

RESOLVED STELLAR POPULATIONS:  
WATCHING GALAXY EVOLUTION IN REAL TIME

Jessica Reis Kitamura

A thesis submitted in partial fulfilment of the requirements of  
Liverpool John Moores University  
for the degree of  
Doctor of Philosophy.  
February 2020

# Declaration

The work presented in this thesis was carried out at the Astrophysics Research Institute, Liverpool John Moores University. Unless otherwise stated, it is the original work of the author.

While registered as a candidate for the degree of Doctor of Philosophy, for which submission is now made, the author has not been registered as a candidate for any other award. This thesis has not been submitted in whole, or in part, for any other degree.

Jessica Reis Kitamura  
Astrophysics Research Institute  
Liverpool John Moores University  
IC2, Liverpool Science Park  
146 Brownlow Hill  
Liverpool  
L3 5RF  
UK

MAY 2, 2020

# Abstract

One of the main issues in astrophysics is to understand how galaxies form and evolve. Deep photometric studies help the investigation of the evolution of resolved stellar contents of nearby systems. Hence the properties of these regions represent an archaeological record of the processes that shape a galaxy over cosmic time. So one can interpret from the star formation history the evolution of the star formation rate throughout the galaxy and the evolution of the mass and metallicity distributions. The system that has been studied in this project is the nearby galaxy M33, located in the Local Group. The photometric data was taken in the Canada-France-Hawaii Telescope with the MegaPrime/MegaCam wide-field mosaic imager and it is available for the filters  $g'$ ,  $r'$  and  $i'$ . The data analysis is presented in this work with the purpose of recovering its star formation history. Over one million point sources were identified in each filter. The program chosen for this process is DAOPHOT (Stetson, 1987). PSF-fitting photometry was performed using a few hundreds of point sources, selected from non-crowded areas, to fit the point-spread functions. This process, however, was repeated a couple of times in order to get a well adjusted point-spread function with the least residuals possible. The instrumental magnitude was then determined. A selection cut enabled spurious sources to be discarded based on the photometric errors ( $\sigma$ ), residuals scatter ( $\chi^2$ ) and image quality (sharpness). Aperture and offset corrections were applied in the magnitudes before the transformation to the standard photometric system. A completeness test to examine the effects of crowding in the images was conducted in each photometric filter. The bias in the observed magnitudes and in the stellar counts due to high stellar density affects the final star formation history, resulting in the miss-assumption of the stellar age, metallicity and initial mass function. The

artificial stars test (Williams et al., 2009) is a standard technique used to that end and consists of inserting synthetic stars in the images, with the routine ADDSTAR (Stetson, 1987), and performing again the photometric reductions in those synthetic images to compare the known inserted brightness with the recovered ones. The completeness is given by the ratio of the number of retrieved artificial stars over the number of added ones.

Stars of all evolutionary stages lose mass and the mass recycled in the interstellar medium will be part of the next generation of stars and planets. The study of mass loss is quite well understood for metal-rich stars populating the asymptotic giant branch, though there is still a lot to be understood about the metal-poor stars losing mass during the red giant phase. The understanding of the mass loss process that happens in red giant stars of globular clusters might help us to better estimate the post-main sequence stellar evolutionary stages and the intra-cluster gas enrichment. Since the 70's it has been known that the Galactic globular cluster  $\omega$  Centauri shows an extremely complex stellar chemistry, with a wide variation in metallicity,  $[\text{Fe}/\text{H}] \approx -2$  to  $[\text{Fe}/\text{H}] \approx -0.6$ , and light elements (like He, C, N...). Indeed, the properties of  $\omega$  Cen favours the hypothesis that this is a remnant of a dwarf galaxy orbiting the Milky Way and tidal interactions partially disrupted it. With observations from the Infra-Red Array Camera aboard of the *Spitzer* telescope, investigations on red giant stars in  $\omega$  Centauri are carried out to identify infrared colour excess originating from the emission of a circumstellar envelope surrounding the stars (e.g. Frogel & Elias, 1988; Origlia et al., 1996). This study is based on a proper combination of ground-based and original Spitzer photometric data as well as results from previous spectroscopic surveys. Prior to the selection of the dust excess stars, the magnitudes from the SDSS photometric system are converted to the TCS system based on the colour relations of Carpenter (2001) and Alonso et al. (1998) as the colour-temperature equations used to calculate the effective temperature are in different photometric filter systems. Bolometric corrections and the effective temperature are needed for comparisons between observations and theory and both parameters were derived according to Alonso et al. (1999). After selection, 34 giant stars presented colour excess in  $(K - 8)$  with metallicities ranging from  $-1.9 < [\text{Fe}/\text{H}] < -0.7$ ;

metallicities that were interpolated from PARSEC isochrones (Bressan et al., 2012). Field stars were rejected based on the proper motions from GAIA, which reduced to 18 the number of mass-losing candidates. The large amount of field stars excluded from the sample is due to the difference in spatial coverage from GAIA and Spitzer. The stellar synthetic spectral distribution of those stars is modelled and used to calculate its mass loss rate, using a modified version (Origlia et al., 2007) of the radiative transfer code DUSTY (Ivezic et al., 1999; Elitzur & Ivezić, 2001). The mass loss rates derived from our sample are in the range of  $10^{-8}$  to  $10^{-7} M_{\odot} yr^{-1}$ , which is slightly off the values proposed by Origlia et al. (2002) and Boyer et al. (2008). The mass loss rates seem to increase with increasing luminosities and its dependency with metallicity is minimal. Only a fraction of red giant stars are losing mass indicating an episodic mass loss.

# Acknowledgements

This work would not have been finished without the help of others. I would like to take this opportunity to recognise their precious participation.

Firstly, I would like to thank Dr. Maurizio Salaris and Dr. David Bersier for accepting me as their pupil and for sharing all their knowledge and experience in the past four years.

I would like to express my sincere appreciation to the examiners Dr. Nate Bastian and Dr. Livia Origlia for their valuable suggestions and corrections, which greatly improved the presentation of this manuscript.

I have been honoured to collaborate with the University of Bologna team: Dr. Emanuele Dalessandro and many others upon whose work this thesis is partially based. Thanks for giving me this pleasure and privilege.

I am grateful to all staff members and to all my colleagues at ARI for reminding me why I am here, for supporting me throughout these years, especially when I was feeling tired and overwhelmed. Thanks for the caring, all the smiles, for understanding, taking my hand, drying my tears, not letting me to give up. Thank you all for being present, positive, supportive. Thanks for Harriet Brown and Tricia Sullivan for the constructive criticism of the manuscript.

I cannot forget to thank my family members and friends that were in a 'galaxy' far, far away but always in my heart. Ciria Lima, Alexandre Araujo and Denise Castro, you were always there for me. Allyson Kitamura, without your help it would have been harder for me to accomplish this. It all started when you boarded on this adventure

with me, then you taught me programming, then you heard my troubles. Now we are here, together, ready (or not!) for the next stage. Stella and Levi, both of you arrived in the middle of this all and made it a bit more complicated, but a lot more satisfying. Thanks for transforming this opportunity in the best experience of my life.

Dr. Lucimara Pires Martins, you triggered this moment, you were the first one to believe and encourage me, even more than that. I cannot be thankful enough for all you did. I will always remember the kind person you are, the exceptional professional you are. Among other brilliant women that inspired me, you are the greatest. Thank you so much! All my gratitude for you.

I appreciate the financial support that CNPq (Conselho Nacional de Desenvolvimento Científico e Tecnológico - Brasil) granted me under the fellowship number 234457/2014-7.

Finally, thanks to everyone that directly or indirectly were involved on this journey with me.

# Contents

<b>Declaration</b>	<b>ii</b>
<b>Abstract</b>	<b>iii</b>
<b>Acknowledgements</b>	<b>vi</b>
<b>Contents</b>	<b>viii</b>
List of Tables . . . . .	xii
List of Figures . . . . .	xiii
<b>1 Introduction</b>	<b>1</b>
1.1 Star formation history of galaxies . . . . .	1
1.1.1 Characteristics of the galaxy M33 . . . . .	4
1.1.2 Methods to derive the SFH . . . . .	7
1.2 Mass Loss . . . . .	8
1.2.1 Observational evidence of mass loss in globular clusters . . .	10
1.2.2 Characteristics of the Galactic globular cluster $\omega$ Centauri . .	11
1.3 Goals . . . . .	12

1.3.1	M33 . . . . .	12
1.3.2	$\omega$ Centauri . . . . .	13
<b>2</b>	<b>Structures and evolution of galaxies and stars</b>	<b>14</b>
2.1	Galaxies . . . . .	15
2.1.1	Galaxy formation . . . . .	16
2.2	Stellar Populations . . . . .	19
2.3	Globular clusters . . . . .	20
2.4	Stellar evolution . . . . .	23
2.4.1	Main Sequence . . . . .	23
2.4.2	Sub-giant branch . . . . .	24
2.4.3	Red giant branch . . . . .	27
2.4.4	Horizontal branch . . . . .	28
2.4.5	Asymptotic giant branch . . . . .	29
2.5	Mass loss mechanisms . . . . .	30
2.5.1	Dust driven winds . . . . .	30
2.5.2	Line-driven winds . . . . .	31
2.5.3	Alfvén wave driven winds . . . . .	32
2.6	Photometry . . . . .	32
2.6.1	Photometric filter systems . . . . .	33
2.6.2	Interstellar extinction . . . . .	36
<b>3</b>	<b>Photometric observations</b>	<b>38</b>

3.1	Data reduction and analysis . . . . .	38
3.1.1	M33 . . . . .	41
3.1.2	$\omega$ Cen . . . . .	55
<b>4</b>	<b>M33 - Artificial stars test</b>	<b>61</b>
4.1	Monte Carlo test . . . . .	62
4.2	AST results . . . . .	63
<b>5</b>	<b>Mass-loss in <math>\omega</math> Cen</b>	<b>76</b>
5.1	Physical parameters . . . . .	76
5.2	Colour excess selection . . . . .	79
5.3	Dust excess sample . . . . .	81
5.4	Mass-loss rate derivation . . . . .	86
5.4.1	DUSTY . . . . .	86
5.4.2	Results . . . . .	88
<b>6</b>	<b>Summary and Future work</b>	<b>91</b>
6.1	Summary . . . . .	91
6.2	Future work . . . . .	93
6.2.1	M33 . . . . .	93
6.2.2	$\omega$ Cen . . . . .	94
<b>A</b>	<b>Complementary tables</b>	<b>96</b>
<b>B</b>	<b>List of Abbreviations</b>	<b>128</b>





# List of Figures

1.1	Image of the Triangulum galaxy in the g' filter, with north up and east to the left. . . . .	5
2.1	Hubble Sequence. Images credit: NED - NASA/IPAC Extragalactic Database. . . . .	17
2.2	Small magellanic cloud. Image credit: APOD/NASA Stephane Guisard.	18
2.3	Fornax dwarf galaxy. Image credit: ESO/Digitized Sky Survey 2. . . .	18
2.4	HRD of four isochrones (Pietrinferni et al., 2004), colours red and blue have same metallicity, $Z = 0.0001$ , but different ages, 5 and 10 Gyr respectively; while green and black have metallicity $Z = 0.01$ , but ages 5 and 10 Gyr. . . . .	21
2.5	HRD of a $1 M_{\odot}$ star's evolutionary track, considering metallicity $Z = 0.02$ . . . . .	25
2.6	HRD of a $5 M_{\odot}$ star's evolutionary track, considering metallicity $Z = 0.02$ . . . . .	26
2.7	Passband comparison of optical broadband systems by Bessell (2005).	34
2.8	Passband comparison of infrared broadband systems by Bessell (2005).	35
2.9	Normalized interstellar extinction curves from the far-IR through the UV. Solid curve is derived by Fitzpatrick (1999) based on $R \equiv A_V/E(B-V) = 3.1$ , further curves were plotted for comparison by the author. . .	37

3.1	Sub-image vs chip positions. The black lines are the boundaries between each sub-image and the blue rectangles are the position of the chips used for the magnitude calibration. . . . .	43
3.2	Illustration of the PSF subtraction. First column corresponds to the original images while the second column corresponds to the residual images after PSF subtraction. First row corresponds to a single star of a non-crowded field and second row corresponds to a crowded field. Each image is shown with the same grey-scale intensity and same pixel size, with north up and east to the left. . . . .	44
3.3	Top panel is $\sigma$ , increasing as the magnitudes get fainter expectedly due to a higher uncertainty in the photometric magnitude determination of faint sources. Middle panel is $\chi^2$ and bottom panel is <i>sharpness</i> . . . .	45
3.4	Comparison between the output magnitudes taken from an overlap region of sub-images 52 and 53. The black dots represent differences with dispersion below $3\sigma$ while red dots represent differences with dispersion above $3\sigma$ . To quantify how many stars are scattered by more than $3\sigma$ , the magnitudes were averaged in five magnitude bins. . . . .	46
3.5	Same as 3.4 but the photometry performed for this set considered a higher sky background, eliminating the slope affecting the faint magnitudes seen in 3.4. . . . .	47
3.6	Plot of the flux versus the radius (in units of pixels) for the PSF stars of a given sub-image. The solid red line is the average flux. . . . .	49
3.7	Colour-Magnitude Diagram, $g'-r'$ versus $r'$ . . . . .	51
3.8	Colour-Magnitude Diagram, $g'-i'$ versus $i'$ . . . . .	51
3.9	Comparison between the calibrated magnitudes from this current work (CW) dataset and KT's dataset for $g'$ filter. . . . .	54

3.10	Comparison between the calibrated magnitudes from this current work (CW) dataset and KT's dataset for r' filter. . . . .	54
3.11	Comparison between the calibrated magnitudes from this current work (CW) dataset and KT's dataset for i' filter. . . . .	55
3.12	Three colour image of $\omega$ Cen. Red is $8 \mu m$ , green is $5.8 \mu m$ and blue is $3.6 \mu m$ . . . . .	56
3.13	(K - 3.6) (top-left) vs. K, (K - 4.5) (top-right), (K - 5.8) (bottom-left), (K - 8) (bottom-right) CMDs for $\omega$ Cen. . . . .	60
4.1	Top-left: plot of the ratio between the recovered and the injected artificial stars; Middle-left: comparison of the observed, injected and recovered stars; Bottom-left: blue dots are the magnitude difference; Top-right: the dispersion in position (x and y); Middle- and Bottom-right: histograms of the dispersion in x and y respectively. . . . .	64
4.2	Completeness (the ratio of the number of recovered stars over the number of inserted artificial stars) by instrumental magnitude. Red dot is the magnitude where 50% of stars were recovered and the total length of the error bar is 0.5 dex (equivalent to the bin-width at which the ratio was calculated). Multiple columns are located in the outskirts of the galaxy and opposite to each other whilst the middle column is in the centre of the galaxy. Top row is g' filter, middle row is r' filter and bottom is i' filter. . . . .	65
4.3	The distribution of the difference of magnitude $\Delta mag$ with the exponential (magenta) and polynomial (yellow) functions fitted on it for g' filter. Red lines are the average and $\pm 1\sigma$ . Left and right plots are located in the outskirts of the galaxy and opposite to each other whilst the middle plot is in the centre of the galaxy. . . . .	67
4.4	Same as figure 4.3, but for r' filter. . . . .	68

4.5	Same as figure 4.3, but for i' filter. . . . .	69
4.6	Parameter b, from the exponential function $f(x) = ae^{(x/b)} + c$ , versus stellar density. Top plot is result for g' filter, middle plot refers to r' filter and bottom plot is i' filter. . . . .	71
4.7	Magnitude at 50% recovery rate versus stellar density. Top plot is result for g' filter, middle plot is referent to r' filter and bottom plot is i' filter. . . . .	72
4.8	Stellar density $\left(\frac{N_* \times PSF^2 \pi}{N_x \times N_y}\right)$ for the sub-images of the g' filter. The axes are the spatial position xy in pixels and the number written inside each square is the instrumental magnitude at which 50% of the stars were recovered. . . . .	73
4.9	Same as figure 4.8, but for the r' filter. . . . .	74
4.10	Same as figure 4.8, but for the i' filter. . . . .	75
5.1	Hertzsprung-Russel Diagram for $\omega$ Cen. . . . .	79
5.2	$(K - 8)$ colour vs. $M_{bol}$ CMD for $\omega$ Cen. Stars with IR colour excess are marked with red circles, green squares are ML candidate stars from Boyer et al. (2008). 44262 (V42), 52030 and 43105 (V29) are stars identified also by Woolley (1966); Clement (1997); van Leeuwen et al. (2000); Kaluzny et al. (2004); McDonald et al. (2011). . . . .	80
5.3	$(K - 5.8)$ vs. $(K - 8)$ colour-colour diagram for $\omega$ Cen. Stars with IR colour excess are marked with red circles. . . . .	81
5.4	$(B - I)$ colour vs. B for stars in $\omega$ Cen. Optical CMD used to select AGB stars (red circles). Blue circles are LPV stars from van Leeuwen et al. (2000); Lebzelter & Wood (2016); Mowlavi et al. (2018). . . . .	82
5.5	PARSEC (Bressan et al., 2012) theoretical isochrones, assuming $[Fe/H] = -0.7, -1.0, -1.3, -1.6$ and $-1.9$ and age 10 Gyr. . . . .	83

5.6	( $K - 8$ ) colour vs. $[Fe/H]$ for the dusty stars in $\omega$ Cen. The colour is an average of all stars with that particular metallicity. Metallicities were interpolated from theoretical isochrones. Stars with low metallicity does not seem to restrict dust production. . . . .	84
5.7	Top panel: ML rate as a function of the bolometric magnitude for the metal-poor (green) and metal-rich (red) RGB stars of $\omega$ Cen with dust excess. Bottom panel: Average total mass lost by the metal-poor (green) and metal-rich (red) RGB sub-populations of $\omega$ Cen. The error bars are the $1\sigma$ uncertainty in the average total ML. The solid line is the fitting relation $\pm 0.03$ rms (dotted lines) for the GGCs studied by Origlia et al. (2014), which is only shown for reference. . . . .	89

# Chapter 1

## Introduction

### 1.1 Star formation history of galaxies

The formation and evolution of galaxies is still one of the most challenging cosmological problems to be solved. The processes involving the baryonic matter assembly, *i.e.* gas shocking and cooling in dark matter haloes, star formation, supernovae and active galactic nuclei feedback, chemical enrichment, and stellar evolution, are lacking a full comprehension and are still in need to be investigated (Baugh, 2006). Basically, there are two main approaches to explore galaxies, observing galaxies over a range of redshifts (cosmic time) or analysing the past history of star formation of local galaxies with their current stellar population. For the former though, there are certain limitations, like only being able to observe the galaxies with higher surface brightness at large distances and to have access only to an integrated spectral energy distribution of all stellar constituents. The latter, on the other hand, benefits from the possibility to resolve the stellar content and the results could be used to compare with galaxies at high redshift.

The star formation history (SFH) of a system denotes the evolution with time of the star formation rate (SFR; which is the total mass of stars formed in a given period of time) and the metallicity. The formation of stars can happen by the accretion of

the gas from other objects or intergalactic medium, onto discs, then this gas is cooled and form molecular clouds and the cloud fragments are accreted into denser cores, the contraction of the cores subsequently form stars and planets (Kennicutt & Evans, 2012).

The formation of stars in galaxies could be described in three distinct evolutionary scenarios (Martín-Manjón et al., 2011). In the first scenario, stellar formation happens as an initial burst at the moment the galaxy was formed. In another scenario, a galaxy could continuously form stars, but slowly decrease the formation rate since the time of the galaxy formation. Lastly, an episode of intense star formation could occur sometime after the galaxy formation epoch and lasts for a short period, when compared to the galaxy lifetime.

Besides, the star formation occurs differently according to the different morphological types of galaxies. For instance, luminosity evolution models commonly assume that most of the elliptical galaxies have undergone starbursts (intense rate of star formation) at an early epoch and now is quenched (Kitzbichler & White, 2006), conversely spirals are still forming stars to the present day (Brinchmann et al., 2004).

The SFR is usually related to the surface density of gas, commonly known as Schmidt Law of star formation (Schmidt, 1959), mathematically presented as a power law relation of the form  $\dot{\Sigma}_{\star} \propto \Sigma_{gas}^N$ , where  $\dot{\Sigma}_{\star}$  is the star formation rate summed along a line-of-sight through the galaxy disc, in units of  $M_{\odot} pc^{-2} yr^{-1}$ , and  $\Sigma_{gas}^N$  is the sum of the surface densities of atomic and molecular gas, in units of  $M_{\odot} pc^{-2}$ . Kennicutt (1998) found the best fit of  $N = 1.4$  from a sample of 97 nearby star-forming galaxies.

Chemical evolution is another important ingredient to trace the SFH. There are three main processes responsible for the formation of chemical elements in the Universe. The primordial nucleosynthesis that occurred in the first minutes of the formation of the Universe, when matter was very hot and dense, and formed elements like hydrogen, helium, their isotopes and lithium. Stellar nucleosynthesis forms elements in the core of the stars (mainly helium, carbon, nitrogen, oxygen and s-process elements) and in supernovae explosions (in Type II supernovae is formed mainly  $\alpha$ -elements, iron and

iron-peak elements and in Type Ia supernovae mainly iron-peak elements are formed). Interstellar nucleosynthesis, that is the interaction between cosmic rays and the interstellar medium (ISM) gas, which produces light elements like lithium and berillium (Audoze & Mathieu, 1986).

Besides the production site of the chemical elements, one can interpret from the chemical enrichment history the enrichment timescales. For instance, elements originated from Type II supernovae generally take about  $\sim 10^7 yr$  to pollute the ISM (which is the time massive stars take to reach their final evolutionary stage and explode as Type II supernovae); on the other hand, the majority of iron produced by Type Ia supernovae takes longer to pollute the ISM,  $\sim 1 Gyr$  (Greggio, 2005). There are some conditions to consider during the analysis of the chemical evolution of galaxies: if the first stars were formed from a primordial gas or from a pre enriched gas, the rate at which stars were formed and its distribution, the amount of enriched gas ejected by stars, gas inflows and outflows, radial flows of gas and stars and accretion of material from other systems. Therefore, studying the SFH of galaxies is essential to reveal such differences in the mechanisms and processes that drive the star formation and the chemical evolution.

To help us unveil the formation and evolution of the Universe, it is important also to understand the formation and evolution of individual galaxies. Although disc galaxies are interesting objects for offering a complex varied range of stellar populations distributed along each of its components (bulge, halo and discs), there exist some uncertainties related to the bulge (e.g. structure, formation, chemical enrichment; Graham, 2001; Robin et al., 2012; Nataf, 2016), and tidal interactions and mergers (Barnes & Hernquist, 1992).

Interestingly, galaxies like M33 largely overcome these disadvantages; given that, in the specific case of M33, it apparently had only a few interactions with M31 (Bekki, 2008; McConnachie et al., 2010; Davidge & Puzia, 2011; Wolfe et al., 2013), is bulge- and barless (Bothun, 1992; Regan & Vogel, 1994), and has weak spiral arms (Dobbs et al., 2018) that interferes with stellar formation (Seigar & James, 2002; Dobbs, 2011). Furthermore, the galaxy M33 is also a dwarf spiral which, conveniently, is the ideal

representative target of the most common type of galaxy in the local universe (Marinoni et al., 1999; Brown, 2009), as well as low-mass galaxies are well distributed at all redshifts (Bauer et al., 2013). Its relatively face-on inclination is advantageous to determine its metallicity and SFR and to resolve its stellar populations in the disc and halo on its entirety. Consequently, studying the stars of stellar populations in the spiral galaxy M33 makes it possible to address some key aspects of galaxy formation, such as the SFR as a function of metallicity.

### 1.1.1 Characteristics of the galaxy M33

The nearby galaxy Messier 33 (also known as Triangulum Galaxy or NGC 598) is a relatively metal-poor, late-type spiral galaxy, located in the Local Group at a distance of about 850 kpc (Freedman et al., 1991) and its total mass is about  $10^9 M_{\odot}$  (Corbelli, 2003). The Local Group, which is a non-compact galaxy cluster where our galaxy is settled in, contains roughly about 50 galaxies where the three most dominant are M31, the Milky Way and M33 (emitting 90% of the visible light, all together) and the rest of them are dwarf galaxies (no high masses, no high luminosities).

M33 is an interesting laboratory, since its proximity allows us to resolve the individual stars and its nearly face-on inclination, projected over a large area on the sky, makes it an ideal candidate for wide-field CCD mosaic imaging. M33 is one of the very few galaxies luminous and close enough where this type of study can be done in such detail, and the result could be used as complementary to the ones obtained from galaxies at high redshift. The fact that M33 has no bulge component may facilitate the understanding of disc evolution as thin discs are the product of gas accretion, while thick discs tend to be built up through merging (Barker et al., 2011). While other studies have examined the SFH in M33 using resolved stars, none have been as finely resolved in deep fields as the work proposed here, and most of them have been dedicated to its outer regions of the disc, as its centre is challengingly presented due to a crowded stellar core.

Williams et al. (2009) have determined the SFH in the inner and outer disc of M33

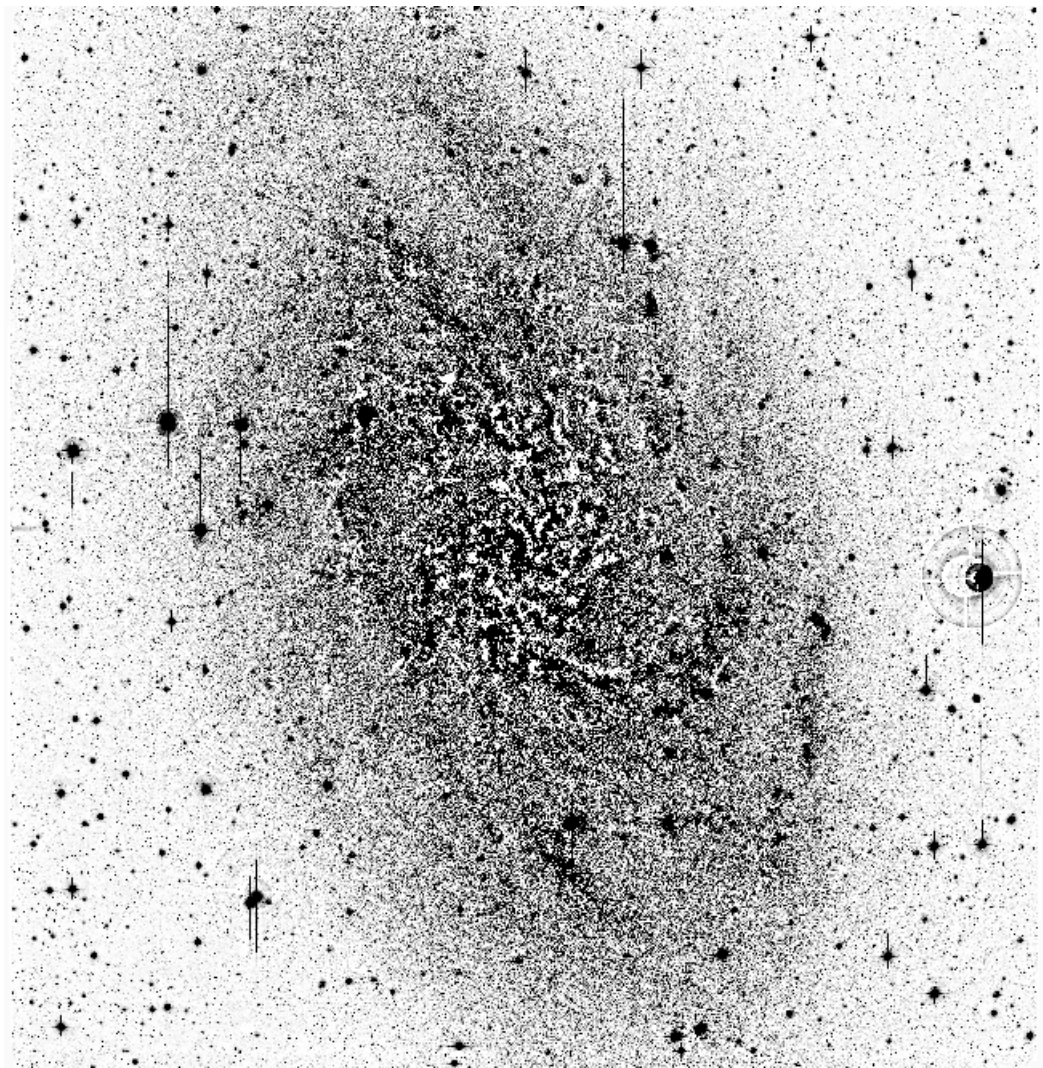


Figure 1.1: Image of the Triangulum galaxy in the  $g'$  filter, with north up and east to the left.

using deep images from HST/ACS. They found that most of the disc stars outside of 3 kpc were formed in the last 8 Gyr, which differs from what is observed in massive spiral galaxies that usually had stars formed before that. The authors have analysed four fields at different radii. Comparing the Colour-Magnitude Diagram (CMD) of each field, they have noticed that the number of main sequence (MS) to giant stars increases with radius, and this suggests a decrease of stellar ages with increasing radius within 8 kpc, but at larger radii the average age increases with radius. The authors state that this radial age inversion is in agreement with simulations of disc evolution and is related to the inside-out disc formation theory.

Barker et al. (2011) have studied two fields in the outer disc at 9.1 and 11.6 kpc using images from HST/ACS and have determined the SFH. In agreement with Williams et al. (2009), Barker et al. (2011) found that most of the disc stars were formed by 8 Gyr ago. They analysed the colour function of each field, finding that the first field is mostly populated by 2 to 4 Gyr age range and metallicity range from  $-0.8$  and  $-0.2$  dex, while the second field is older, age range from 4 to 9 Gyr, and more metal-poor, metallicity range from  $-1.0$  to  $-0.5$  dex. The age gradient could be explained as a result of radial migration, however they believe this is not likely to be true for M33 for those two particular fields because of the small percentage of stars ( $\sim 14\%$ ) older than 4.5 Gyr in the first field compared to the inner disc where stars of that age are more common ( $> 50\%$ ).

Davidge & Puzia (2011) have analysed young stars in the stellar disc of M33 using five deep wide-field observations from MegaCam on the CFHT. The authors suggest that star formation has been constant in the inner disc, within the 8 kpc radius, for the past 250 Myr and SFR decreases with increasing radius. However, their data shows evidence of young stars in the outskirts of the disc, with similar properties of those with ages  $\sim 100$  Myr, suggesting radial migration or star formation that happened in intermediate epochs in an extended disc.

Beasley et al. (2015) have characterized 77 star clusters using spectroscopic observations from Gran Telescopio de Canarias and William Herschel Telescope. The star clusters sample an age distribution from a few  $\sim 10$  Myr to 13 Gyr and metallicity

range from  $-1.74$  to  $0.18$  dex; more than half of this sample is younger than 1 Gyr and more metal rich than  $[M/H] = -1$ . They found an age-metallicity relation for the clusters and evolution of the metallicity gradient was found in the disc, but no evidence was found for a radial age gradient in the disc clusters. In comparison with the Milky Way, globular clusters (GC) in M33 are more metal rich and the age-velocity dispersion relation is similar to the clusters in the Milky Way.

McMonigal et al. (2016) have used data from the Pan-Andromeda Archaeological Survey on the CFHT MegaPrime to detect a halo on M33. Despite the robust statistical analyses, they were not able to detect a halo component neither in the observations nor in a synthetic dataset. The authors explain that if there were a halo component it was completely dominated by every other component in the galaxy.

### 1.1.2 Methods to derive the SFH

The most common methods developed to determine the SFH of nearby galaxies are based on matching the density of stars with stellar evolution models. Usually, one creates synthetic CMDs, that is a theoretical simulation of the observed CMD of a stellar population, to compare with the observational ones using a merit function or maximum likelihood technique. Then, the stars are binned in both observed and synthetic CMDs and the number of stars in each bin is compared. However, this binning scheme limits the resolution of the solution and inserts a subjective element into the method (Aparicio & Hidalgo, 2009). A synthetic CMD must also include effects of photometric errors, blending and incompleteness that may affect the observed CMD of the stellar population in analysis. Generally, this is accomplished accounting for the results achieved in the artificial star tests in the observational data.

Some widely used synthetic CMD computational codes are *starFISH* (Harris & Zaritsky, 2001), *MATCH* (Dolphin, 2002), *IAC-star* (Aparicio & Gallart, 2004) complementary to the *IAC-pop* (Aparicio & Hidalgo, 2009), which is a method to solve the SFH, and *Talos* (de Boer et al., 2012). These methods have been used in several applications (i.e. Harris & Zaritsky, 2004; Brown et al., 2006; Barker et al., 2007; Williams et al.,

2009). Some variants of the method above have been presented by Tolstoy & Saha (1996), applying a Bayesian probability approach, and Vergely et al. (2002), using an inverse method to recover the SFR. *FIREs* (Small et al., 2013) represents a composite stellar population by a linear combination of isochrones (multiple isochrones, each one with its own amplitude or weight) instead of binning the CMD. This means that, with this method, each star is fit to an isochrone.

Synthetic CMDs have been used to examine some massive galaxies (e.g. Hernandez et al., 2000; Brown et al., 2006; Williams et al., 2009; Bernard et al., 2012, 2015) and to probe low mass galaxies (e.g. Harris & Zaritsky, 2001, 2004; Cole et al., 2007; Weisz et al., 2014) since these are the most numerous type of galaxies in the Local Group, which is one of the few places where low mass galaxies can be well resolved with the current telescopes. However, they have been limited to small fields or low spatial resolution. The observations used on this project are from the wide-field camera in the Canada-France-Hawaii Telescope (CFHT) with high resolution photometry, fully covering the local galaxy M33.

## 1.2 Mass Loss

Almost all stars experience mass loss (ML) by stellar winds of various type (e.g. pressure-, radiation- or wave-driven wind), with the ML increasing drastically during stellar evolution<sup>1</sup>. For instance,  $1M_{\odot}$  stars lose about  $10^{-14}M_{\odot}yr^{-1}$  (Willson et al., 1987; Lim & White, 1996) during the MS phase; red giant branch (RGB) stars, with initial masses of about  $0.8 - 0.9M_{\odot}$ , are expected to lose about  $10^{-8} - 10^{-6}M_{\odot}yr^{-1}$  (Origlia et al., 2002, 2007; Boyer et al., 2010) and asymptotic giant branch (AGB) stars, with initial masses of about  $0.5 - 8M_{\odot}$ , lose about  $10^{-8} - 10^{-5}M_{\odot}yr^{-1}$  (Höfner & Olofsson, 2018); however, the exact amount of mass lost depends essentially on the stellar initial mass and metallicity. Stellar winds enrich the ISM with metals, possibly triggering new populations of stars (Tenorio-Tagle et al., 1987; Oey & Massey, 1995). The pollution of the ISM is either by the material produced through nuclear processes

<sup>1</sup>A brief explanation of each phase can be found on section 2.4

in the centre of the former star, which is injected in the ISM through ML mechanisms in the whole lifetime of the star, or also with heavy elements produced by neutron captures during the explosion of massive stars.

Mass loss can be traced from the primordial eras of the Universe with the first stars. The first stars were a population of very massive stars to first form in the early Universe; they are believed to play a role in the evolution of their environment, enriching their local surroundings with metals formed during their short life and ejected in episodes of ML with heavy elements formed during their explosion as supernovae (Johnson et al., 2008b). The feedback effects of the first stars were paramount for the formation of next generation of stars and in the formation of the first galaxies (Johnson et al., 2008a). With regard to the mass lost in the explosive event of a supernova, gamma-ray bursts are produced and they are important tracers of the SFH at high redshift (Dado & Dar, 2014; Wang & Dai, 2014; Tan et al., 2015; Savaglio, 2015; Greiner et al., 2016; Wei & Wu, 2017). The ML influences the angular momentum loss, thus may dictate whether or not the star become such a burster (Petrovic et al., 2005; Woosley & Heger, 2006). Besides impacting the SFH determination at high redshift, the modelling of ML for low-mass red giants affects the stellar distributions used in SFH modelling that incorporates the horizontal branch (HB) morphology into synthetic CMDs of resolved galaxies in the local Universe (Aparicio & Gallart, 2004; Savino et al., 2018).

Undoubtedly, mass loss is an important process to the understanding of many subjects, from stellar to extragalactic astrophysics. Still, some aspects of the ML mechanisms need more studying (Goldberg, 1979), such as the stellar angular momentum transferred to the stellar wind (Lamers & Leitherer, 1993; Allain, 1998), stellar wind theories (Lucy & Solomon, 1970; Abbott, 1982; Pauldrach et al., 1993; Falceta-Gonçalves & Jatenco-Pereira, 2002) as well as the impact of the ML on the evolution of stars (e.g. Chiosi & Maeder, 1986; Jimenez & MacDonald, 1996; Fusi Pecci & Bellazzini, 1997; Origlia et al., 2007; Salaris et al., 2009; Percival & Salaris, 2011; Salaris et al., 2016), such as the reduction of the total stellar mass with evolution in the Hertzsprung-Russel Diagram (HRD), the chemical composition in the stellar surface, the susceptibility to

undergo physical instabilities, and the final stellar evolutionary stage (Goldberg, 1979). Although the ML rates on the MS are negligible (in the order of  $10^{-14} M_{\odot}yr^{-1}$  (Willson et al., 1987)), it is extremely significant on the RGB, because the total mass with which a star leaves the RGB reflects directly in the HB morphology and in the AGB timescale (Salaris et al., 2016). Also, the period-luminosity relation for RR Lyrae stars can be explained theoretically if stars lose a considerable amount of mass, not only in the RR Lyrae pulsation phase itself but also during the giant phase (Christy, 1966; D’Cruz et al., 1996) and if a RGB star loses its whole envelope rapidly it turns into a helium white dwarf star (Rood, 1973; D’Cruz et al., 1996). Some studies explain the temperature and colour distribution of the HB stars (also known as “The second parameter effect”; D’Cruz et al., 1996; Fusi Pecci & Bellazzini, 1997; Ferraro et al., 1998; Whitney et al., 1998; Catelan, 2000; Catelan et al., 2001) and the match between observed and synthetic HB models (Iben & Rood, 1970; Catelan, 1993; di Criscienzo et al., 2010; Dalessandro et al., 2013; McDonald & Zijlstra, 2015; Salaris et al., 2016) as a probe of the red giant ML.

### 1.2.1 Observational evidence of mass loss in globular clusters

Observationally, the evidence that red giant stars lose mass can be obtained by P Cygni profiles, where emission and absorption lines are both observed in the same spectral line profile, and molecular lines are redshifted due to the velocity of the outflowing gas in the stellar envelope; and by circumstellar envelopes, which is the stellar radiation reemitted by dust grains in cool clouds surrounding the star, at larger distances, causing an excess emission relative to the stellar flux in the infrared.

A significant ML rate of about  $10^{-8} M_{\odot}yr^{-1}$  has been calculated based on ultraviolet absorption lines in spectroscopic observations of a M-type supergiant star, whose circumstellar envelope has an expansion velocity of  $10 \text{ km s}^{-1}$  (Deutsch, 1956). Elitzur et al. (1976) identified OH maser emission lines from circumstellar envelopes of M-type stars and from that derived a ML rate of  $10^{-5} M_{\odot}yr^{-1}$ . A ML rate for AGB stars of about  $10^{-7} - 10^{-8} M_{\odot}yr^{-1}$  was calculated based on circumstellar CO emission in

M-type irregular and semi-regular AGB-variables (Olofsson et al., 2002). There was no correlation between the ML and stellar temperature, while the correlation between the ML and the gas expansion velocity would indicate a dust-driven wind mechanism.

Origlia et al. (2002) using ISOCAM observations found a mid-IR excess associated with giants in several GC and attributed it to dusty circumstellar envelopes. The sample size was for a small region of the core of the clusters, where there are less than 30% of the brightest giants, so they only found the long period variable star 44262 (V42) and could not proceed to the ML rate determination.

Also studying the circumstellar envelope of giants, Boyer et al. (2006) detected a population of dusty red giants near the centre of M15. Boyer et al. (2008) characterized stars observed with *SPITZER* and selected about 75 dust excess candidates in the GC  $\omega$  Centauri. They detected stars with the most significant ML to be near the tip of RGB and estimated that the total ML is about  $2.9\text{-}4.2 \times 10^{-7} M_{\odot} \text{yr}^{-1}$ , with more than 60% of this total regarding the three brightest M-type stars (LEID 33062, 44262 (V42), 35250). The authors also predicted that if the ML has been constant in the cluster, in the last  $3.4 \times 10^6$  years  $\omega$  Cen has lost about 1-2  $M_{\odot}$ .

Origlia et al. (2007) identified dusty RGB stars in 47 Tuc and derived an empirical ML law for Population II stars. Mass loss rates derived from these observations showed that the ML increases with luminosity and possibly it is episodic.

### 1.2.2 Characteristics of the Galactic globular cluster $\omega$ Centauri

The Galactic GC  $\omega$  Centauri (NGC 5139) is the most massive ( $\sim 4.5 \times 10^6 M_{\odot}$  (D'Souza & Rix, 2013)) and luminous GC in the Milky Way, with a complex stellar population sampling probably many different ages, and a large range in iron abundance spanning from  $[\text{Fe}/\text{H}] \sim -2.0$  to  $[\text{Fe}/\text{H}] \sim -0.6$  (e.g. Norris & Da Costa, 1995; Pancino et al., 2002; Origlia et al., 2003), and light elements (like He, C, N...). Due to its properties, it is commonly accepted that this GC is the remnant of a dwarf galaxy orbiting the Milky Way and was partially disrupted because of tidal interactions (e.g.

Bekki & Freeman, 2003).

Stellar dynamical models estimate that 9% of  $\omega$  Cen total mass is attributed to heavy remnants (black holes and neutron star), 40% to white dwarfs, and the remaining 51% to non-remnant stars (giants and MS, Meylan, 1987). Giersz & Heggie (2003), on the other hand, suggest that heavy remnants (in their definition: neutron stars + white dwarfs) mass represents about 55% of a total mass of  $3.6 \times 10^6 M_{\odot}$ . The dynamical models of Noyola et al. (2006, 2008) suggest that the presence of a black hole of mass  $4 - 5 \times 10^4 M_{\odot}$  in the cluster core is necessary to match observations.

Later Hubble Space Telescope (HST) data helped in the identification of the MS segregation into two main chemical groups (Anderson, 2002; Bedin et al., 2004; Milone et al., 2017; Bellini et al., 2018). Pancino et al. (2000) found an extremely metal-rich anomalous RGB (RGB-a). The population of RGB-a stars is parallel to the giant branch at much cooler temperatures and lower optical brightness than that of the main RGB. This anomalous branch has now been traced down to the sub-giant branch, or SGB-a with metallicity of about  $[\text{Fe}/\text{H}] = -1.1$  (Villanova et al., 2007).

## 1.3 Goals

### 1.3.1 M33

We prepare the ground for investigating the SFH of the nearby galaxy M33, with the data obtained by the MegaPrime/MegaCam wide-field mosaic imager observations on the 3.6 m CFHT. To achieve that, firstly the photometry is performed for each filter to obtain the instrumental magnitudes. The program chosen for this process is DAOPHOT (Stetson, 1987). The instrumental magnitudes obtained for the optical data should be calibrated into apparent magnitudes in a standard photometric system, correcting effects of discrepancies between instrumental and standard systems, atmospheric extinction and colour-correction. Secondly, the effects of crowding on the photometry are going to be assessed. It is important to quantify this properly because

the bias in the observed magnitudes and star counts will affect the final SFH. The standard way of measuring this effect is performing the artificial stars test (Williams et al., 2009) in order to characterise photometric completeness and to account for the observational errors that result from crowding.

Chapter 2 presents a literature review that briefly explains two main theories behind galaxy formation and their evolution and an overview of photometry. Chapter 3 presents details of the reduction and analysis of the observational dataset and chapter 4 discusses the method on which the artificial stars were tested and the subsequent results. Chapter 6 refers to a concise description of all work done and to a recommendation for a future research.

### 1.3.2 $\omega$ Centauri

This work aims at identifying red giant stars with ML in the Galactic GC  $\omega$  Centauri. Observations are performed with the Infra-Red Array Camera on board of the space-based telescope *Spitzer*. Mid-infrared photometry with *Spitzer* Infrared Array Camera (IRAC; Fazio et al., 2004) assists the detection of the colour-excess that comes from the emission of a circumstellar envelope around RGB and AGB stars (e.g. Frogel & Elias, 1988; Origlia et al., 1996). The  $8\mu\text{m}$  IRAC band is especially sensitive to the warm dust emission (Origlia et al., 2010). After selection of the dust excess stars, their synthetic spectral distribution will be modelled and used to calculate their ML rate, using a modified version (Origlia et al., 2007) of the radiative transfer code DUSTY (Ivezic et al., 1999; Elitzur & Ivezić, 2001). An analysis of the ML rate dependency to the metallicity is undertaken.

In chapter 2 is presented a literature review that explains the physical processes undergoing in stars and their evolution, the composition of GC and an overview of photometry. Chapter 3 presents details of the observational dataset, its reduction and analysis and chapter 5 discusses the method on which the stars are selected based on the colour (K - 8) excess and the results. Lastly, the work is summarised in chapter 6 and suggestions of potential new investigations are discussed.

## Chapter 2

# Structures and evolution of galaxies and stars

This section approaches the background in order to understand the physical processes that happen in galaxies and stars. The most commonly accepted theory of galaxy formation and evolution is the *hierarchical model*. In this model, galaxies are formed and evolve through successive mergers of smaller structures. In this way, spiral galaxies are thought to be formed after only a few interactions with other structures, while elliptical galaxies would be formed after several mergers. Galaxies hosts several stellar clusters, they could be simple stellar populations when composed of stars formed at the same time and with the same chemical abundance, or they could be composite stellar populations if one of these two ingredients were different. The chapter also discuss the evolution of stars: all stars start their journey and spend most of their lifetimes in the MS where their stellar core burns hydrogen into helium. In all evolutionary stages stars lose a certain amount of mass through stellar winds, how much mass they lose depends on their initial mass; however, this ML can affect the evolutionary paths of the stars. There are several mechanisms that cause stellar ML; and, the three main mechanisms are described in detail: dust-driven winds, line-driven winds and Alfvén wave-driven winds. At last, it is discussed how photometry allows us to study the radiative flux emitted by a celestial body, the different options of photometric filter systems and the

effect of interstellar extinction.

## 2.1 Galaxies

A galaxy is a dynamically-bound system, containing stellar mass from about  $10^5$  (Kirby et al., 2013) to  $10^{11} M_{\odot}$  (Baldry et al., 2012) and varying in size from 1 to 1000 kpc. For instance, a Milky Way-like galaxy contains about  $10^{10}$  stars and has a diameter of about 20kpc. Several parameters characterize a given galaxy: morphology, luminosity and stellar mass, size and surface brightness, gas-mass fraction (the ratio of cold gas that is actually turned into stars), colour, environment, nuclear activity and redshift. There exist two basic types of galaxies, spirals and ellipticals.

Elliptical galaxies, also known as early-type galaxies, have generally redder colours than spirals, due to the presence of old and/or more metal-rich stellar populations, stars are usually low-mass and, these galaxies commonly show minimal star formation activity. Spirals, also known as late-type or disk galaxies, are extremely flattened disks, which are rotation sustained and are characterized by spiral arms structures. They may also present other morphological characteristics such as bar-like structures and a bulge component in their centres. The photometric colours are bluer than an elliptical with the same luminosity, due to its on average younger stellar content.

The properties of a spiral galaxy's stellar population (such as mass, metallicity, age, magnitudes and colours) can provide important hints about the galaxy's formation and evolution. However, the broadband colours have to be correct for extinction effects, as spirals are usually dusty and often inclined with respect to the line-of-sight. It is also important to carefully consider each component of the spiral galaxy; that is because they all have different stellar populations, *i.e.* normally the bulge and halo are populated by old stars whilst the thin and thick disk components are dominated by stars with a broad range of age and metallicity (although stars from the thick disk are older and more metal poor).

The Hubble Sequence (see example in figure 2.1 Hubble, 1926) is a classification sys-

tem still commonly used to identify the different types of galaxies observed in the Universe. Yet, not all galaxies appear in this classification; for instance, the faintest galaxies called dwarf galaxies. Dwarf irregulars present a very irregular structure and contain a large amount of gas and an active stellar formation activity (see an example in figure 2.2). Dwarf spheroidals are galaxies with no gas and with no or few young stars, and typically present a dispersed structure (see example in figure 2.3).

Some galaxies are part of dense clusters, forming a group of several hundreds, while other are grouped in smaller groups, like the Milky Way, of about a few dozens of galaxies. Cluster structures are gravitationally bound and may interfere in the formation and evolution of the galaxies within, especially because elliptical galaxies are mainly found in clusters and spirals are typically isolated, a field galaxy.

### 2.1.1 Galaxy formation

One of the first ideas to understand the formation and evolution of galaxies was based on gravitational instability occurring in a large gas cloud, similar to what happens with stars. A large cloud in rotation collapses, and the gas which is not gravitationally stable breaks into smaller clouds and form stars. This top-down theory is called the *monolithic collapse model*, and it was first proposed by Eggen et al. (1962). Considering this scenario for instance, on the one hand elliptical galaxies would have been formed in a highly dense cloud, with low rotation velocity and high SFR, while on the other hand spiral galaxies would have been formed in a less dense cloud, with higher rotation velocity and a lower SFR.

The steady advance of technology has allowed us to observe galaxies at increasingly larger redshifts, in the earlier stages of evolution of the Universe and to study the local Universe with a better spatial resolution. Searle & Zinn (1978) studied red giants of 19 GC in the Galactic halo and derived a wide range of metallicity and ages for those stars. In a monolithic scenario of formation, however, these GC should have formed from an early collapse of a gas with low metallicity; which is not the case. Hence, they concluded that the halo have probably been accreted over a period of time,

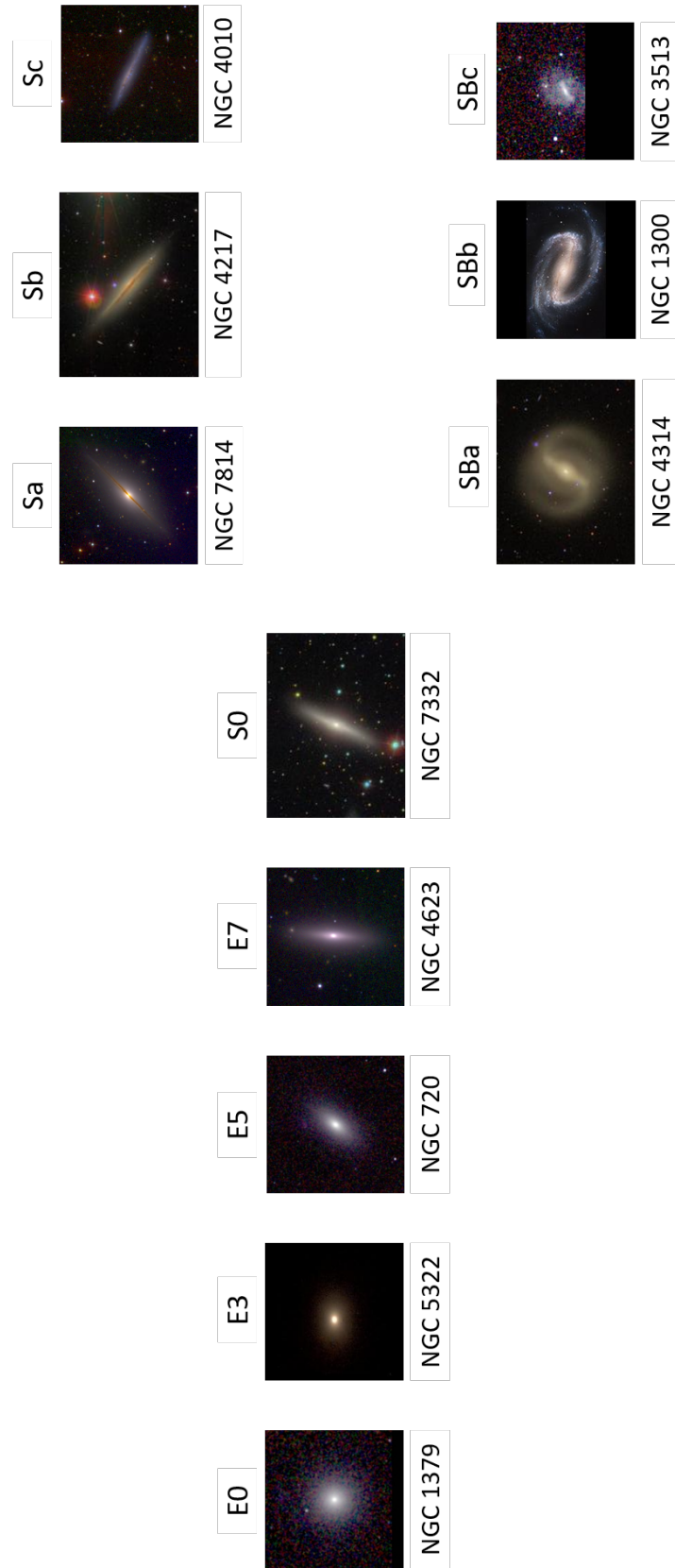


Figure 2.1: Hubble Sequence. Images credit: NED - NASA/IPAC Extragalactic Database.



Figure 2.2: Small magellanic cloud. Image credit: APOD/NASA Stephane Guisard.



Figure 2.3: Fornax dwarf galaxy. Image credit: ESO/Digitized Sky Survey 2.

either by clouds of intergalactic gas or dwarf galaxies that merged with the Milky Way. Furthermore, studies like the mass modelling of rotation curves and mass-to-light ratios compared to the expected mass from stellar population syntheses models suggested the existence of dark matter composing the total mass of galaxies (Faber & Gallagher, 1979; Kent, 1986). That being the case, further studies of galaxy formation suggested a model that explained best the formation of galaxies composed with dark matter (White & Rees, 1978). With the new observational evidence gathered, the monolithic scenario could no longer completely describe all the aspects of the formation of galaxies.

The *hierarchical model* has been widely accepted (Baugh, 2006) since it was first debated (Peebles, 1982). Through the perspective of the  $\Lambda$ CDM (cold dark matter) cosmological model, large structures are built up over time by means of the continuous accretion of smaller structures. It proposes that the dark matter collapses and its density grows. The dark matter density fluctuations result in dark matter haloes that are followed by successive merging with much less massive haloes, producing more massive structures. Eventually, the massive dark matter haloes start accreting baryons (the visible matter), so galaxies can be interpreted as the product of evolution of baryonic matter within a much larger halo of dark matter. The diversified morphological types of galaxies are the result of different interactions; for instance, spiral galaxies would have been formed with few interactions, whereas elliptical galaxies would have been formed with more frequent mergers. In this bottom-up theory, the environment where the galaxies are settled is an important determining factor; for instance elliptical galaxies (which, as explained above, would be a result of several interactions) are predominant in galaxy clusters.

## 2.2 Stellar Populations

The concept of stellar populations was first introduced by Baade (1944) after observing two distinct groups of stars in different locations in the galaxy M31. The CMD of stellar populations can be matched with one or more isochrones. An isochrone at a given age is a curve that connects the evolutionary tracks of stars with the same initial

chemical abundance and varied masses at the same age in a HRD<sup>1</sup>, meaning that whilst time is constant the distinct points composing the isochrone have a different stellar initial mass value. Therefore, when one looks at the CMD of a stellar system (say a GC or a nearby galaxy), there is information about the age and metal content of all the stars we see. Hence the whole history of the system is encrypted in the CMD. Figure 2.4 shows four examples of isochrones, with same ages 5 Gyr (green and red) or 10 Gyr (black and blue) and with same metallicities  $Z = 0.0001$  (red and blue) or  $Z = 0.01$  (green and black), from the bottom of MS to the end of AGB stage.

Simple stellar populations (SSP) are composed of stars formed at the same time with the same initial chemical composition. One way to determine the parameters of a stellar population is to compare observed CMD with isochrones. While SSPs represent star clusters quite well, they are not a good approximation for galaxies, which are much more complex systems presenting several star formation episodes with different properties throughout the history of the system. Galaxies are populated by a distribution of stars that is a complex superposition of numerous isochrones, implying numerous generations of stars with different metallicities. Therefore, it can be assumed to be a composite stellar population. The inherent information that characterises a composite stellar population is the SFH, that is, the evolution with time of the total mass of stars formed and their initial chemical composition.

## 2.3 Globular clusters

In the late 17<sup>th</sup> and early 18<sup>th</sup> century, astronomers identified the first star clusters, but because of the low aperture and resolution of their telescopes they thought they had discovered nebulous stars. It was only with William Herschel in the late 18<sup>th</sup> century, possessing a much larger telescope, that it was possible to resolve the stars in the clusters. In his second catalogue publication (Herschel, 1789), he studied star clusters in detail and labelled them into separate groups, one of them being called

---

<sup>1</sup>A HRD is a plot of luminosity versus temperature of a star. The connection between luminosity and temperature gives the evolutionary stage of a star.

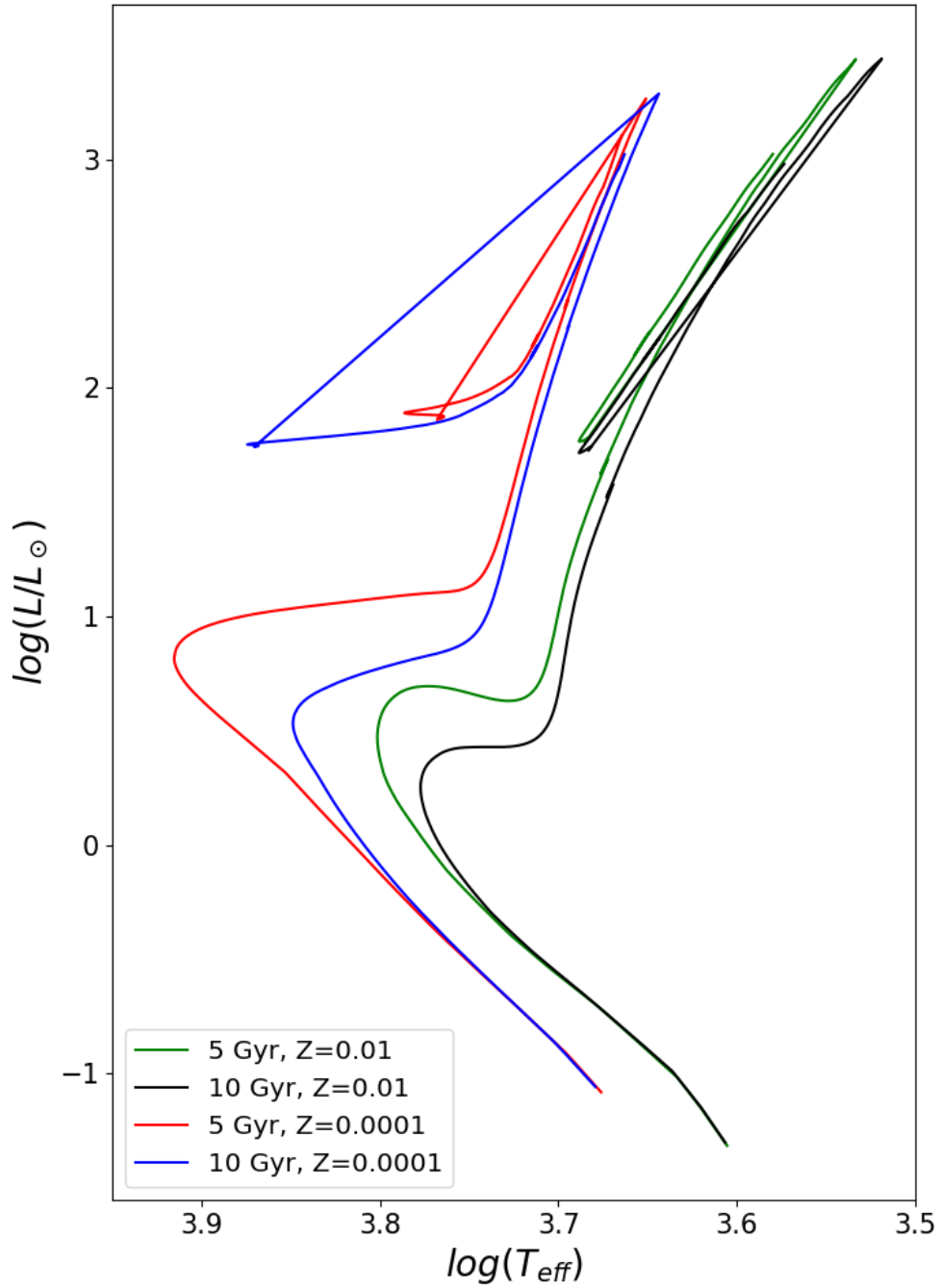


Figure 2.4: HRD of four isochrones (Pietrinferni et al., 2004), colours red and blue have same metallicity,  $Z = 0.0001$ , but different ages, 5 and 10 Gyr respectively; while green and black have metallicity  $Z = 0.01$ , but ages 5 and 10 Gyr.

'globular'. In the early 19<sup>th</sup> century, the advent of high-resolution spectroscopy and photometry improved results in the characteristics of the stellar cluster, such as their distance. Shapley (1918) used RR Lyrae and Cepheid variables to measure the distance to the known clusters and estimated their location in the Galaxy by calculating their distance to the Galactic centre.

Stars in GC are gravitationally bound, distributed according to a spherical geometry with higher stellar densities towards their centre and typically host up to  $10^6$  stars (Benacquista, 2002). Most of the stars in a GC tend to be faint, red stars located near the lower end of the MS. Because it is possible to fit a single isochrone to the HRD of a GC, this is evidence that stars within a GC have identical ages. In our galaxy (in this case we speak of Galactic globular clusters, GGC) about 150 have been identified (Harris, 1996), which are typically distributed in the halo and bulge. Overall GGC have ages from 10-13 Gyr (VandenBerg et al., 2013), which means that most stars have formed in the beginning of the universe and are important tracers of remote ages.

GCs are believed to have been formed by the collapse of a single molecular cloud. In fact, they are the best-known example of a SSP, formed by coeval stars with the same chemical composition. Because of their relative simplicity, GCs have historically been used as to validate stellar evolution models and to understand more complex systems, such as galaxies. While the definition of SSP can still be considered valid in good approximation, particularly with differences in the abundance of some metals, in recent decades the presence of multiple populations has been highlighted. It is possible to find a few peculiarities: for instance,  $\omega$  Centauri presents a wide range of metallicities (e.g. Norris & Da Costa, 1995; Pancino et al., 2002; Origlia et al., 2003), showing up to eight populations with varied Fe abundances ( $\Delta [Fe / H] \approx 1.5$  dex) and other heavy elements. The reader is referred to Bastian & Lardo (2018) for a broader discussion about multiple populations in other various GGCs.

## 2.4 Stellar evolution

The HRD describes the relation between the luminosity of a star and its effective temperature. The connection between luminosity and temperature gives the evolutionary stage of a star. GCs are examples of simple stellar populations and thus allow the study of different evolutionary phases of a population with fixed age and chemical composition. The ideal tool for this type of study is the CMD, the observational counterpart of the HRD. In a CMD, each star is defined by a color and a magnitude, corresponding respectively to the effective temperature and brightness. In the CMD of a GC, a star belongs to a certain sequence depending on the type of nuclear combustion that occurs in its core. Below are the main evolutionary phases that will be addressed in the next chapters.

### 2.4.1 Main Sequence

MS is the evolutionary stage where stars spend most of their lifetimes, and therefore the number of stars observed in this phase is considerably higher than in any other phase. The MS corresponds to the nuclear fusion of hydrogen in the core through the process called proton-proton chain (or simply pp chain), more effective for low mass stars, and CNO (carbon-nitrogen-oxygen) cycle, dominant in more massive stars. The increase of molecular weight in the core also increases the density and temperature, so that the star becomes somewhat more luminous and the outer envelope expands and cools down slightly. The position in the HRD moves towards the turn-off (TO) point. The MS ends with the exhaustion of hydrogen in the core, the contraction of the core and the expansion of the envelope. The timescale and how a star evolves depends on its initial mass and the kind of nuclear reaction that converts hydrogen to helium. In fact, each initial mass corresponds to a different central temperature, which favours different burning cycles. In particular:

- $M \leq 1.3 M_{\odot}$ : the hydrogen combustion occurs through the pp chain reaction

---

<sup>2</sup>All the mass range suggested in this section depends critically on the initial chemical composition

and the star core is radiative, whilst the stellar envelope is convective.

- $M > 1.3 M_{\odot}$ : the hydrogen burning occurs mainly through the CNO cycle and the core is convective surrounded by a radiative envelope.

The moment a star moves from the MS to the next evolutionary stage (subgiant branch) corresponds in the CMD to the TO point, which is equivalent to the brightest and warmest point of the MS in the HRD. Figures 2.5 and 2.6 show the evolutionary track of stars with 1 and 5  $M_{\odot}$ , respectively.

### 2.4.2 Sub-giant branch

This evolutionary phase (SGB) is characterized by the contraction of the core and the transition from core to shell combustion, through the CNO cycle. The luminosity of the stars during the SGB remains approximately constant. The temperature will rise in the core but not enough to trigger the helium nuclear fusion, though a thick hydrogen shell surrounding the core will start burning the hydrogen into helium. The shell will become thinner with the hydrogen depletion. The radiation emitted from the core and the shell during the rise of the core temperature causes a thermal expansion in the stellar envelope and the surface cools down. With the surface expanded and cooled, the formation of molecules and grains is more effective causing a rise in the opacity. Eventually, the core of low-mass stars will get dense enough to develop electron degeneracy and will stop contracting. In this phase the star moves towards the red part of the CMD. The timescale in the SGB is approximately a few Myr, nuclear timescales<sup>3</sup> for stars with core degeneration, and it tends to be shorter for stars with non-degenerate cores, which follows Kelvin-Helmholtz timescales<sup>4</sup>. Therefore the chance of a massive

---

of the stars.

<sup>3</sup>The nuclear timescale is given by the equation:  $t_{nuc} = \frac{0.007Mc^2}{L}$ , where  $M$  is the mass of the star,  $c$  is the speed of light and  $L$  is the stellar luminosity. 0.007 stems from the fact that fusing hydrogen to helium liberates roughly 0.7% of the available mass energy.

<sup>4</sup>Or thermal timescale, given by the equation:  $t_{KH} \propto \frac{GM^2}{RL}$ , where  $G$  is the gravitation constant and  $R$  is the stellar radius.

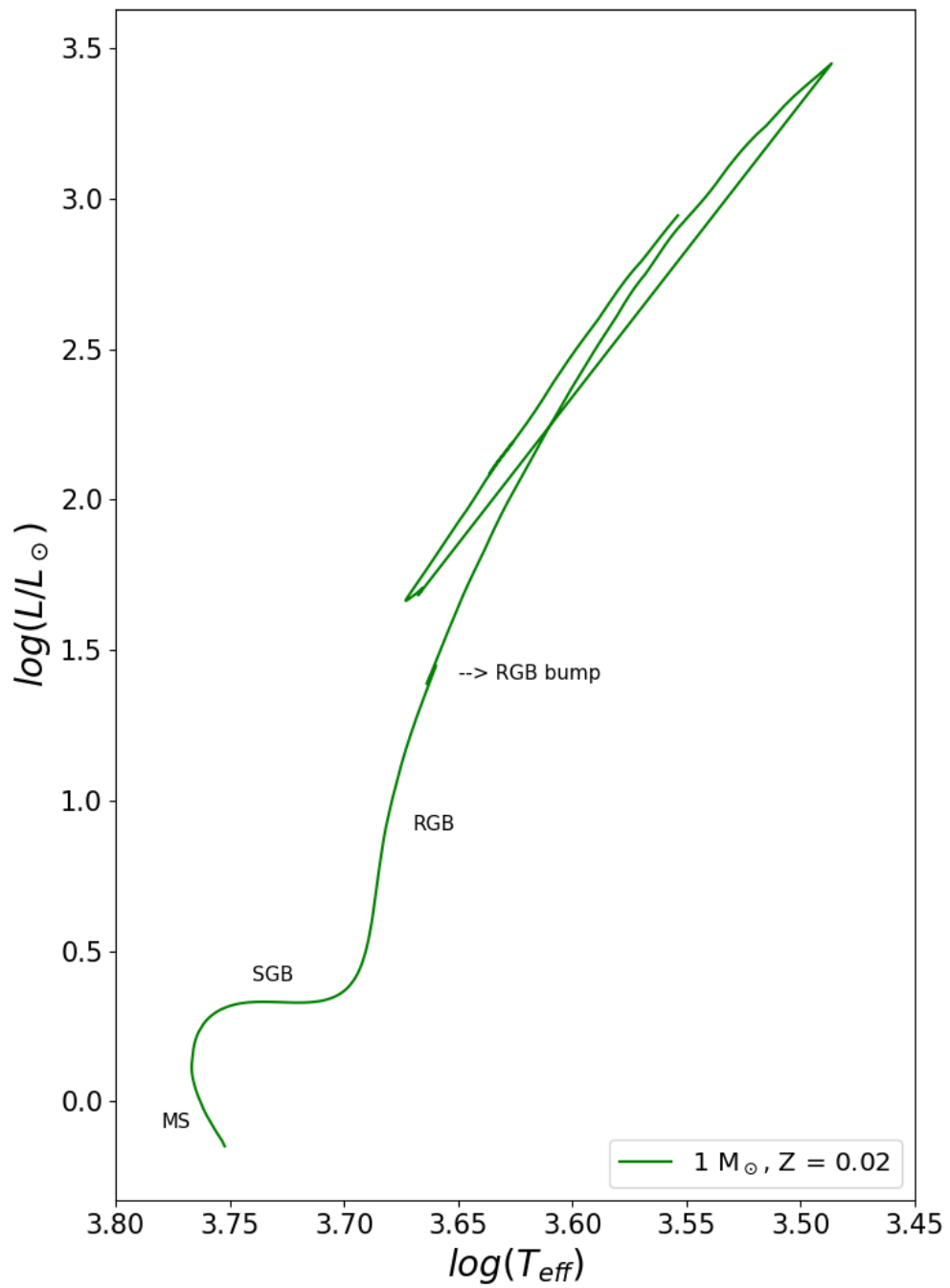


Figure 2.5: HRD of a  $1 M_{\odot}$  star's evolutionary track, considering metallicity  $Z = 0.02$ .

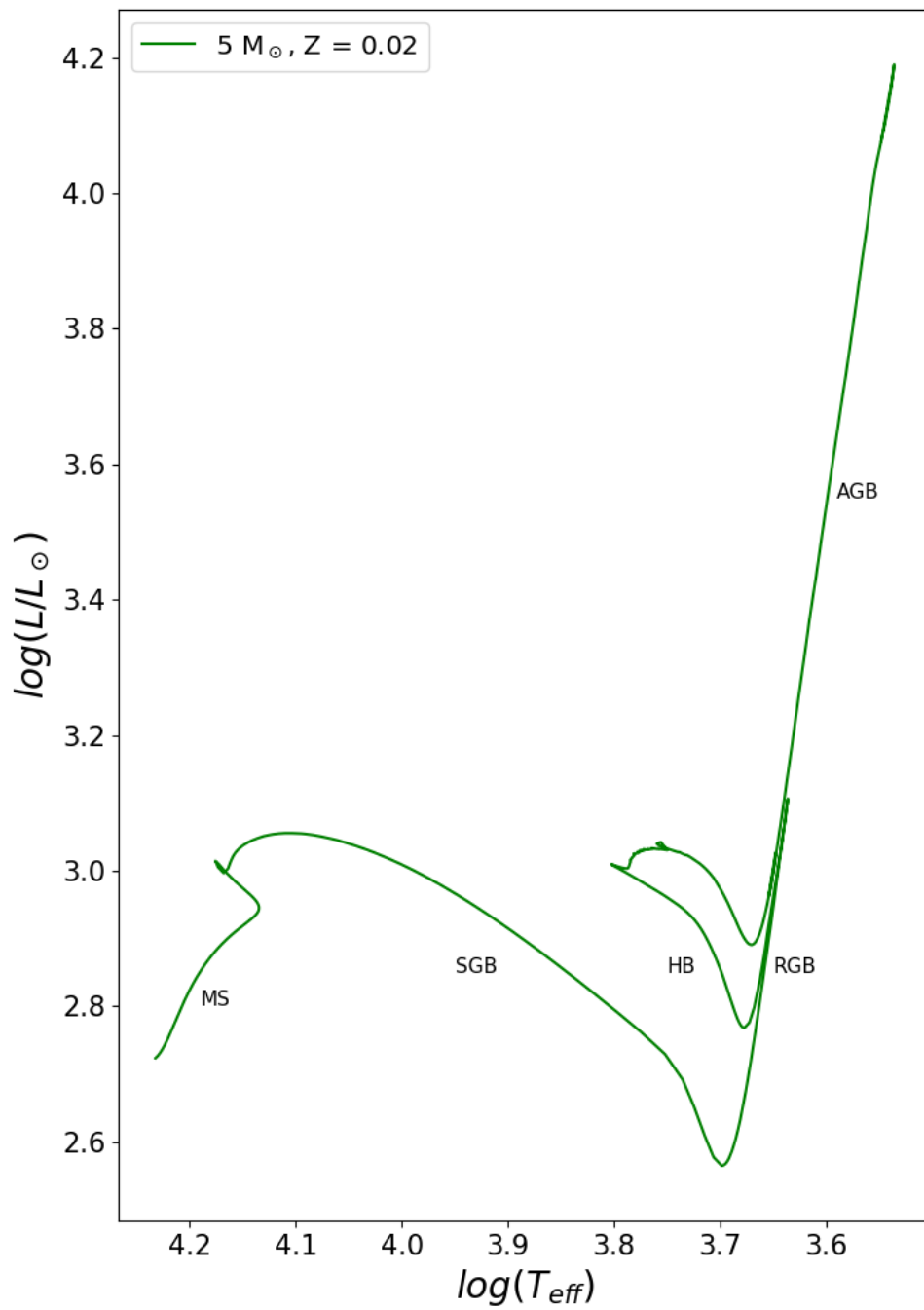


Figure 2.6: HRD of a  $5 M_{\odot}$  star's evolutionary track, considering metallicity  $Z = 0.02$

star being observed during its SGB phase is practically null, resulting in a lack of stars in the HRD, called Hertzsprung Gap.

### 2.4.3 Red giant branch

This phase is characterized by the burning of hydrogen into helium in a thin shell. In the HRD (or CMD), RGB stars follow an evolutionary path in a nearly vertical line. The way the RGB phase develops depends on the mass:

- $M \leq 2.3 M_{\odot}$ : the core is in degenerate conditions, so that the pressure does not depend on temperature. All the stellar luminosity is sustained by the radiation produced by a thin hydrogen burning shell. The convective zone penetrates deeply into the star, bringing up some of the helium produced by the core during the MS phase to the surface, enriching the chemical content of the stellar atmosphere with helium. This process is known as first *dredge-up*. By the time the core reaches  $T \approx 10^8$  K, a thermal instability happens, causing the helium ignition to burn explosively (He-flash), whose energy removes degeneracy. This trigger usually occurs when the core mass is  $\sim 0.5 M_{\odot}$ , regardless of the star's initial mass. This implies that the corresponding terminal region of the RGB, the RGB tip, has the same bolometric luminosity for all stars in this mass range. This, therefore, makes possible the use of this point as a standard candle to determine distances;
- $M > 2.3 M_{\odot}$ : in these stars the core is not degenerate, but in a perfect gas regime. For this reason, the ignition of the helium burn occurs in a thermo-regulated regime when the core reaches the required temperature and density ( $T \approx 10^8$  K and  $\rho \approx 10^4$  g cm<sup>-3</sup>).

A star with initial mass around  $0.8 M_{\odot}$  will typically lose about  $0.2 M_{\odot}$  during the RGB phase (Schatzman et al., 1993).

### 2.4.4 Horizontal branch

During the HB phase, the stable combustion of helium occurs in the core accompanied by the hydrogen burning in the shell. In all stars with core mass ( $M_c$ ) greater than  $\sim 0.5 M_\odot$ , helium burning in carbon and oxygen occurs independently of the value of the mass, through the  $3\alpha$  process. The placement of HB stars in the HRD depends on its initial mass:

- $M \leq 2.3 M_\odot$ : stars within this mass range have experienced helium flash and therefore all have  $M_c \sim 0.5 M_\odot$ . A star's position in HB depends on the ratio of core mass to total mass, hence essentially the amount of residual envelope. A thin envelope implies higher effective temperatures, so the star is positioned in the warmer zone of the HRD (in the blue part of the CMD), forming an extended horizontal arm. If, on the other hand, the amount of residual envelope is greater, the effective temperature is lower so the stars accumulate near the RGB, in the red side.
- $M > 2.3 M_\odot$ : as already mentioned, in this mass range the ignition of the burning of the helium takes place under non-degenerate conditions, when the appropriate conditions of temperature and density are verified. In this case, the increasing efficiency in energy production by the hydrogen envelope moves the star to the hot part of the HRD. The star reaches the bluest part of the HRD when the He abundance in the core reaches about 50% then moves back to the red.

After spending a few dozens mega years in the HB, the star has now a core made of degenerate carbon and oxygen (for stars more massive than  $8-10 M_\odot$  the carbon-oxygen core is not degenerate), surrounded by a helium-burning shell and on top of that a hydrogen-burning shell. The helium-burning shell releases a large amount of energy, causing the stellar envelope to expand and cool down.

### 2.4.5 Asymptotic giant branch

The AGB phase is characterized by hydrogen-burning shell on top of a helium-burning shell, while the carbon-oxygen core is inert. Similarly to the RGB phase, the stars in the AGB follow a basically vertical line in the CMD. In the end, AGB stars evolve to white dwarfs.

- $M \leq 6 - 8 M_{\odot}$ : the carbon-oxygen core is degenerate, in which the necessary conditions for the beginning of further nuclear reactions are never reached. The start of the helium nuclear reactions in the shell leads to a few consequences: the stellar surface luminosity drops, the hydrogen envelope expands and cools and the hydrogen burning turns off. Following that, the convection in the hydrogen envelope deepens carrying the elements processed by the CNO cycle and helium to the surface. This is the second dredge-up, which occurs only in stars with  $\sim 3 - 5 M_{\odot}$ .

After a first phase in which only the helium shell is active (early AGB), now the helium shell is turned off and the hydrogen shell reignites, accumulating helium in the layer between these two shells. The alternating ignition between the two shells defines the so-called thermal pulsing AGB (TPAGB) phase, which is a sudden increase of the luminosity repeatedly in a period of time (Schwarzschild & Härm, 1965; Weigert, 1965). During the TPAGB for stars with initial mass  $\geq 1.5 M_{\odot}$ , the convective envelope moves inwards, causing the third dredge-up, due to the envelope expansion and cooling caused by the thermal pulses. Carbon enriched stars, and hence carbon-rich dust, are the result of the third dredge-up episodes.

At the end of the TPAGB, the total ejection of the envelope around the degenerate core and contraction of the degenerate core occurs, until what remains of the star is the central core surrounded by the ejected dusty, cool cloud. The central source is observed in UV spectra whilst the dust cloud emits radiation in IR. The dust shell ionises the radiation and re-emits in the optical, producing the so-called planetary nebulae, and the central object is now a white dwarf.

For stars with initial mass  $M > 8 M_{\odot}$ , the core contracts and the temperature in the non-degenerate core is reached for the beginning of the carbon burning and the subsequent thermonuclear reactions until the synthesis of the elements of the iron group. The iron core determines the end of the evolution of massive stars. When the iron core mass approaches  $M_c \sim 1.4 M_{\odot}$ , the pressure of the degenerate electrons is no longer sufficient to sustain the structure; therefore the core collapses, causing the star to explode like a Type II supernova. The supernova explosion leaves a neutron star as a remnant if the stellar initial mass is less than  $\approx 25 M_{\odot}$  or, a black hole for larger masses.

## 2.5 Mass loss mechanisms

Stellar winds can be triggered by miscellaneous mechanisms, for instance coronal winds (driven by gas pressure; the ML here can be enhanced by associated magnetic winds), sound wave winds (driven by acoustic wave pressure), dust (or continuum) winds and line winds (both driven by radiation pressure), magnetic rotator wind and Alfvén wave winds (both driven by a magnetic field with and without rotation, respectively). The most efficient ML mechanisms, radiation-driven winds and Alfvén wave-driven winds, are described below (for a thorough review, see Lamers & Cassinelli, 1999).

### 2.5.1 Dust driven winds

Cool, luminous red super-giants and AGB stars are prone to undergo dust-driven winds. The effective temperature and the luminosity vary respectively from 2000 to 3000 K and from  $L \geq 10^4 L_{\odot}$  (for AGB) to  $L \geq 10^5 L_{\odot}$  (for super-giants). The stellar atmosphere is extended, lifting the gas to a certain distance from the photosphere. The low temperature allows grain formation and growth in the atmosphere forming a dust shell. The opacity blocking the radiation flux increases. The grain particles absorb and scatter the stellar radiation, momentum is transferred from the radiation to the gas

resulting in an acceleration of the dust in an outwards direction. Grain acceleration is increased to over the sound speed and a drag force on the gas molecules is produced by their collision and coupling with the dust, triggering a stellar wind. Photon absorption by dust and grains happens in a wide wavelength range; that is why the outflow of cool giant stars in this process is also called continuum-driven wind.

The minimum ML rate for dust-driven winds is usually about  $10^{-7} M_{\odot} \text{ yr}^{-1}$  and the maximum is about  $10^{-5} M_{\odot} \text{ yr}^{-1}$  (when taking into account thermal pulsations) and the wind terminal speed is slow, about 10 to 30  $\text{ km s}^{-1}$ . The grain size is typically between  $0.05 \mu\text{m}$  and  $0.1 \mu\text{m}$ . O-rich stars with  $\text{C/O} < 1$  produce silicate grains (common composition:  $\text{Mg}_2\text{SiO}_4$  or  $\text{MgSiO}_3$ ) and C-rich stars with  $\text{C/O} > 1$  produce carbonaceous grains (common composition: SiC, MgS or Fe). Stars with a normal atmospheric abundance, like M super-giants, usually have silicates winds. Both C-rich and O-rich atmospheres with carbon or silicate grains ignite grain condensation at a temperature of about 1500 K. The radiation by dust in the winds is observed at long wavelengths. Dust emission produces a peculiar energy distribution, forming like a bump in the IR, similar to a Planck Function with  $T \approx 10^2$  to  $10^3$  K. The bump wavelength is related to the dust average temperature.

### 2.5.2 Line-driven winds

Hot, luminous stars have a great amount of absorption lines, particularly in the ultraviolet where most of their radiation is emitted. The stellar atmosphere of these massive stars is no longer in hydrodynamic equilibrium, consequently the radiation and gas pressure take over the gravity, pushing the mass outwards (Lucy & Solomon, 1970). All the stellar photosphere radiation at the exact excitation frequency would be absorbed or scattered in the inner layers of the atmosphere in a static system and the outer layers would not interact directly with the radiation; thus reducing the radiation velocity. However, if the gas is accelerating, the ions will then absorb photons that are red-shifted in regards to the photons absorbed in the layers downward; which means that the interaction of the gas, that is moving outwards, with the radiation coming

from the photosphere results in a even more accelerated gas. The efficiency of this process depends on the amount of exciting or ionising radiation. Stars from different evolutionary stages can experience this ML mechanism (MS, giants and O, B and A super-giants, planetary nebulae central stars and white dwarfs). The ML rate for line driven winds is usually about  $10^{-5} M_{\odot} \text{ yr}^{-1}$  and the wind terminal speed is larger than  $10^3 \text{ km s}^{-1}$ .

### 2.5.3 Alfvén wave driven winds

Alfvén wave is a low-frequency hydromagnetic wave, which results from electromagnetic oscillations. Alfvén waves are transverse waves, which means that the particle oscillation is perpendicular to the direction of the wave propagation. In stars, the wind driven by Alfvén waves is a consequence of an acceleration in the photosphere caused by the energy and momentum dissipation from the charged particles carried by the wave. The outflow velocity varies accordingly to the magnetic field and the particle densities and is typically high, reaching up to  $700 \text{ km s}^{-1}$  for Sun-like stars. This process along with the two radiative processes described above are the most effective ML mechanisms. Stars that may present Alfvén wave winds are: MS stars of spectral type B, low mass pre-MS, giants and super-giants with effective temperatures between 3000 K and 15000 K.

## 2.6 Photometry

In order to study any celestial body one needs to acquire information about it by observing and accounting for the amount of light arriving at the detectors from a specific object, for instance through the method called photometry. Therefore, photometry can be defined as the measurement of the electromagnetic radiation distribution coming from an object. The telescope collects the radiation from a celestial source, but detecting devices are the ones responsible for detecting, recording and measuring the amount of light.

In the past, photographic plates were used to capture the flux emitted by celestial bodies and the magnitudes were calculated visually. Photographic plates were ideal to simultaneously observe multiple objects, but the measurement accuracy was limited and with low quantum efficiency. Quantum efficiency is a measure of how many incoming photons are counted by the detector, as some are always lost. Nowadays, charge coupled devices (CCD) are used to electronically record the electromagnetic radiation. CCD is a silicon chip, divided into smaller individual pieces called pixels. A photon is detected after colliding with the semi-conductor material and exciting an electron from the valence band to the conduction band, then being captured by an electrode. During the reading, the electrons are transported to an analogue to digital converter, that transforms the charge into a number which is proportional to the number of photons fallen in each pixel. The output afterwards is a digital image.

### 2.6.1 Photometric filter systems

Observations must be limited to certain wavelengths regions, either by the atmosphere, or by the detectors used. To standardize and compare observations of different objects, and also to get information about some stellar properties, sets of photometric filters are used. The sensitivity to the radiation depends on the spectral efficiency of the telescope, the detector and the passband. There are several photometric systems with a variety of filters to choose from. Each photometric system has a set of standard stars with known apparent magnitude measured at a specific filter. Photometric systems are divided in three categories, according to their bandwidths; broadband filters are usually wider than  $40 \mu\text{m}$ , intermediate band are between  $7$  and  $40 \mu\text{m}$  wide and narrow band are narrower than  $7 \mu\text{m}$ . Figures 2.7 and 2.8 show the comparison of a few broadband systems in the optical and infrared, respectively, by Bessell (2005).

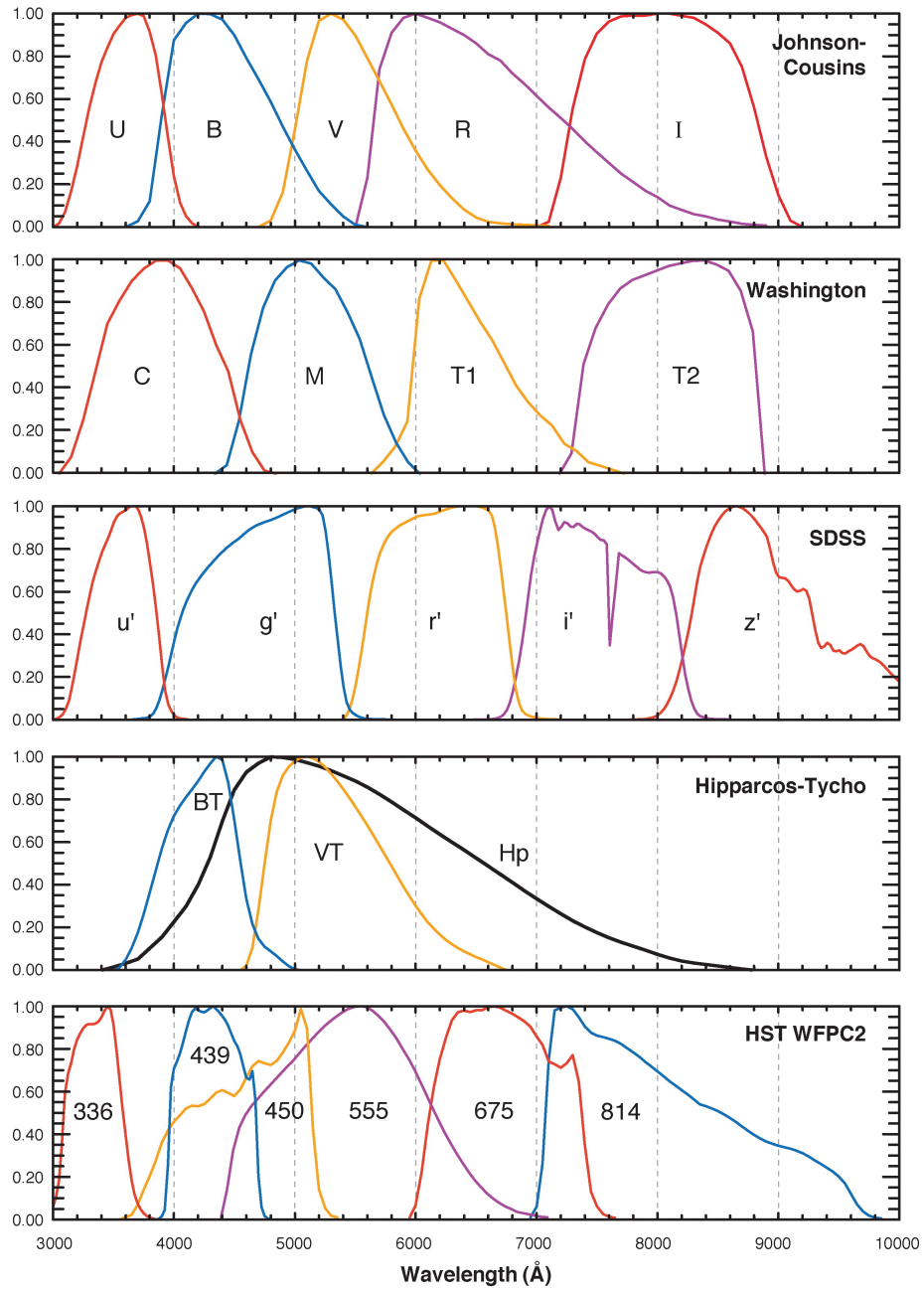


Figure 2.7: Passband comparison of optical broadband systems by Bessell (2005).

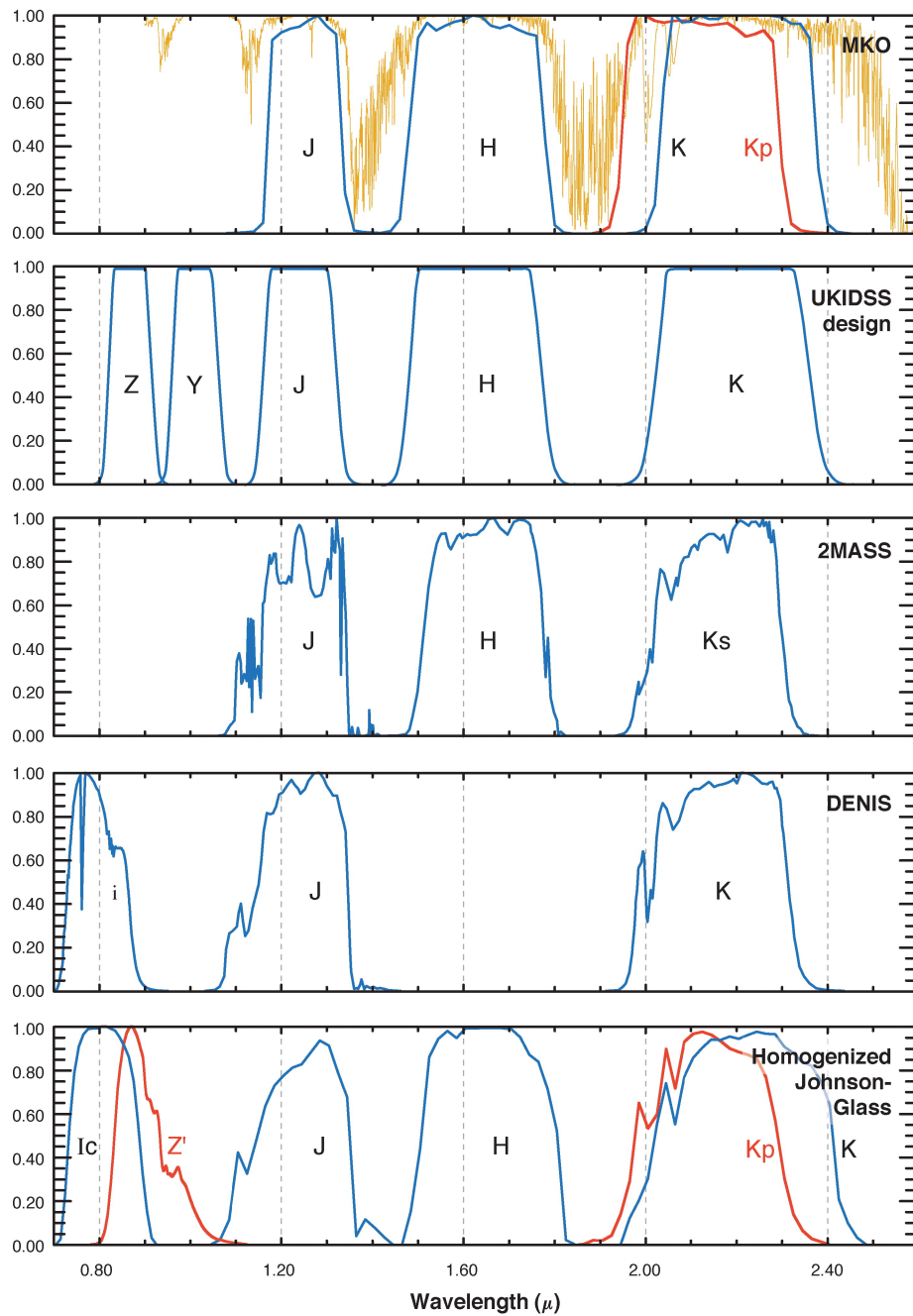


Figure 2.8: Passband comparison of infrared broadband systems by Bessell (2005).

## 2.6.2 Interstellar extinction

The interstellar medium is composed of dust and gas and they interact with the stellar radiation. The dust grains absorb and isotropically scatter the starlight, resulting in the so called extinction. The amount of extinction can be different from galaxy to galaxy and from direction to direction within the same galaxy, because variations in sizes and chemical composition of the dust grains affect the interactions with photons. The extinction caused by dust grains is stronger at short wavelengths, resulting in the so called interstellar reddening.

Extinction  $A_\lambda$  can be defined in terms of the reduction of intensity by the presence of dust:  $A_\lambda = -2.5 \log \left( \frac{I_\lambda}{I_{\lambda 0}} \right) \equiv -2.5 \log(e^{-\tau_\lambda})$ , where  $I_\lambda$  is the observed intensity and  $I_{\lambda 0}$  is the intensity at the wavelength  $\lambda$  that would be observed if there was no extinction and  $\tau_\lambda$  is the optical depth. Should the distance and luminosity of the source be known, the extinction can be written in terms of the magnitude:  $m_\lambda = M_\lambda - 5 \log(d) + 5 + A_\lambda$ , where  $m_\lambda$  is the apparent magnitude,  $M_\lambda$  is the absolute magnitude and  $d$  is the distance. Colour excess is other measure of extinction:  $E(B - V) = A_B - A_V = (B - V) - (B - V)_0$ , in the photometric B and V bands.

The extinction law describes the dependence of extinction with wavelength and is commonly expressed in the form of a ratio of colour excesses:  $\frac{E(\lambda - V)}{E(B - V)}$  or like  $\frac{A_\lambda}{A_V}$ . The extinction ratio  $R_V = \frac{A_V}{E(B - V)}$  characterizes the steepness of the extinction curve. The extinction curve is usually determined by comparing a reddened stars flux distribution with a dereddened one (with same spectral type and luminosity).  $R_V$  is 3.1 for the Galactic average extinction curve, reaching up to  $\sim 5.5$  in dark clouds (Fitzpatrick, 1999). Figure 2.9 is an example of an extinction curve for  $R_V = 3.1$  from the far-IR through the UV derived by Fitzpatrick (1999).

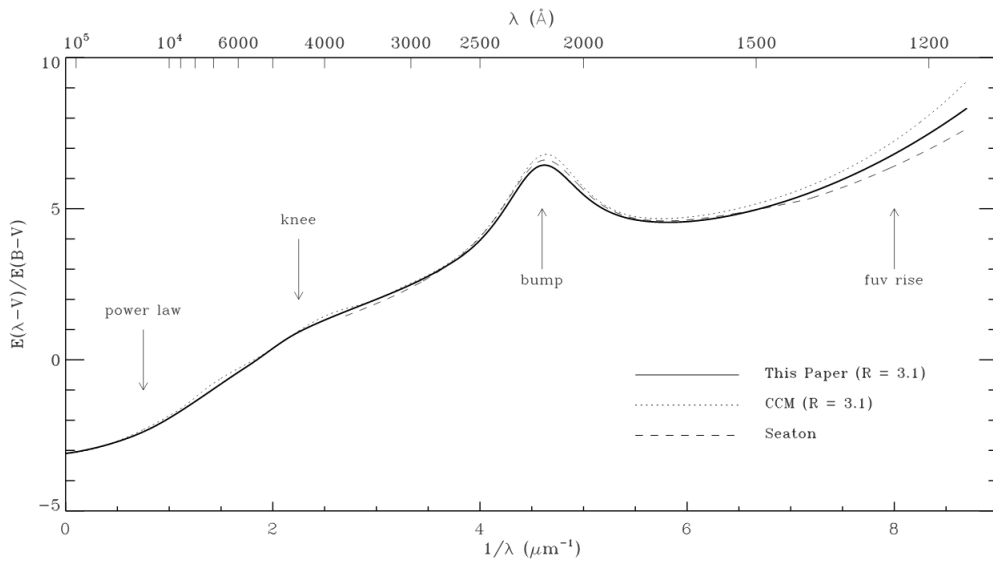


Figure 2.9: Normalized interstellar extinction curves from the far-IR through the UV. Solid curve is derived by Fitzpatrick (1999) based on  $R \equiv A_V/E(B - V) = 3.1$ , further curves were plotted for comparison by the author.

# Chapter 3

## Photometric observations

In this chapter is presented a description of the photometry performed for both data sets, for M33 and  $\omega$  Cen. The softwares used for this task were DAOPHOT and IRAF. The observational data taken from *Spitzer*-IRAC for the GC  $\omega$  Centauri are in the following channels: 3.6, 4.5, 5.8 and 8  $\mu m$ . The final catalogue assembles about 4000 stars. Our observations for the galaxy M33 come from the CFHT in the filters g', r' and i'. The final catalogue accumulates about a million stars.

### 3.1 Data reduction and analysis

Photometry is the technique of measuring the amount of radiation emitted from a celestial object. To interpret the observed flux from a point source, all the recorded light is summed and the sky background is subtracted. Point spread function (PSF)-fitting photometry considers individual stellar profile, and it is the technique applied for this data, since it may disentangle fluxes that could overlap due to the high stellar density. Aperture photometry is also applied later on to compensate any “lost” flux due a smaller aperture radius chosen in the PSF-fitting to not include any neighbour star.

The photometric analysis was performed using the software DAOPHOT (Stetson, 1987), a program specially designed to obtain the positions of stars and magnitudes in digital

two-dimensional images, and particularly efficient in conditions of high stellar density. The software needs some input information about the images. In particular, the gain and readout noise must be known. These two values are listed in the header of the images used and, in each case, their values are respectively equal to  $22 e^-/\text{ADU}$  (analogue-to-digital unit) and  $0.8 \text{ ADU}$  for the CFHT/gri and  $3.3 e^-/\text{ADU}$  and  $0.5 \text{ ADU}$  for the IRAC/filters 3.6, 4.5, 5.8,  $8\mu\text{m}$ .

Also, the full width at half maximum (FWHM) for the PSF of the stars in the field should be calculated. PSF are expected to be circularly symmetric. The angular size of a PSF can be measured by a FWHM which is the diameter where the flux falls to half its central value. The FWHM was estimated using the IRAF/DAOEDIT task; a sample of  $\approx 40$  isolated and bright stars for  $\omega$  Cen, and for M33 there were two distinct samples: a mixture of 200 bright and 600 faint stars for the crowded regions and 80 bright and 50 faint stars for the uncrowded regions. On average, the FWHM was about 5 pixels ( $1''$ ) for the CFHT/gri and about 2 pixels ( $2.4''$ ) for the IRAC/filters 3.6, 4.5, 5.8,  $8\mu\text{m}$ .

Another parameter that must be known a priori is the saturation level of the image. Saturation is determined essentially by the maximum pixel value at which the detector becomes saturated. In the case of CFHT/gri, this level is about 4000, 5000, 6000 ADU ( $g'$ ,  $r'$ ,  $i'$ ) and for the IRAC/filters 3.6, 4.5, 5.8,  $8\mu\text{m}$  this level is about 2000 ADU.

The first step of the reduction is to identify the stellar objects present in the image. This step is performed by the DAOPHOT/FIND task. For this purpose, a threshold level is defined, measured in units of standard deviations from the background value of the image, above which stellar sources are identified. The latter is determined in a circular area at a fixed distance from the star's source. To detect weak sources one should reduce the threshold value. The threshold values assumed for the CFHT/gri are  $2, 3, 4 \sigma$  and  $1 \sigma$  for the IRAC/filters 3.6, 4.5, 5.8,  $8\mu\text{m}$ . The output of the procedure is a text file, with the .coo extension, which contains for each detected object: an identification number, the x- and y-coordinates of the centroid, a magnitude measured from the assumed threshold level, and the roundness and ellipticity indexes of the star. These latter two parameters are useful for evaluating whether the detected object is

actually a star, by avoiding in this passage the inclusion of objects having a particularly elongated shape, very bright single pixels (so-called hot pixels) or cosmic rays.

The derivation of an appropriate PSF model is essential for accurate and reliable magnitude measurements. DAOPHOT has four options of PSF analytical models, among which the one that best represents the data is chosen. The analytical models available are, in particular, the functions of Gauss, Lorentz, Moffat and Penny.

The Gaussian function has two free parameters, namely the half-width at half-maximum in  $x$  and  $y$ . It may therefore have an elliptical shape, but the ellipse orientation is restricted, to make the calculation faster. The Lorentzian function has three parameters: the half-width at half-maximum in  $x$  and  $y$  and the angle with which the major axis of the ellipse is described. The Moffat function has the same free parameters as the Lorentzian.

The Penny function consists of the sum of a Gaussian function and a Lorentzian function, which may have an elliptical shape and be tilted relative to the  $x$  and  $y$  directions of the image. Two versions of the Penny function are available. In the first case, the orientation of the ellipse representing the Lorentzian is limited, while the Gaussian orientation is free. Therefore, there are four free parameters: the half-width at half-maximum in  $x$  and  $y$ , the fractional amplitude of the Gaussian function at the peak of the stellar profile and the angle of rotation of the major axis of the ellipse representing the last one. In the second case, both the ellipses representing the Gaussian and the representative of the Lorentzian can rotate. The free parameters are the same as in the first Penny function plus the angle of rotation of the major axis of the two ellipses representing the Lorentzian function.

The PSF model is calculated by comparing the possible analytical models, with the profile of a sample of stars, appropriately selected (i.e., the most isolated and bright, but not saturated) by the PSF task. This task calculates the best fit of one or more analytical functions in relation to the data and determines the value of the residuals (by a  $\chi^2$  test). It is at the discretion of the user to choose whether the program should use a particular analytical function, or whether the residuals should be calculated for

each of the available functions, only by choosing the best case (for this work, the latter option was chosen). Another parameter set by the user is the degree of variability of the PSF as a function of the instrumental coordinates. Given the significant deformation, depending on the position, the variability was set to return the best function during the calculations.

The best PSF template for each image in the dataset is applied to the entire list of stars through the ALLSTAR program. The output consists of: magnitude, error,  $\chi^2$  and sharpness based on the PSF model obtained in the previous step; all this information is saved in a text file with the .als extension. When ALLSTAR outputs are available for all available images, they must be combined for a preliminary catalogue of the dataset.

### 3.1.1 M33

The photometric data used in this work were obtained with the Queue Service Observing mode using the MegaPrime/MegaCam wide-field mosaic imager on the 3.6 m CFHT. The observations were taken on 27 distinct nights between August 2003 and January 2005, for the g', r' and i' band filters with exposure times ranging from 8 to 11 minutes. The MegaPrime/MegaCam instrument has 36 individual CCDs of  $2048 \times 4612$  pixels<sup>2</sup>, 1 degree  $\times$  1 degree field of view and a high angular resolution of 0".187 per pixel. The seeing values of all analysed images are from 0.6 - 1". All the images were pre-processed by the CFHT's Elixir pipeline, which performs dark and bias and sky subtraction, flat-fielding and fringe corrections and merge amplifiers. More details about the observations and the data reduction can be found in Hartman et al. (2006). The master image, of size  $20220 \times 20531$  pixels<sup>2</sup>, which is a composition of at least 33 images for each separate filter as a result of the pipeline mentioned above, was trimmed and split in smaller sub-images of  $2048 \times 2048$  pixels<sup>2</sup> in order to facilitate the image manipulation. All sub-images were trimmed leaving an overlapping area, with respect to its neighbour sub-image, of 300 pixels between each sub-image. These overlapping regions are necessary to not lose any star in the cutting-line and also to estimate the uncertainty in the magnitude measurement. Figure 3.1 exemplifies the

trimming and the sub-images overlapping; where the black lines are the edges of each sub-image and the blue rectangles represents the spatial location of each chip over the sub-images used for the magnitude calibration, that will be described in 3.1.1.

Photometry was performed according to the description in section 3.1. To improve the photometric results, the photometry was performed again in the subtracted image of the first pass, obtaining an improved second-generation PSF<sup>1</sup> over this subtracted image. An aperture radius of 4 pixels was adopted for the magnitude measurements and the background sky was determined in an annulus with inner radius of 16 pixels and an outer radius of 32 pixels.

A good PSF is adjusted ideally for a bright, non-saturated and isolated star. In a crowded field it is really difficult to pick such a candidate, so the use of as many PSF stars as possible in the fitting process is important to improve the signal-to-noise ratio of the PSF. What the fitting routine does is that every time a star is added, the position is shifted and the brightness is scaled to guarantee that the centroid of each star added matches with the previous one as precisely as possible. The script allows us to determine the number of bright and faint stars that will be picked to be fitted by the PSF, as it is important to consider some faint stars for crowded fields. The number of PSF stars vary for each sub-image, especially for crowded regions because extremely crowded regions make the constructions of point-spread functions quite challenging. An example of the PSF fitting performed in an uncrowded and in a crowded field is shown in Figure 3.2.

Selection cuts were applied on the final catalogue based on the DAOPHOT parameters  $\sigma$  (photometric errors from DAOPHOT),  $\chi^2$  and *sharpness* to try determining, from all sources obtained with the photometry, which ones were most likely to be stars and exclude any spurious sources. The range of values of each parameter varies according to the sample of each sub-image. A visual inspection of the images of the rejected sources was done to guarantee they were correctly discarded.

$\chi^2$  is the goodness of fit parameter, relative to the profile star fit quality in relation to

---

<sup>1</sup>The two-dimensional brightness distribution produced in the detector by the image of an unresolved source.

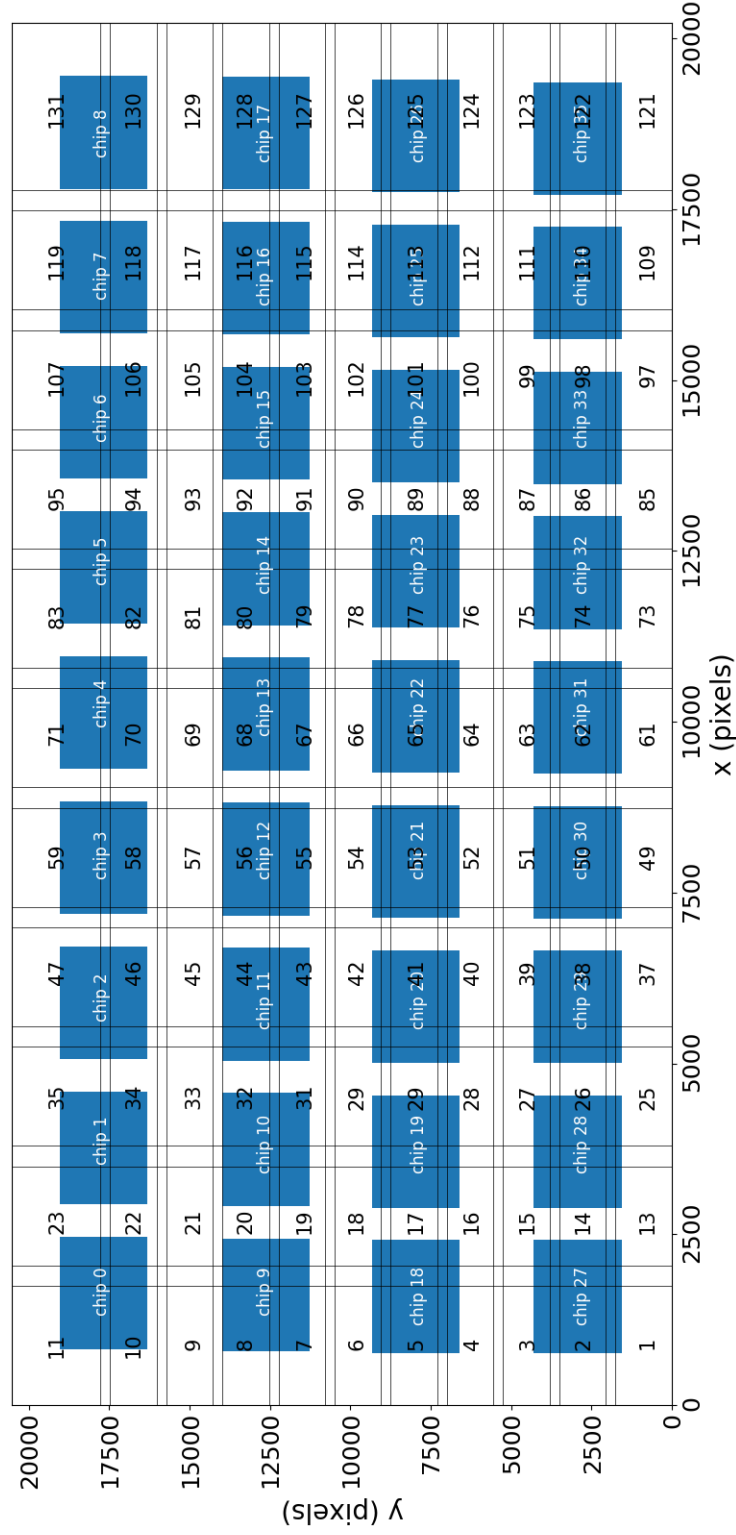


Figure 3.1: Sub-image vs chip positions. The black lines are the boundaries between each sub-image and the blue rectangles are the position of the chips used for the magnitude calibration.

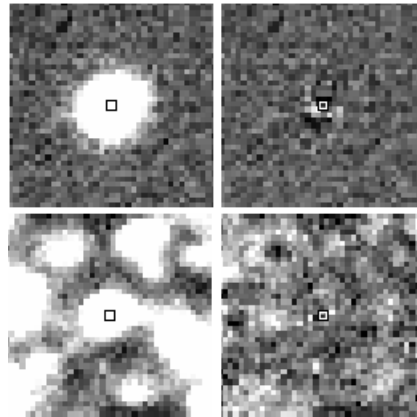


Figure 3.2: Illustration of the PSF subtraction. First column corresponds to the original images while the second column corresponds to the residual images after PSF subtraction. First row corresponds to a single star of a non-crowded field and second row corresponds to a crowded field. Each image is shown with the same grey-scale intensity and same pixel size, with north up and east to the left.

the assumed model. A large value of  $\chi$  is likely to be a non-stellar object. *Sharpness* is a parameter to establish the image quality, an index that measures how much the profile detected is broader or narrower. For a single, isolated, resolved star its value should be around zero, whereas large positive values of this parameter, containing hot pixels, usually indicate that the object is, for instance, resolved galaxies or unrecognised blended double stars. Large negative values, on the other hand, could be from bad pixels, cosmic rays or blemishes. Figure 3.3 illustrates the behaviour of the described parameters in a somewhat crowded image portion.

In the overlap region between sub-images, each star had the magnitude measured from each individual sub-image. This allows a comparison of the photometry done in different sub-images. A best match in the coordinates of the overlapping areas was done applying a matching radius of 1 pixel. After this, the photometric measurements of the stars that were located in the regions of overlap between different sub-images were compared. If the method was perfect, the magnitude difference would be expected to be around zero and the dispersion should increase, as the magnitude gets fainter where the photometric error ( $\sigma$ ) is higher. However, for a few cases, as examples seen in Figure 3.4 there was a slight trend.

To understand the reason for the slope in the magnitude differences among a few sub-

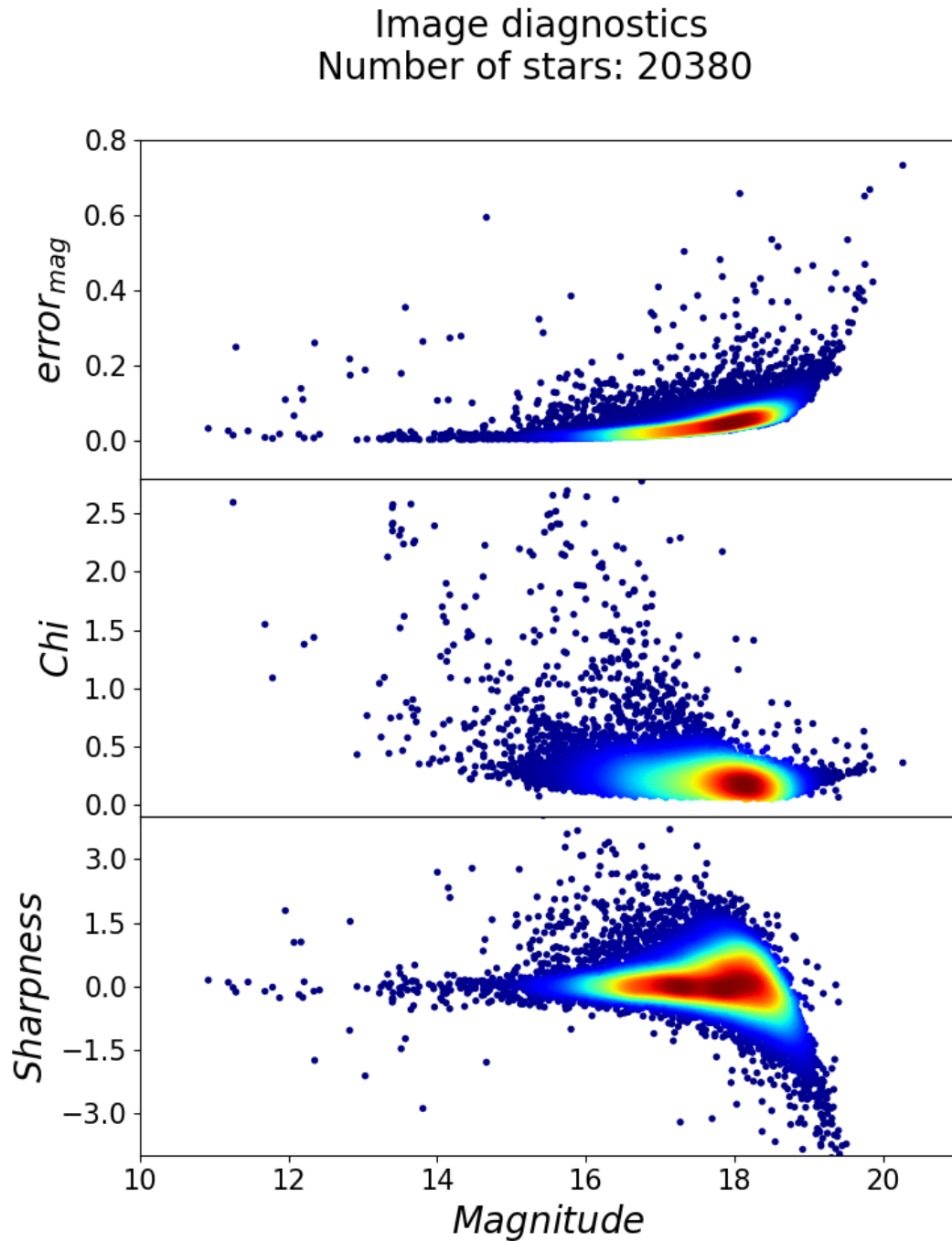


Figure 3.3: Top panel is  $\sigma$ , increasing as the magnitudes get fainter expectedly due to a higher uncertainty in the photometric magnitude determination of faint sources. Middle panel is  $\chi^2$  and bottom panel is *sharpness*.

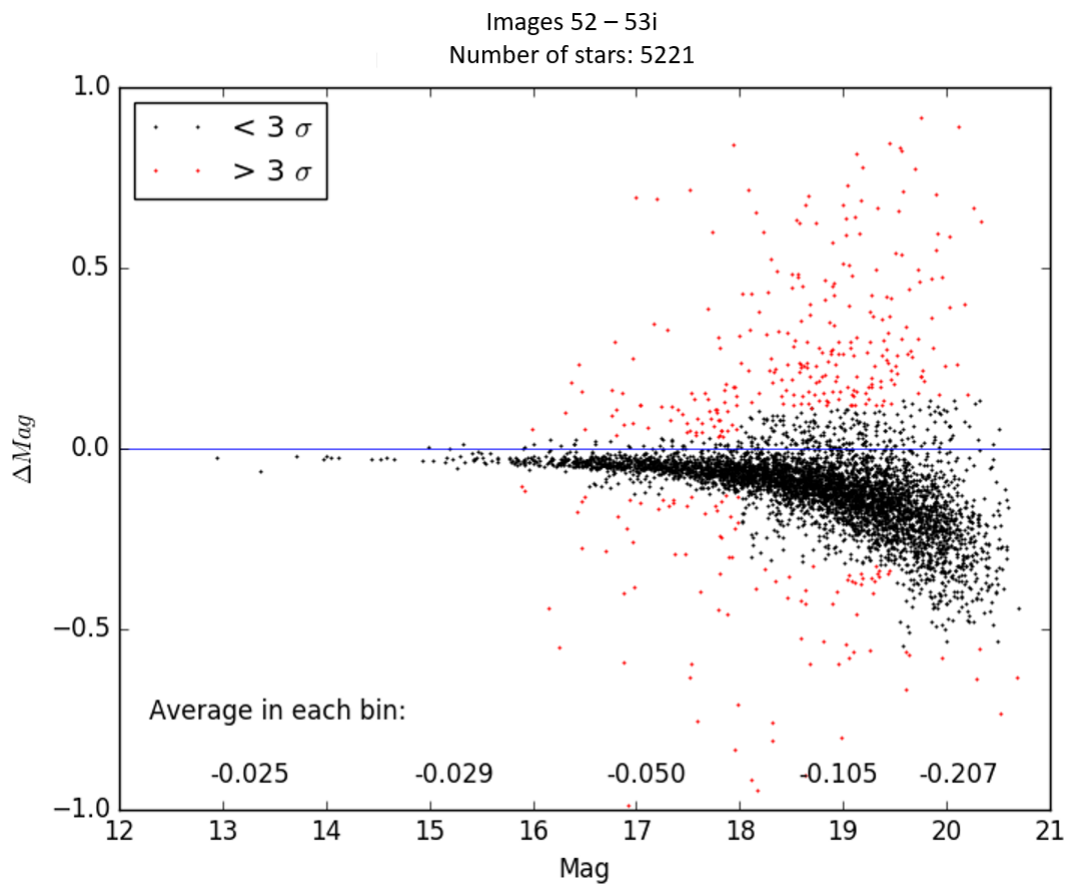


Figure 3.4: Comparison between the output magnitudes taken from an overlap region of sub-images 52 and 53. The black dots represent differences with dispersion below  $3\sigma$  while red dots represent differences with dispersion above  $3\sigma$ . To quantify how many stars are scattered by more than  $3\sigma$ , the magnitudes were averaged in five magnitude bins.

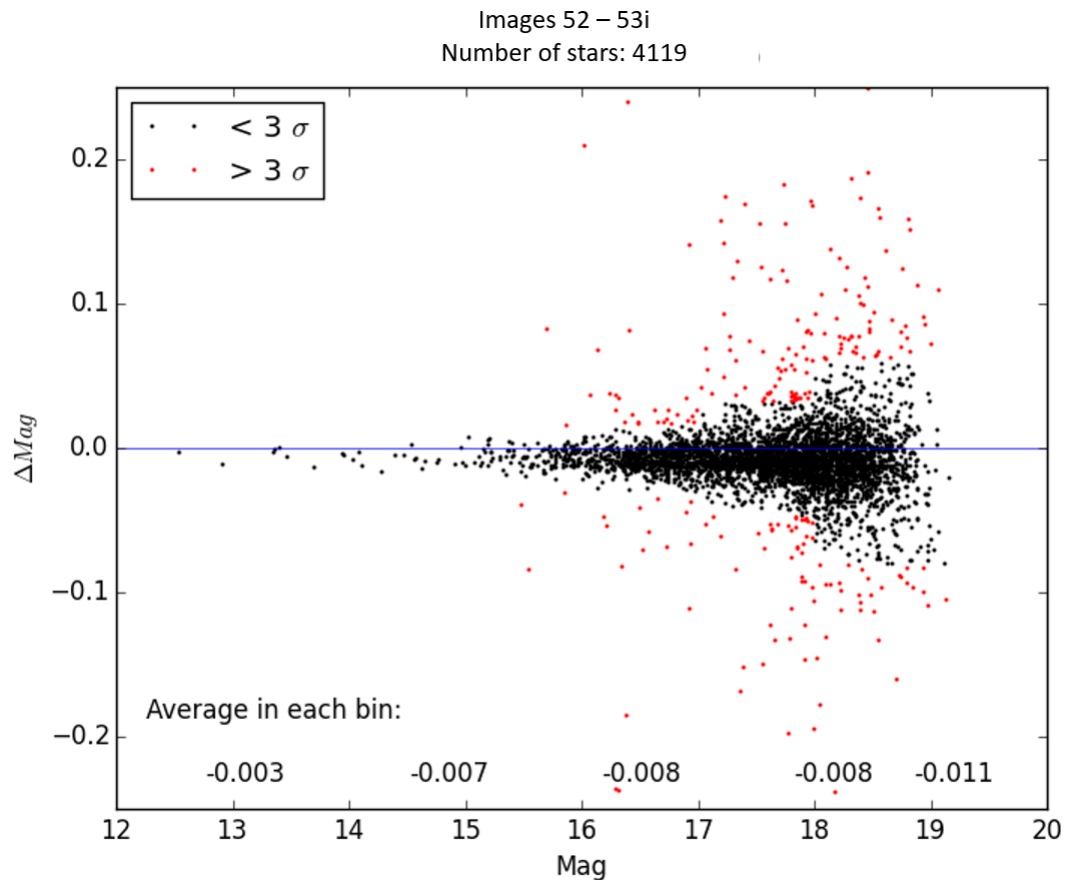


Figure 3.5: Same as 3.4 but the photometry performed for this set considered a higher sky background, eliminating the slope affecting the faint magnitudes seen in 3.4.

images, the number of PSF stars and gain and readout noise (RON) values were tested. Somehow, the noise statistics of the image were miscalculated after the stacking and the sky removal in the course of data reduction. This means that pixels that would be considered too noisy to be part of the PSF calculation suddenly become good when the RON is low. Adding an *artificial* sky background equivalent to the subtracted sky and rerunning the photometry with higher RON and saturation level values seemed to overcome this issue. DAOPHOT should consider a much higher noise in this way and get less stars for the PSF fitting. Therefore, sky background of about 800 ( $g'$ ), 1500 ( $r'$ ) and 2000 ( $i'$ ) was added to each sub-image of all three filters and the photometry was redone. Figure 3.5 shows the improvement after adding the sky background.

### Photometric corrections

Aperture photometry consists essentially of calculating the brightness of each star within an area, generally of a circular shape, for each star identified in the previous passage. The value of the sky, also in this case, is determined in a concentric ring outside the area used to obtain the magnitude of the star. Although this approach is extremely simple, it is not capable of disentangling the contributions of individual components; therefore, it is unsuitable for accurate photometry in dense stellar systems, such as GC. However, aperture photometry provides a relative ranking in terms of brightness, between identified sources, which is useful for subsequent steps in the analysis. The calculation is performed by the IRAF/PHOT task, which uses the yields of the input file .coo from FIND, a list of diverse aperture radii (up to 20) provided by the user, and the internal radius of the outer ring in which the sky is calculated. The output result is a text file, with .ap extension, in which identifier and pixel coordinates of the star (same as the previous coordinate file) are reported, instrumental magnitudes detected in each of the apertures used and related errors, and the value of the sky is determined with relative errors.

When doing PSF-fitting photometry the larger the aperture, the more of the star's flux is within the radius, though the larger the sky error from the sky noise will be. That is why it is important to do an aperture correction, to correct the limited size of the aperture radius and guarantee that the aperture is large enough to contain most of the star flux with the minimum sky noise.

The task IRAF/MKAPFILE was used to compute a growth curve of the magnitude in a given aperture versus the aperture radius. The aperture correction was calculated separately for each sub-image. Firstly, subtracted images were generated with the PSF stars on it, then the task IRAF/PHOT was run again to measure the flux of the isolated stars considering radii range from 15 (the aperture radius used in the first photometry) to 20 pixels. Then, IRAF/MKAPFILE integrates the adopted curve of growth between the smallest and the largest aperture. The observed curve is weighted to favour the small aperture radius whilst the theoretical curve favours the largest radius. The al-

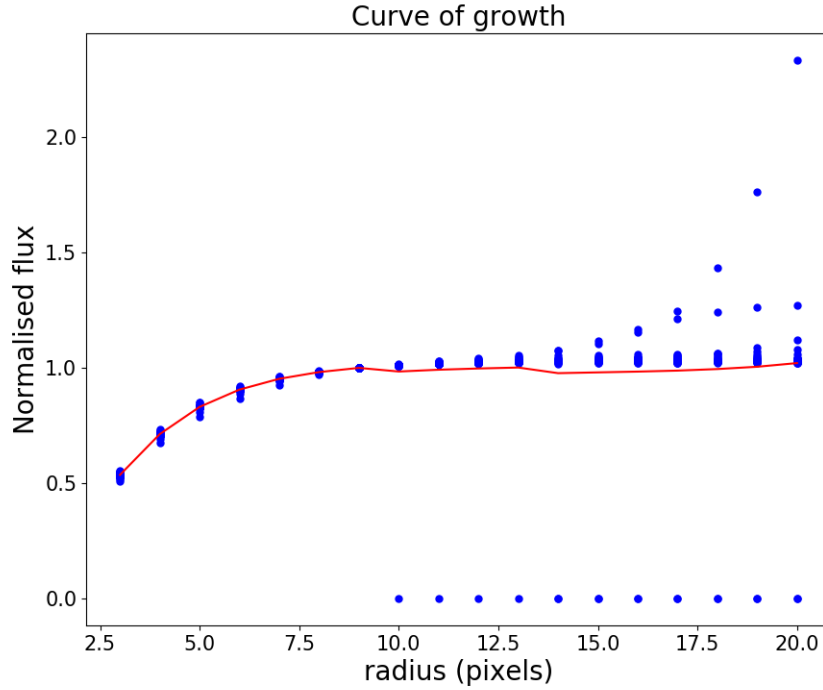


Figure 3.6: Plot of the flux versus the radius (in units of pixels) for the PSF stars of a given sub-image. The solid red line is the average flux.

gorithm used in IRAF/MKAPFILE is called DAOGROW (Stetson, 1990). Aperture growth-curve correction to all photometric measurements were applied correcting all stars with respect to their sub-image correction values. Each sub-image had its aperture correction value determined (see table A.1) and applied to the magnitudes of all stars within it. Figure 3.6 shows an example of the fluxes measured in a given radius for several PSF stars of a given image. The solid line represents the average curve of growth.

An offset correction was also applied in the magnitudes to correct for a zero point among the sub-images. A “reference” sub-image was selected for each filter as a zero point. The criteria for this selection were a sub-image with high star density and with the least magnitude dispersion. Thus, the average of the magnitude difference between the reference sub-image and its neighbour was calculated:

$$\text{offset}_{\text{factor}} = \frac{1}{n} \sum_{i=1}^n \mu_{\text{img1}} - \mu_{\text{img2}} \quad (3.1)$$

where  $\mu_{img1}$  is the magnitude from sub-image 1 and  $\mu_{img2}$  is the magnitude from sub-image 2. The error associated to this offset factor was calculated according to the following:

$$\sigma_{offset} = \sqrt{\frac{1}{\sum_{i=1}^n \left(\frac{1}{\sigma_i^2}\right)}} \quad (3.2)$$

where  $\sigma_i^2 = \sigma_{img1}^2 + \sigma_{img2}^2$ .

The offset factor was subtracted from all the stars of the reference sub-image neighbour related to those offset, and from the corrected sub-image a new offset factor was determined, to be applied to a new sub-image neighbour. For each new correction a new offset was generated to keep correcting all the sub-images of the mosaic. The final magnitude error of an individual star accounting for the offset correction was determined as follows:

$$\sigma_{mag} = \sqrt{\sigma_{apc}^2 + \sigma_{offset}^2} \quad (3.3)$$

where  $\sigma_{apc}$  is the magnitude error after the aperture correction and  $\sigma_{offset}$  is the error associated to the offset correction factor. To see the offset values applied to each individual sub-image refer to the table A.2.

The  $r'$ ,  $g'-r'$  and  $i'$ ,  $g'-i'$  CMDs for M33 are shown in figures 3.7 and 3.8. MS stars are around the colour  $-0.2$ , red super-giant stars are in the upper-right around 1.1, RGB stars around 1.3 and the AGB stars are in a slightly horizontal around 2.0. There is also a foreground contamination of Galactic stars around the colour 0.5.

### Photometric calibration

Instrumental magnitudes should be transformed into magnitudes in a standard photometric system<sup>2</sup>, such as SDSS system. The final magnitudes were calibrated based on

<sup>2</sup>A standard photometric system is defined by a list of magnitudes and colours for standard stars, well distributed over the whole sky, for a set of specific filters.

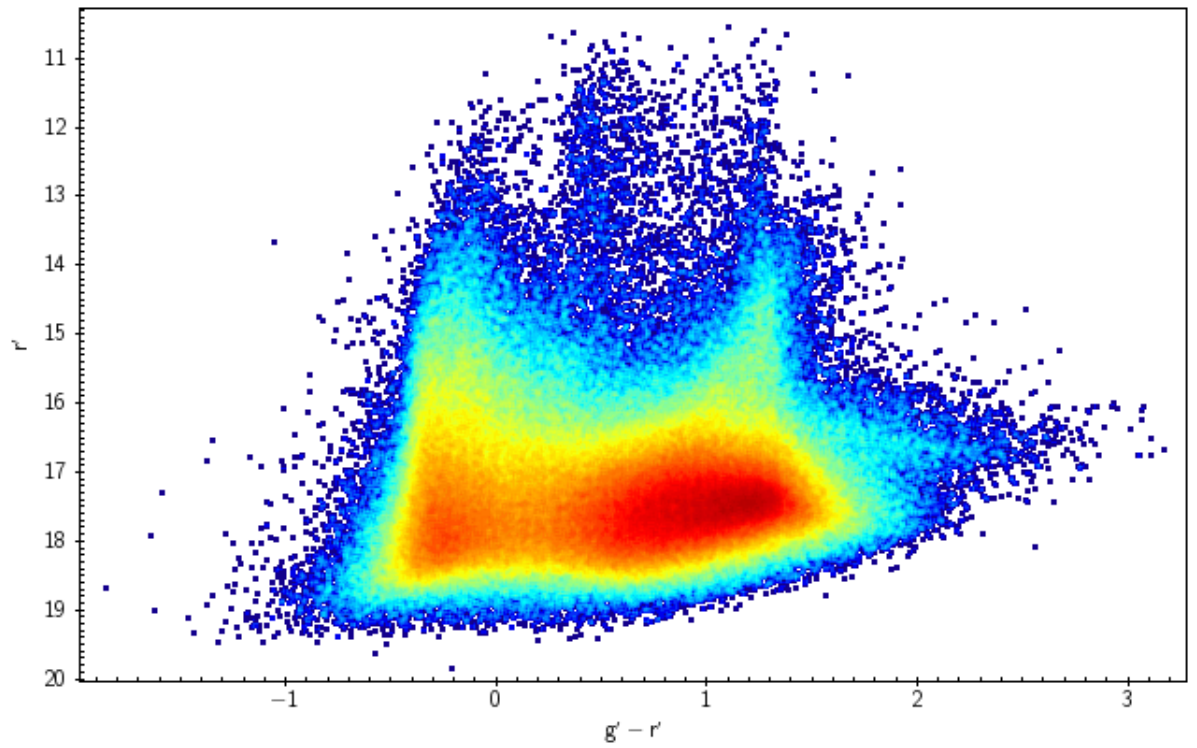
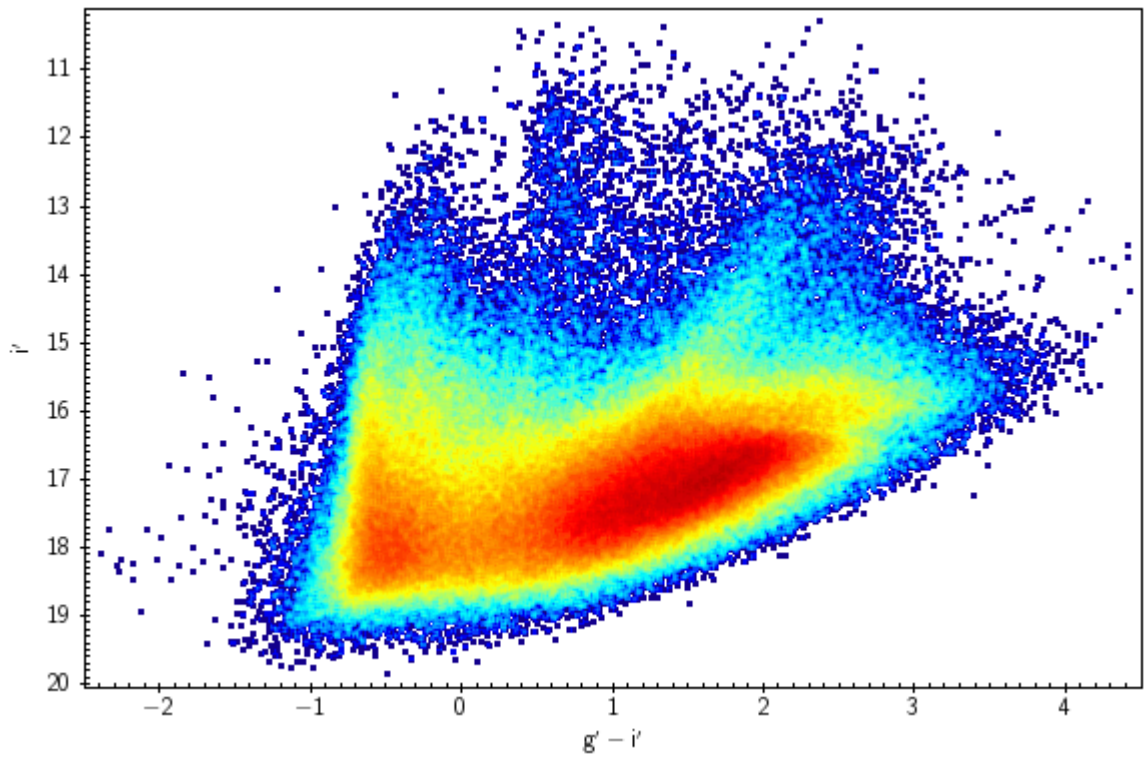
Figure 3.7: Colour-Magnitude Diagram,  $g' - r'$  versus  $r'$ .Figure 3.8: Colour-Magnitude Diagram,  $g' - i'$  versus  $i'$ .

Table 3.1: Average of the chip’s photometric solutions for zero point, colour term and coefficients  $A_*$  in g’, r’ and i’ filters. For a full table, with individual chip solutions fitted by KT, please refer to A.3.

filter	$Z$	$C$	$A_1$	$A_2$
g’	-29.656	-0.177	$-1.605e - 5$	$-5.437e - 6$
r’	-29.736	-0.020	$-2.418e - 5$	$4.129e - 6$
i’	-30.233	-0.069	$-1.174e - 7$	$2.044e - 6$

the transformation equations and solutions that a fellow student, Kevin Tsang (hereafter KT), determined from the photometric catalogues of Isaac Newton Telescope (INT) and CFHT observations. The stacked images are composed of 36 chips, from which result independent colour terms. IRAF/FITPARAMS is the task that transforms the magnitudes, by fitting the equation to a set data points, and once the coefficients are determined they can be used to calibrate the final magnitudes. The adopted transformation equation by KT is:

$$m_{inst} = m_{stand} + Z + C \times (colour)_{stand} + A_1 \times x_m + A_2 \times y_m \quad (3.4)$$

where  $m_{inst}$  is the instrumental magnitude from CFHT,  $m_{stand}$  is the magnitude from the INT standard stars,  $Z$  is the zero point between the standard and instrumental systems,  $C$  is the colour correction terms,  $colour_{stand}$  is the standard colours (g’ - r’) to calibrate g’ and r’ magnitudes and (r’ - i’) to calibrate i’ magnitudes,  $A_*$  are additional coefficients, which are used to improve accuracy. See the average of all chips for each parameter in table 3.1. The axial coordinates were included in the calibration equation for the purpose of accounting for any possible existing radial distortion since the CFHT covers a large region of the sky.

Usually, the use of colour terms in calibrations is appropriate when there is an uncertainty in the match between the instrumental and standard system or when a high precision photometry is aimed so any tiny discrepancy between instrumental and standard system must be corrected for. To obtain a more accurate result, more complex equations should be used by introducing additional terms.

Prior to applying the solutions in the dataset of this work and have the instrumental

magnitudes properly standardized, it was necessary to relate the fields from the sub-images to the field in each separate chip. Figure 3.1 shows the sub-images labelled from 1 to 131 and the chips over the sub-images numbered from 0 to 35. As per say, sub-images 10 and 11 relate to the chip 0, sub-images 22, 23, 34 and 35 relate to the chip 1, and so on. The correlation between the two dataset was done visually.

The zero-point offset between this work's dataset and KT's dataset had to be corrected beforehand. This was done considering the offset per chip, per filter, in order to maximize the accuracy. The matching radius applied in the cross-match between the two dataset was 1 pixel. Then, all stars with instrumental magnitude lower than 17 in this work's dataset were selected and the average of the difference between those magnitudes and KT's magnitudes were defined. The standard error for this average was calculated according to  $\frac{\sigma_{mag<17}}{\sqrt{N_*}}$  where  $\sigma_{mag<17}$  is the standard deviation and  $N_*$  is the total number of stars in the sample. Each chip were treated individually and the average offset corrections applied was about  $24.930 \pm 0.003$ ,  $24.880 \pm 0.002$  and  $24.901 \pm 0.003$  for g', r' and i' respectively.

Once the two catalogues were on the same zero-point, it was possible to apply the calibration transformation using an IRAF task. IRAF/INVERTFIT is the task that inverts the transformation equations using the values produced by IRAF/FITPARAMS to compute magnitudes and colours. As chip 8 does not present a photometric solution, for all the stars that have fallen in that particular field it was considered the coefficients found for the neighbour field, chip 7. The final catalogue with g', r' and i' magnitudes contains about 400000 stars. Figures 3.9, 3.10 and 3.11 show the comparison between the calibrated magnitudes from this work's dataset and KT's dataset. The large dispersion for g' and i' filters is probably due to cross-correlation between the two catalogues, as the axial coordinates present in KT's catalogue refers to the r' filter.

### **Cleaning the catalogue from repeated stars**

When the master image of M33 were trimmed into smaller images to facilitate the handling to perform the photometry, an overlap between each sub-image were allowed

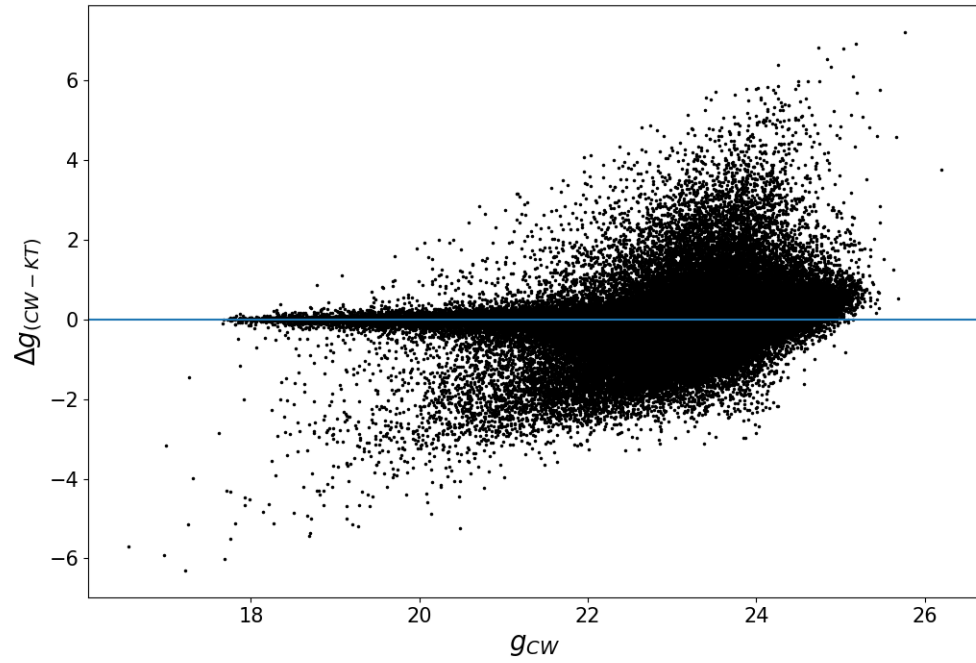


Figure 3.9: Comparison between the calibrated magnitudes from this current work (CW) dataset and KT's dataset for  $g'$  filter.

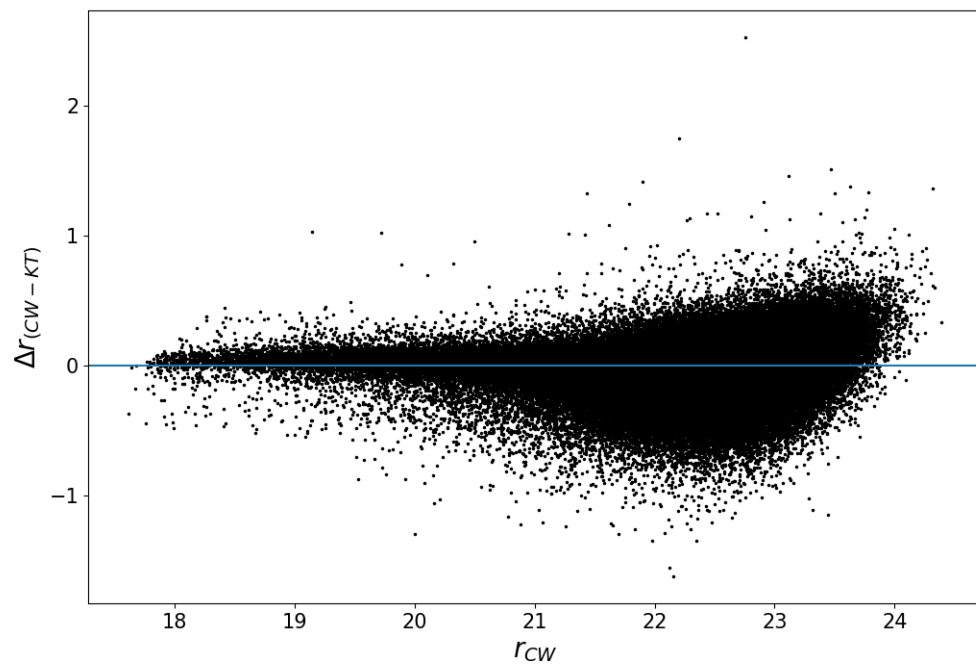


Figure 3.10: Comparison between the calibrated magnitudes from this current work (CW) dataset and KT's dataset for  $r'$  filter.

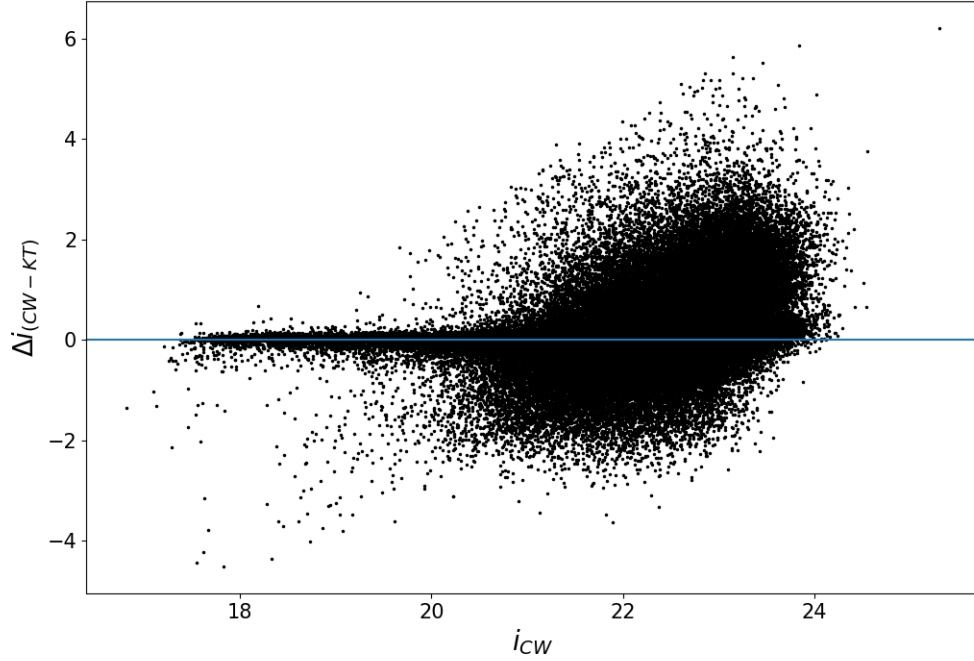


Figure 3.11: Comparison between the calibrated magnitudes from this current work (CW) dataset and KT's dataset for  $i'$  filter.

to guarantee that all stars were accounted for and to ensure the comparison between images. Basically, an overlap area of  $1748 \times 300$  pixels<sup>2</sup> exists in each image, which means that stars falling in that region may appear twice in the catalogue, or up to 4 times in an overlap area of  $300 \times 300$  pixels<sup>2</sup> for regions that overlap in 4 sub-images.

To reduce the appearance of an individual star to a single event, the photometric errors of the recurrent stars were compared and the one with the smaller error were chosen to remain in the catalogue. The match amongst the sub-images considered a 2 pixels matching radius. Overall, 26% of the stars in each filter were redundant and, therefore, eliminated from the final catalogue.

### 3.1.2 $\omega$ Cen

Photometric observations were taken on *Spitzer* Space Telescope with IRAC between September 2005 and July 2006. Images were observed in the channels 3.6, 4.5, 5.8 and

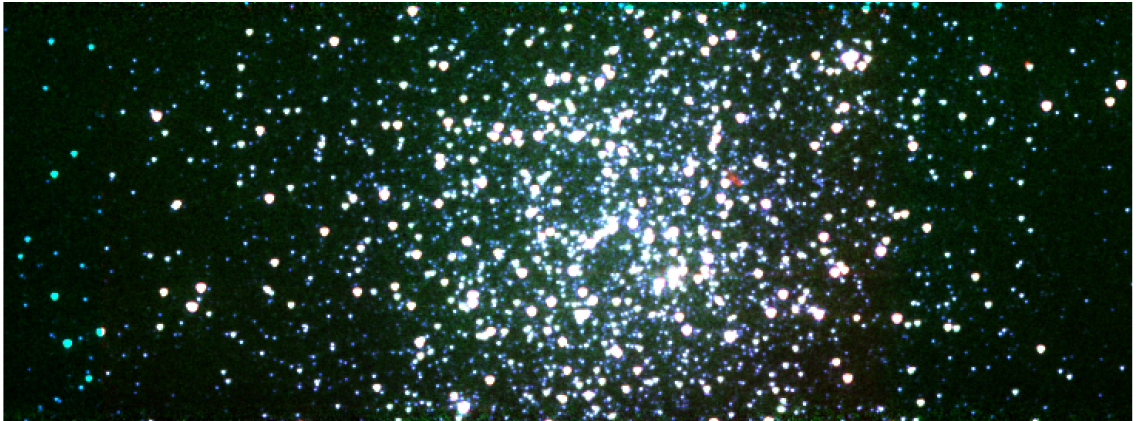


Figure 3.12: Three colour image of  $\omega$  Cen. Red is  $8 \mu m$ , green is  $5.8 \mu m$  and blue is  $3.6 \mu m$ .

$8 \mu m$  in short- and long-exposure times, covering a  $5' \times 5'$  field of view (Origlia et al., 2007, 2014). Figure 3.12 shows the three colour ( $3.6$ ,  $5.8$  and  $8 \mu m$ ) image of  $\omega$  Cen.

The PSF was set to vary linearly with position in the frame and was constructed from about 40 bright, relatively isolated stars widely spread throughout the entire image, except that the cluster core was avoided due to crowding. Specific details about PSF-fitting and data reduction have already been explained previously on section 3.1. The instrumental magnitude error was averaged in magnitude bins, and all objects falling above  $1\sigma$  limit were rejected to refine the photometric results.

A few hundredths of magnitude offset in colour were detected between the short- and long-exposure frames. To account for this offset we have taken an average of the magnitude difference (between the long- and short-exposures) within a 2.0 dex magnitude bin, and added it to the magnitude of the short-exposure frames. Then, the short- and long-exposure photometry lists were merged. Stars brighter than the instrumental magnitude 19.5 (where there was no saturation level) in  $8 \mu m$  were selected from the short-exposure while fainter ones were selected from the long-exposure photometry.

The match between the stellar positions for common stars in all channels and the final mid-IR catalogue compilation was done using DAOMATCH/DAOMASTER. DAOMATCH does a first approximation match for the stars based on the .als files and produces a .mch file with the coordinate transformations, rotation in degrees and pixel offsets. DAOMASTER is run to the catalogues of all images related to the same filter

based on the .mch and finds a more accurate match: the resulting magnitudes are the weighted average of the individual exposures and the error is the standard deviation, based on the error values of the individual exposures. At the end of this step, therefore, there are four .mag files, corresponding to each of the four filters 3.6, 4.5, 5.8 and 8  $\mu m$ , and containing the identifier of each star, mean position in x and y, magnitude and error, mean value of  $\chi^2$  and sharpness.

After obtaining the catalogues of the individual photometric bands, they can be combined into a catalogue containing the four magnitudes of each star. This step is an important check of the validity of the reduction procedure carried out up to this point. The procedure again uses DAOMATCH and DAOMASTER. With the former one obtains the transformations between the reference images of each photometric band, which are then improved by the second one when generating the common catalogue. In this case, it was required that the stars in the catalogue to be detected in at least two filters of which the data set is composed. The information contained in the output file of this procedure (.raw extension) is the same as in .mag files, with the only difference being that there are as many columns containing the magnitude and relative error as many photometric bands are used.

The instrumental magnitude of each star was converted into the Vega magnitude system by using the zero-magnitude flux densities of Reach et al. (2005). The following equation was used to calibrate the magnitudes:

$$M = M_{inst} + 2.5\log(F_{dens}) - 2.5\log(C) - 2.5\log(\Omega^2) \quad (3.5)$$

where  $M_{inst}$  is the instrumental magnitude,  $F_{dens}$  and  $C$  are the flux densities and the absolute calibrator factors (see values for each band in the table 3.2) and  $\Omega$  is the pixel solid angle<sup>3</sup>. The terms of the aperture correction and the position dependency are corrections used to reach higher accuracy, as it accounts for the detector responses in the different bands.

The multi-band photometric combination allows for the characterization of the stars in

---

<sup>3</sup>The side of a pixel is equivalent to 1".22.

Table 3.2: Flux densities and absolute calibrator factors for the channels 3.6, 4.5, 5.8 and 8  $\mu m$  derived by Reach et al. (2005).

<i>Channel</i>	<i>F<sub>dens</sub> (Jy)</i>	<i>C (MJy sr<sup>-1</sup>/DN s<sup>-1</sup>)<sup>a</sup></i>
1	280.9 ± 4.1	0.1088 ± 0.0022
2	179.7 ± 2.6	0.1388 ± 0.0027
3	115.0 ± 1.7	0.5952 ± 0.0121
4	64.13 ± 0.94	0.2021 ± 0.0041

<sup>a</sup>where DN refers to data numbers

the CMD and the identification of stars with colour excess. The mid-IR photometry has been cross-correlated with a complementary ground-based near-IR catalogue. The following catalogues SOFI <sup>4</sup> and 2MASS <sup>5</sup> were used for the central region, approximately 300 pixels radius from the centre of the cluster, and for the external region respectively. The catalogues from Marino et al. (2011) and Johnson & Pilachowski (2010) in the optical band have been cross-correlated with the mid- and near-IR photometry list. In particular, cross-correlation was done using CataXCorr<sup>6</sup> software.

Once the final, calibrated and astrometric catalogues have been obtained, the last step is to assign a flag or a label indicating each quality to each star. Particularly, each star, for each filter, has been assigned an integer equal to 1 in the case of stars considered of excellent quality or equal to 0 in case of lower quality. The assignment was made based on the photometric error associated with the magnitude in each filter, following the approach described below. The magnitude distribution was binned; for each bin the average of the photometric error and the standard deviation associated with it were calculated. The obtained values were interpolated by a *spline* to fit a curve representing the location where the average deviation is equal to  $1\sigma$ . The assignment of the flags was done using this curve as a reference: in particular, the stars positioned above the curve were marked with flags equal to 0, those below it with flags equal to 1. The final catalogue contains about 4000 stars. Figure 3.13 shows CMDs in the colours: (K -

<sup>4</sup>SOFI is an infrared spectrograph and imaging camera at the New Technology Telescope of the European Southern Observatory (Sollima et al., 2004)

<sup>5</sup>Two Micron All Sky Survey

<sup>6</sup>CataXCorr is a software dedicated to cross-correlation of stellar catalogues designed specifically for accurate astrometric solutions. It was developed by Paolo Montegriffo at the INAF - Bologna Astronomical Observatory. The CataPack package, of which CataXCorr is part, is available in <http://davide2.bo.astro.it/~paolo/Main/CataPack.html>

3.6), (K - 4.5), (K - 5.8) and (K - 8).

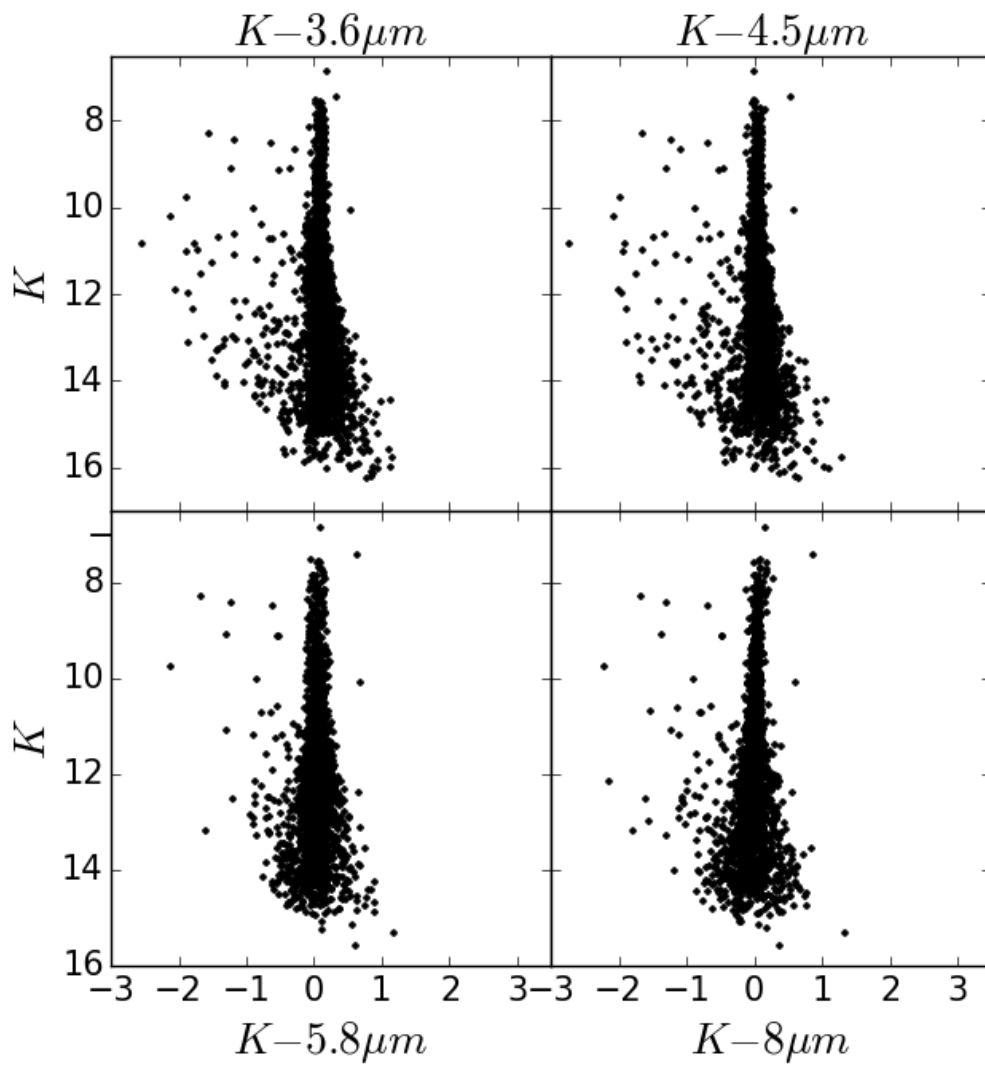


Figure 3.13: ( $K - 3.6$ ) (top-left) vs.  $K$ , ( $K - 4.5$ ) (top-right), ( $K - 5.8$ ) (bottom-left), ( $K - 8$ ) (bottom-right) CMDs for  $\omega$  Cen.

## Chapter 4

### M33 - Artificial stars test

Environments with high stellar density may cause star blending, which biases colour and magnitudes (e.g. Davidge & Puzia, 2011; Olsen et al., 1998; Rowe et al., 2005; Stephens et al., 2001), and star loss, which affects mostly faint stars (Gallart et al., 2005). Therefore, it is crucial to assess the impact of the crowding on the magnitudes and any systematic effect in the photometry, once the method to determine the SFH fits isochrones over the CMD. For instance, if the stars are shifted due to the crowding we can wrongly assume the stellar age, metallicity and mass (Tolstoy et al., 2009). Not taking into account the crowding effect, the real brightness of the stars would be overestimated, that would mean that the age estimate would be wrong, those stars would be considered younger than they really are. Also, the blending effect tend to return blue stars redder and red stars bluer (Aparicio & Gallart, 1995; Gallart et al., 1996), resulting in a mismatch of the isochrones. Incompleteness, on the other hand, would affect the star count inducing us to assume a wrong IMF (Dolphin & Hunter, 1998), hence a wrong SFH. For that reason, an artificial stars test was performed to quantify the impact of the crowding in the magnitudes. A good understanding of the crowding effects and completeness can help us to select the finest stars with most reliable photometry to conduct our analysis of the CMDs. In a nutshell, the test consists in adding fake stars, with known position and magnitude, in the real images and re-measuring the magnitude and compare the input and output quantities. In the end, it is

possible to evaluate the magnitude gradient and number of stars lost in the process.

## 4.1 Monte Carlo test

The traditional artificial stars test (AST, Stetson & Harris, 1988) consists of inserting into the images artificial stars with known positions and magnitudes. Then the photometry is run in the synthetic image using the standard data reduction used in the observed frames. When performing the AST it is important to respect the initial stellar density conditions of the frame, not adding too many stars at time, so the true completeness can be reproduced and the result be a valid estimation.

As one expects the crowding and completeness effect to be functions of magnitude, the magnitudes were randomly distributed similarly to those found in our observed images, sampling the luminosity function of each sub-image (which is a trimmed image from the galaxy master-image, with size of 2048 vs 2048 pixels<sup>2</sup>) for each filter. The positions were randomly created but respecting a distance of 10 pixels between two points to avoid self-crowding. Colours were not attributed for the fake stars, as the photometric errors and the completeness are almost entirely functions only of the magnitude. ADDSTAR (Stetson, 1987) is a Monte Carlo method that inserts in the raw images the fictitious stars and creates a synthetic frame with the new stars. To construct the artificial stars as realistically as the observed stars in the images, the same PSF star lists (the ones used to perform the photometry of the real stars) and the same PSF were used in the AST.

After all fake stars had been inserted in all sub-images, the PSF-fitting reduction was performed as described in section 3.1.1. In each filter, a total of  $4.8 \times 10^6$  stars was added in order to minimize statistical uncertainties; 40 stars were added in an individual sub-image at a time, to not excessively increase the stellar density in that particular sub-image. Every single sub-image had repeatedly added 40 stars and remeasured their magnitudes on one thousand iterations. This is a very time consuming task. To compare the magnitudes of the inserted stars to the retrieved ones, the axial coordinates

of the stars were matched considering a matching radius of 1 pixel. The completeness was computed as the ratio of the number of recovered stars over the number of inserted artificial stars.

Figure 4.1 presents the completeness, magnitude and position bias as a function of magnitude for a subregion in  $r'$  filter. The fraction of recovered stars over the input accounts only for the brightness regardless of the position, which means that a star could be in a magnitude bin in the input but recovered in another, usually brighter.

## 4.2 AST results

The completeness was calculated in bins of 0.5 dex. To determine the ratio where 50% of the stars were recovered, the last ratio above ( $rat_a$ ) and the first ratio below ( $rat_b$ ) 0.5 was stored, as 0.5 will be somewhere between them. Therefore, there are two regimes to determine the magnitude at 50% ( $mag_{50}$ ) recovery. If  $mag_a$  is nearer to 0.5, so is  $mag_{50}$ , then:

$$mag_{50} = mag_a + \frac{binwidth}{2} \times \frac{|0.5 - rat_a|}{0.5} \quad (4.1)$$

For the opposite situation, where  $mag_b$  is nearer, one can say:

$$mag_{50} = mag_b - \frac{binwidth}{2} \times \frac{|0.5 - rat_b|}{0.5} \quad (4.2)$$

The error (e) bars are equivalent to the bin width, 0.5 dex. However, they were weighted according to the position of  $mag_{50}$  between  $mag_a$  and  $mag_b$ , which means that  $e_{min} = mag_{50} - mag_a$  and  $e_{max} = mag_b - mag_{50}$ . Figure 4.2 shows the completeness curves of 6 different areas of the galaxy. The left column locates crowded area and the right column an uncrowded area.

These regions are the same in the filters  $g'$  (on top),  $r'$  (in the middle) and  $i'$  (at the bottom). The recovery ratio becomes brighter towards the centre of the galaxy due to extreme stellar crowding in there. The difference of magnitude ( $\Delta mag$ ) of

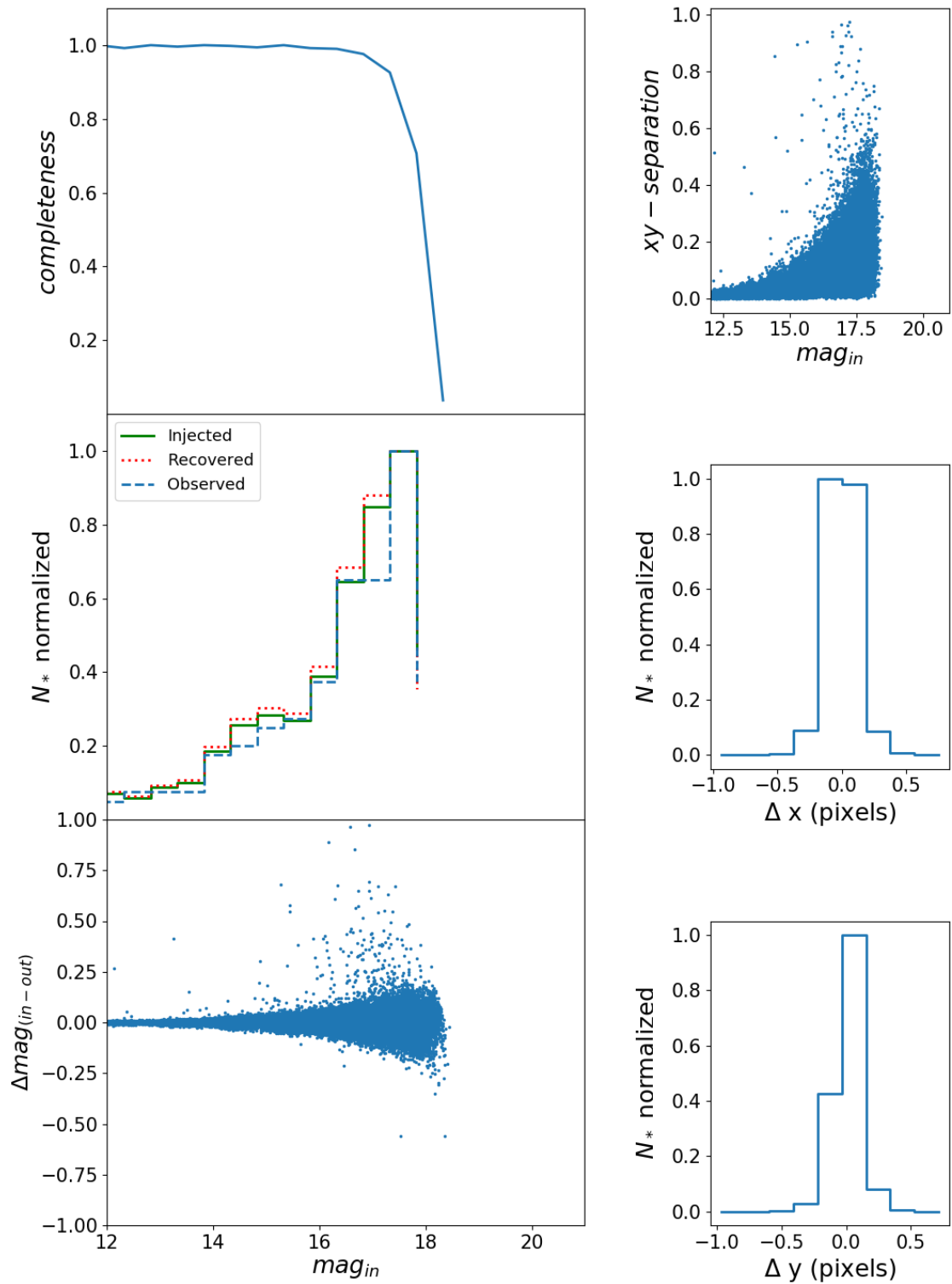


Figure 4.1: Top-left: plot of the ratio between the recovered and the injected artificial stars; Middle-left: comparison of the observed, injected and recovered stars; Bottom-left: blue dots are the magnitude difference; Top-right: the dispersion in position (x and y); Middle- and Bottom-right: histograms of the dispersion in x and y respectively.

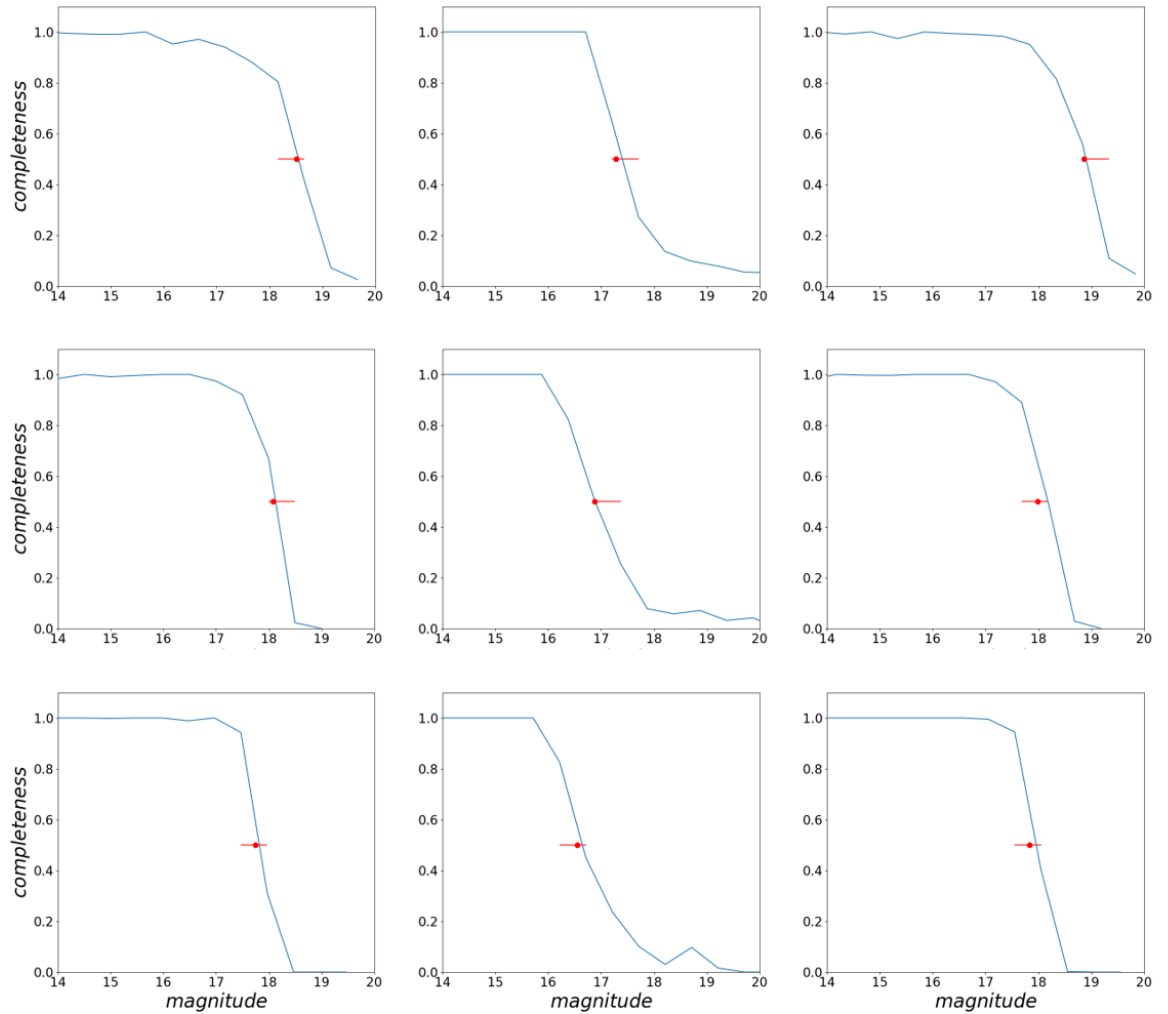


Figure 4.2: Completeness (the ratio of the number of recovered stars over the number of inserted artificial stars) by instrumental magnitude. Red dot is the magnitude where 50% of stars were recovered and the total length of the error bar is 0.5 dex (equivalent to the bin-width at which the ratio was calculated). Multiple columns are located in the outskirts of the galaxy and opposite to each other whilst the middle column is in the centre of the galaxy. Top row is  $g'$  filter, middle row is  $r'$  filter and bottom is  $i'$  filter.

each sub-image were fitted by two functions: an exponential function of the form  $f(x) = ae^{(x/b)} + c$ , and a polynomial function of the form  $ax^4 + bx^3 + cx^2 + dx + e$ . The distributions were binned in 0.1 dex, then some cutting parameters were applied according to standard deviation in colour and star count inside the bins to improve the fitting and, after that each bin was averaged. Therefore, the functions fit the averages. The best fit was decided according to  $\chi^2 = \sum (\overline{\text{observed}} - \text{expected})^2$  where  $\overline{\text{observed}}$  is the mean value of the bins and  $\text{expected}$  is the fitted value in the bins. Most of the sub-images were better fitted by the exponential function, whilst only about 12% of the images were better fitted by the polynomial function. There is no correlation between the fitted functions and the stellar density or magnitude. One can see in figures 4.3, 4.4 and 4.5, the magnitude distribution of the difference between the added and retrieved stars, plots from crowded and uncrowded areas, representing the same region in the filters g', r' and i'. Each plot presents also solid red lines that are the average and  $1\sigma$  deviation, dash-dot magenta line is the exponential fitting and dashed yellow line is the polynomial fitting.

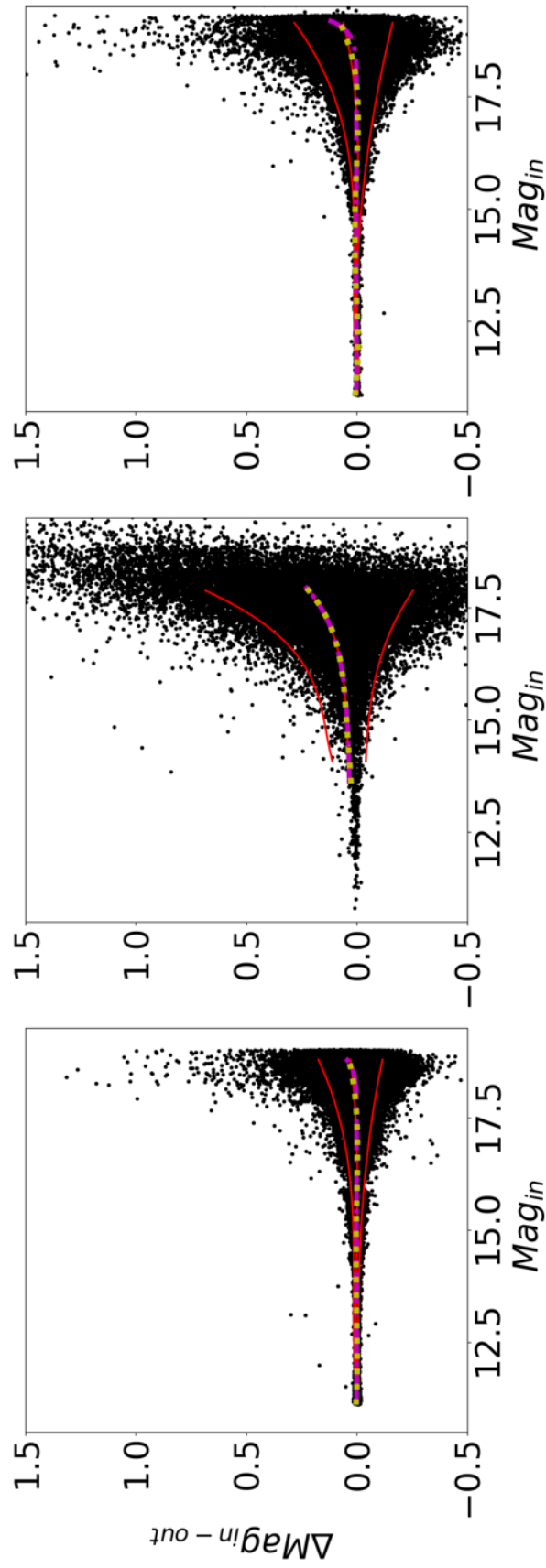
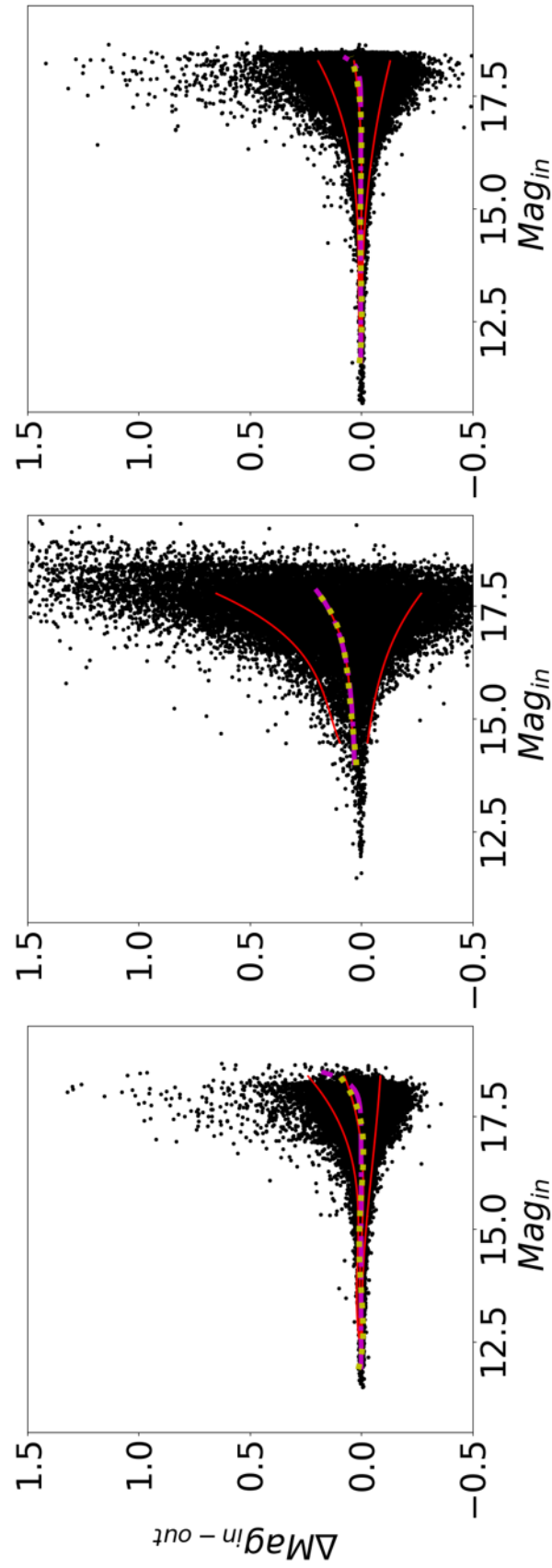


Figure 4.3: The distribution of the difference of magnitude  $\Delta\text{mag}$  with the exponential (magenta) and polynomial (yellow) functions fitted on it for  $g'$  filter. Red lines are the average and  $\pm 1\sigma$ . Left and right plots are located in the outskirts of the galaxy and opposite to each other whilst the middle plot is in the centre of the galaxy.

Figure 4.4: Same as figure 4.3, but for  $r'$  filter.

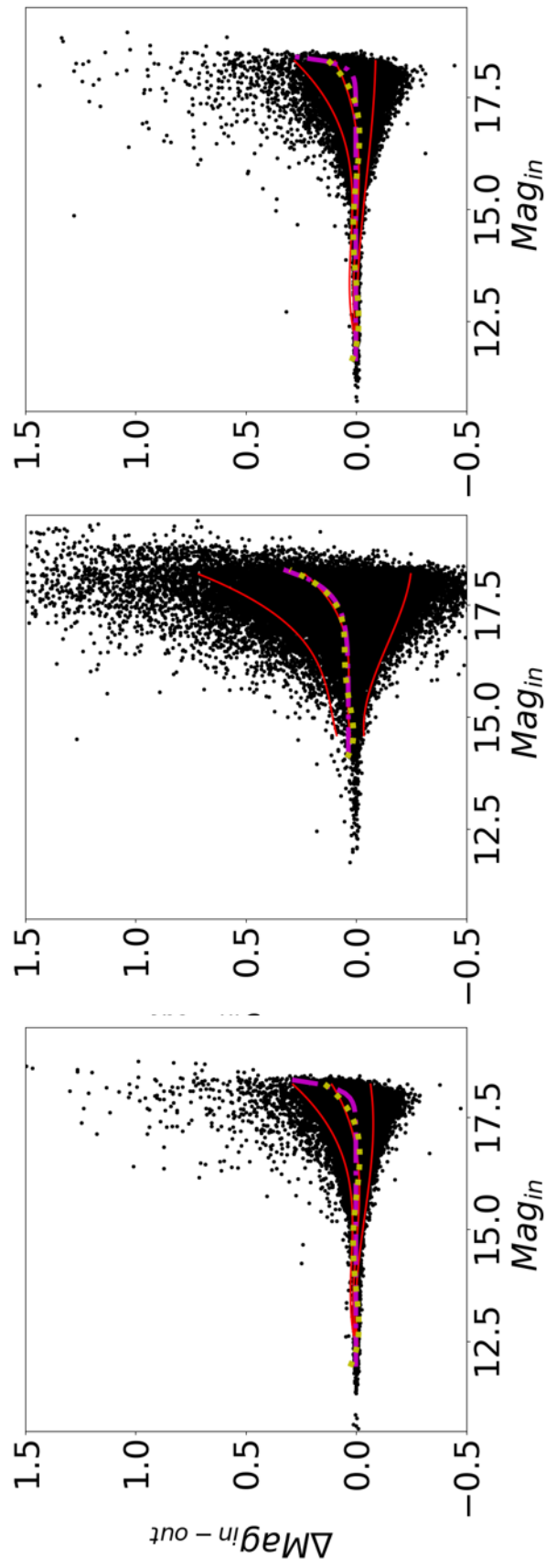


Figure 4.5: Same as figure 4.3, but for i' filter.

The stellar density in an image was calculated according to

$$\frac{N_* \times PSF^2 \pi}{N_x \times N_y} \quad (4.3)$$

where  $N_*$  is the total number of stars in the image, PSF is the FWHM in pixels units and  $N_x$  and  $N_y$  are the number of pixels in x and y coordinates, respectively. The FWHM was added to the equation with the purpose of considering the crowding in the PSF cells, divided by the sub-image area. Figure 4.6 shows how the parameter b (responsible for the slower or faster function growth) from the exponential function increases with increasing stellar density. Figure 4.7 shows that the magnitude at 50% recovery also depends on stellar density. Figures 4.8, 4.9 and 4.10 display a colour map for the filters g', r' and i', respectively, based on the stellar densities calculated for each sub-image. The numbers printed inside each region is the magnitude where 50% of stars were recovered, x and y are spatial coordinates in pixels. For the thorough list of AST result see table A.4.

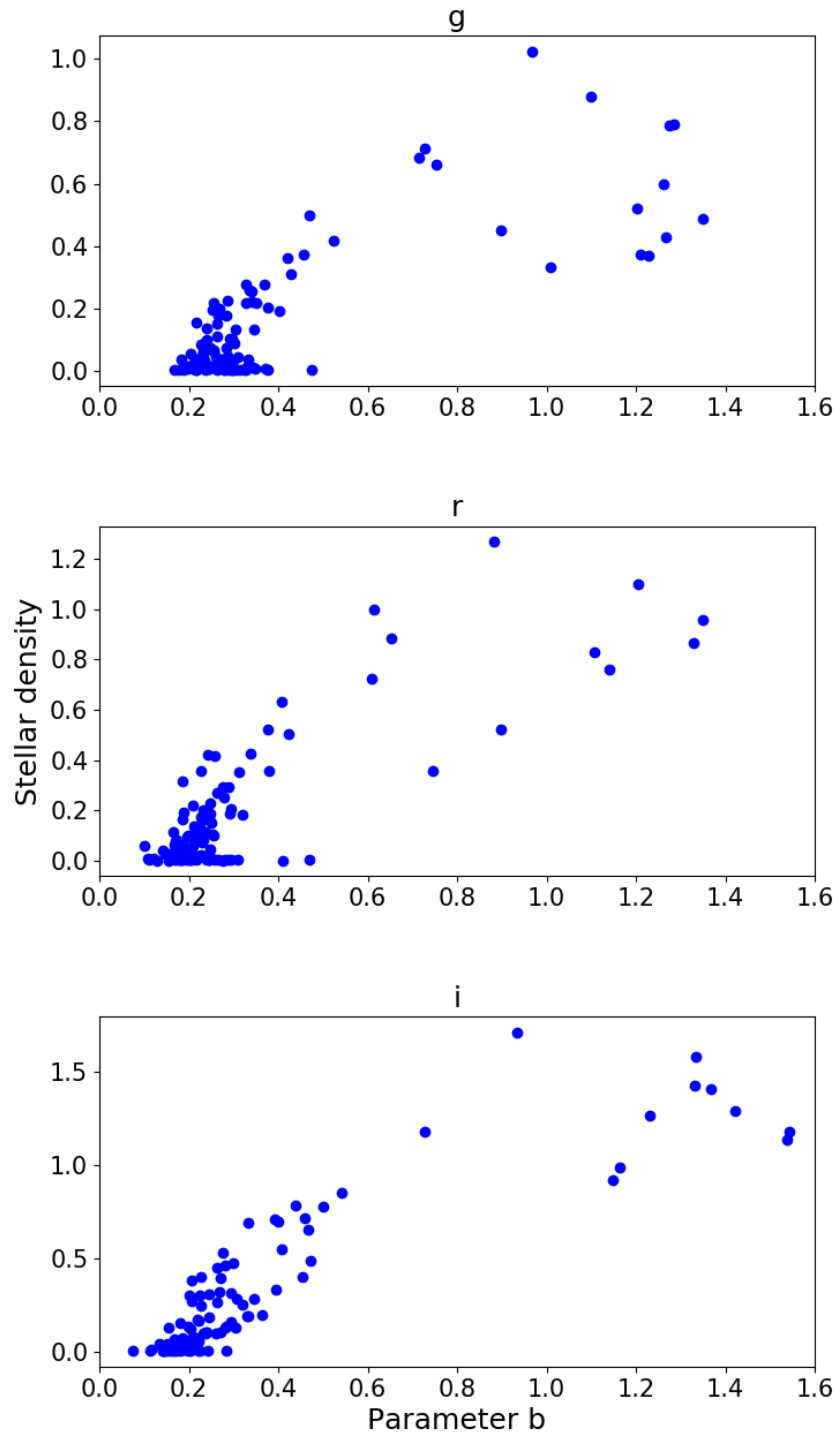


Figure 4.6: Parameter  $b$ , from the exponential function  $f(x) = ae^{(x/b)} + c$ , versus stellar density. Top plot is result for  $g'$  filter, middle plot refers to  $r'$  filter and bottom plot is  $i'$  filter.

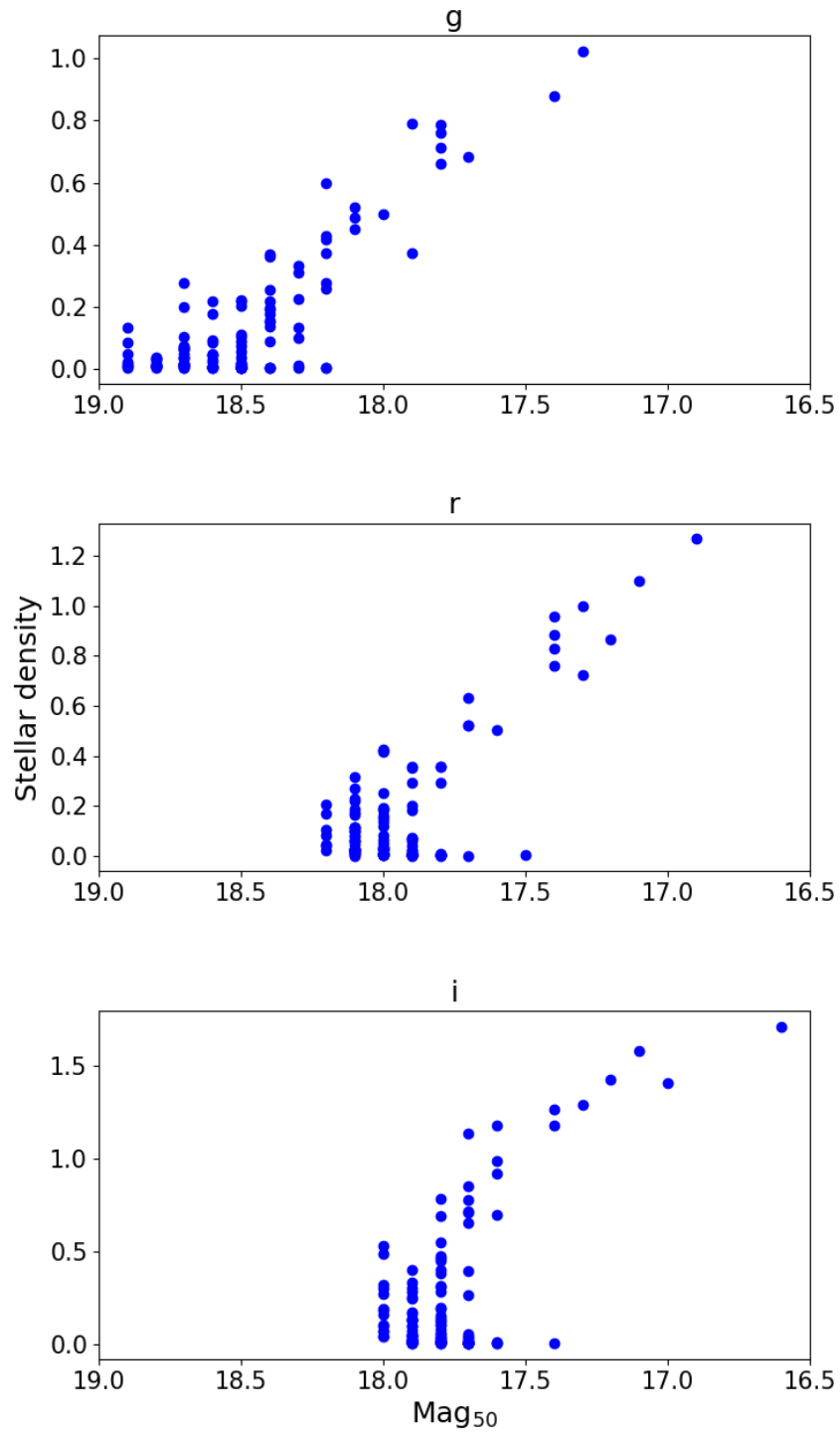


Figure 4.7: Magnitude at 50% recovery rate versus stellar density. Top plot is result for  $g'$  filter, middle plot is referent to  $r'$  filter and bottom plot is  $i'$  filter.

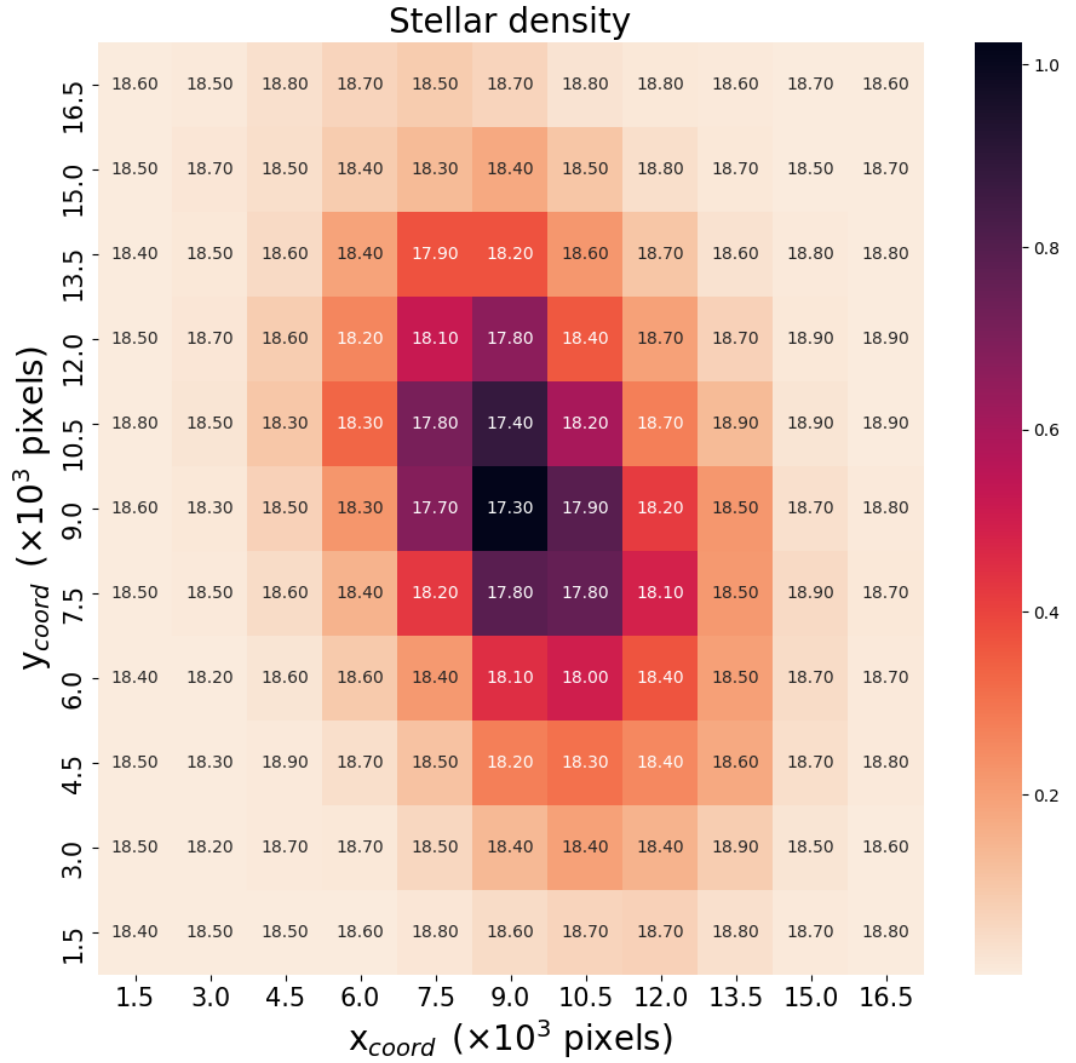
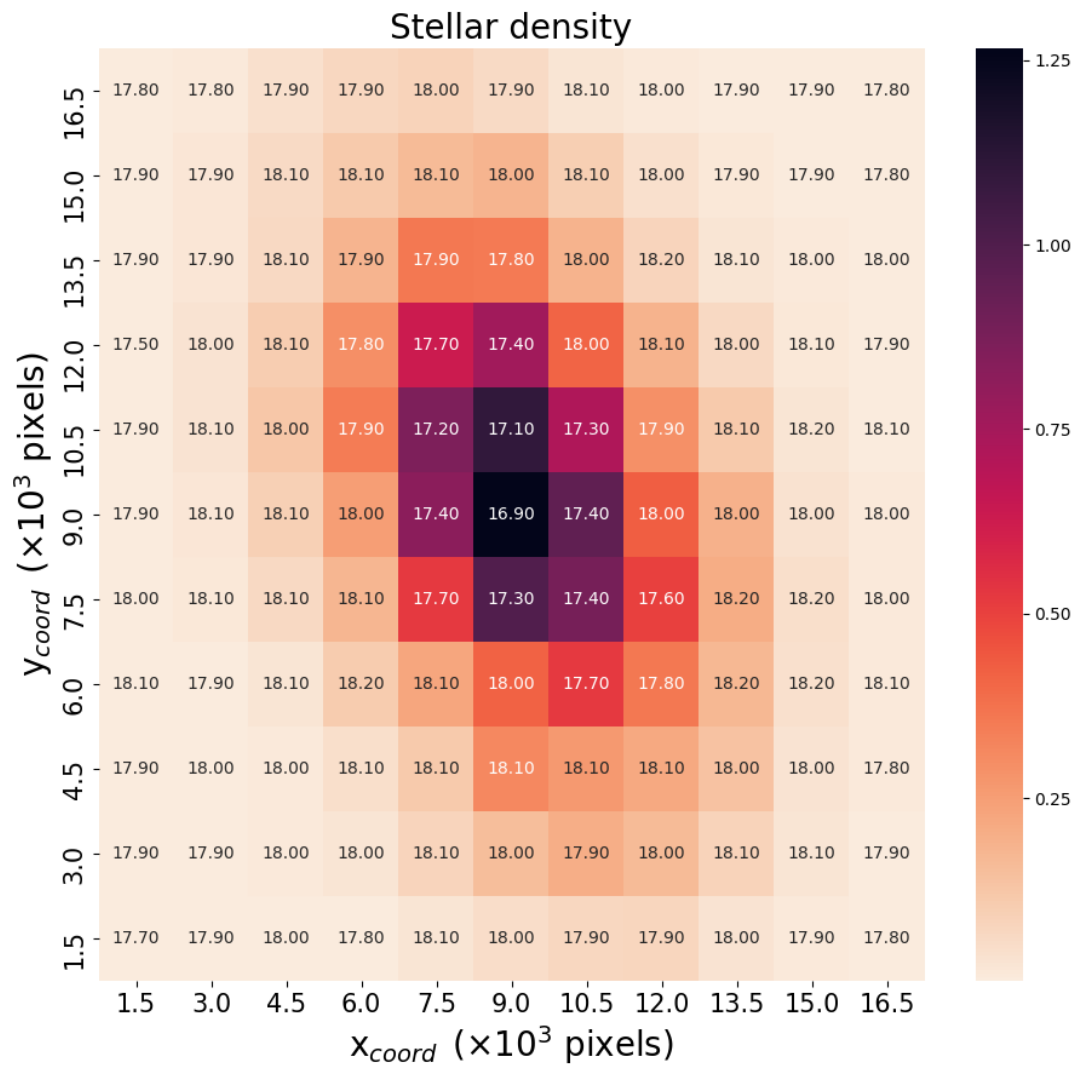
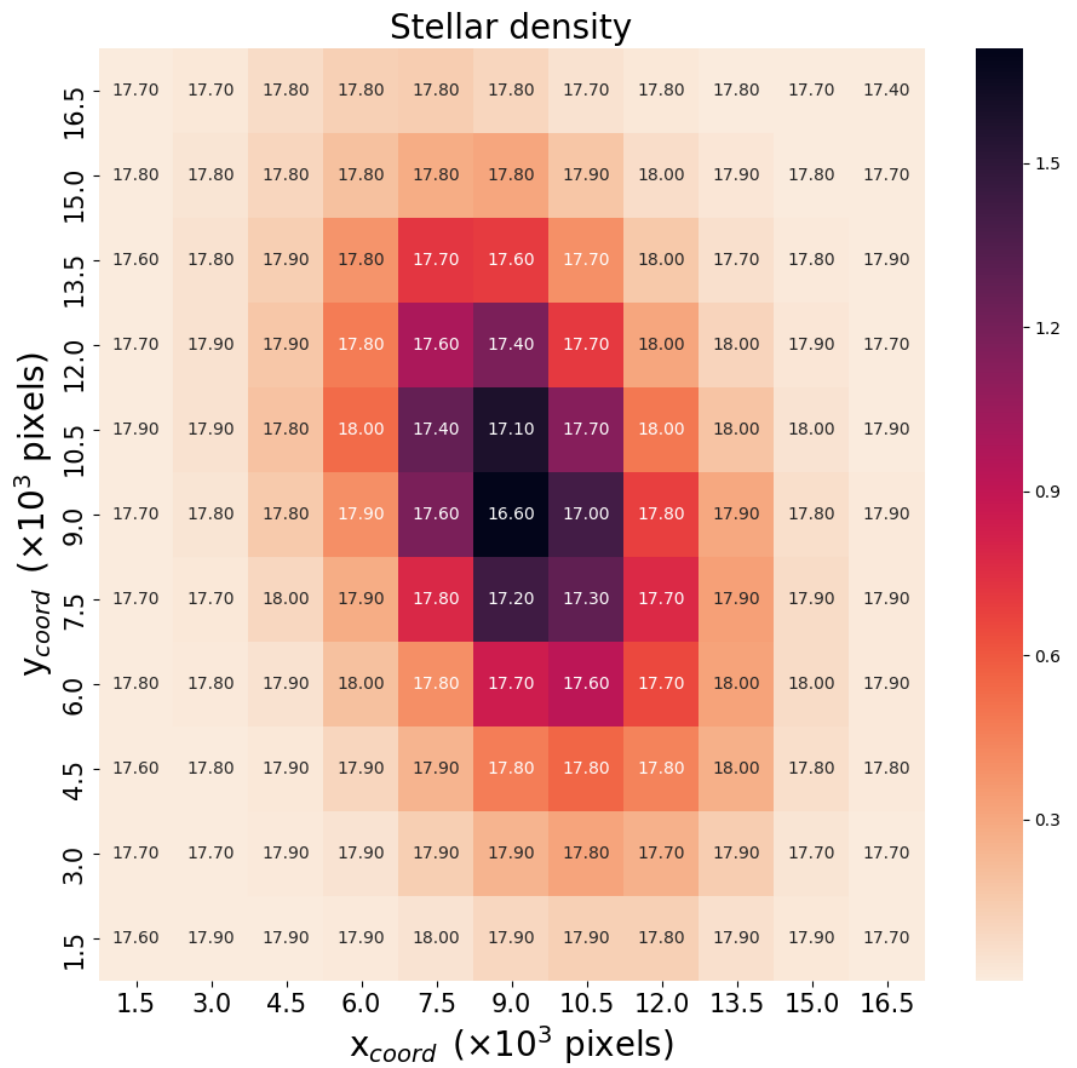


Figure 4.8: Stellar density  $\left(\frac{N_* \times PSF^2 \pi}{N_x \times N_y}\right)$  for the sub-images of the g' filter. The axes are the spatial position xy in pixels and the number written inside each square is the instrumental magnitude at which 50% of the stars were recovered.

Figure 4.9: Same as figure 4.8, but for the  $r'$  filter.

Figure 4.10: Same as figure 4.8, but for the  $i'$  filter.

# Chapter 5

## Mass-loss in $\omega$ Cen

This chapter describes, firstly, how all photometric magnitudes derived in the chapter 3 were converted from the SDSS photometric system to the TCS system. Effective temperatures and bolometric corrections are needed to the comparison between theory and observations and were derived for all stars based on the empirical colour-temperature relation from Alonso et al. (1999). Then, mass-losing candidate stars were selected according to the  $(K - 8)$  colour excess. The evolutionary stage of the mass-losing stars was identified after a visual inspection of the CMD, for the RGB and AGB stars, and LPV stars were identified after a cross-correlation with some LPV catalogues. Metallicity was attributed to the stars after isochrone interpolation. Field stars were removed from our sample based on GAIA proper motions. Ultimately, the ML rates are derived for those RGB stars for the GC  $\omega$  Cen in a modified version of the radiative transfer code DUSTY.

### 5.1 Physical parameters

One of the physical parameters needed to generate the spectral energy distributions used in the radiative transfer code is the effective temperature ( $T_{\text{eff}}$ ) of the stars. The colour-temperature equations used to calculate the  $T_{\text{eff}}$  were derived based on magnitudes and colours from a photometric system different of the ones reduced in this

work. The transmission profiles and effective wavelengths for each photometric system are different from each other. These variations causes a mismatch in the observed magnitudes and colours when two photometric systems are compared. A precise comparison between observations made in different telescopes requires that those datasets are converted to the same photometric system. Which is why the  $K$  magnitudes, that are in the 2MASS photometric system, were transformed to the Telescopio Carlos Sanches (TCS) photometric system, which is the standard photometric system used in the colour-temperature equations by Alonso et al. (1999). Firstly, the  $K_{2MASS}$  were transformed into the Caltech (CIT) system according to the transformation equations provided by Carpenter (2001), as shown below:

$$(J - K)_{2MASS} = (1.056 \pm 0.006)(J - K)_{CIT} + (-0.013 \pm 0.005) \quad (5.1)$$

and

$$(K)_{2MASS} = K_{CIT} + (0.000 \pm 0.005)(J - K)_{CIT} + (-0.024 \pm 0.003) \quad (5.2)$$

Then, the  $K_{CIT}$  was converted into the  $K_{TCS}$  following the transformation equations present in Alonso et al. (1998), see below:

$$J_{TCS} = J_{CIT} - 0.035 + 0.019(J - K)_{CIT} \quad (5.3)$$

and

$$K_{TCS} = K_{CIT} - 0.022 + 0.006(J - K)_{CIT} \quad (5.4)$$

Once the apparent magnitudes were in the same photometric system as in Alonso et al. (1999), the absolute magnitudes, which are the intrinsic brightness of the stars in a given wavelength range, were determined. The distance modulus used to determine the absolute magnitudes is  $(m - M)_V = 14.04$  and a reddening of  $E(B - V) = 0.11$  (Bellazzini et al., 2004) was assumed.  $T_{\text{eff}}$  was obtained through the empirical  $(V - K)$

Table 5.1: Coefficients from the colour-temperature relation of Alonso et al. (1999).

<i>coef</i>	$(V - K)_{1.2}^{2.0}$	$(V - K)_{2.0}^{3.4}$
$a_0$	0.555800	0.377000
$a_1$	0.210500	0.366000
$a_2$	$1.981 \times 10^{-3}$	$-3.170 \times 10^{-2}$
$a_3$	$-9.965 \times 10^{-3}$	$-3.074 \times 10^{-3}$
$a_4$	$1.325 \times 10^{-2}$	$-2.765 \times 10^{-3}$
$a_5$	$-2.726 \times 10^{-3}$	$-2.973 \times 10^{-3}$

colour-temperature relation using the calibrations by Alonso et al. (1999, 2001):

$$\theta_{eff} = a_0 + a_1X + a_2X^2 + a_3X[Fe/H] + a_4[Fe/H] + a_5[Fe/H]^2 \quad (5.5)$$

where  $\theta_{eff} = 5040/T_{eff}$ ,  $X$  represents the colour term  $(V - K)$ , the coefficients  $a_*$  are specified in table 5.1 and it was assumed a  $[Fe/H] = -1.7$  (Bellazzini et al., 2004), which is the metallicity main peak for  $\omega$  Cen in its wide metallicity distribution.

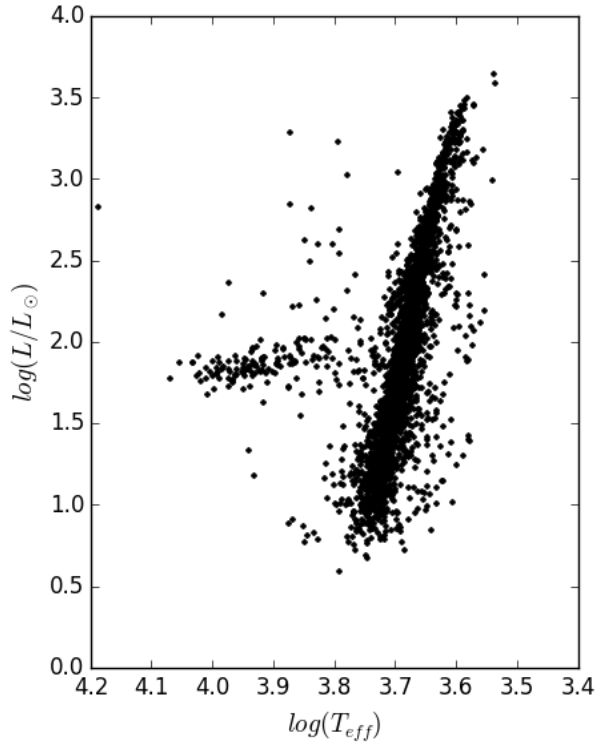
The colour-temperature relation is applicable depending on certain colour and metallicity ranges. Since the metallicity is assumed to be  $[Fe/H] = -1.7$ , the colour ranges should be between 1.2 and 2.0, for the colour  $(V-K)_{1.2}^{2.0}$  and to satisfy  $(V-K)_{2.0}^{3.4}$  the colour range should be between 2.0 and 3.4. The bolometric magnitude  $M_{bol}$  was derived from the bolometric corrections (BC)- $T_{eff}$  relation presented by Alonso et al. (1999):

$$BC_V = \frac{-5.531 \times 10^{-2}}{X} - 0.6177 + 4.420X - 2.669X^2 + 0.6943X[Fe/H] - 0.1071[Fe/H] - 8.612 \times 10^{-3}[Fe/H]^2 \quad (5.6)$$

if  $3.58 \leq \log(T_{eff}) \leq 3.65$  for metallicity  $[Fe/H] = -1.7$  or,

$$BC_V = \frac{-9.930 \times 10^{-2}}{X} + 2.887 \times 10^{-2} + 2.275X - 4.425X^2 + 0.3505X[Fe/H] - 5.558 \times 10^{-2}[Fe/H] - 5.375 \times 10^{-3}[Fe/H]^2 \quad (5.7)$$

if  $3.65 \leq \log(T_{eff}) \leq 3.80$  for metallicity  $[Fe/H] = -1.7$ . For both situations  $X = \log(T_{eff}) - 3.52$ .

Figure 5.1: Hertzsprung-Russel Diagram for  $\omega$  Cen.

## 5.2 Colour excess selection

The spectral range from 3 to 5  $\mu m$  is dominated by photospheric emission in cool and luminous giant stars, and it has also contribution of the circumstellar dust emission. In fact, for relatively warm and low luminosity giants, such as low-mass RGB stars, the fraction of warm and optically-thin dust emission from a circumstellar envelope that contributes in the 3-5  $\mu m$  spectral range is significant. For that, the near- and mid-IR colours like  $(K - 5.8)$  and  $(K - 8)$  are more effective in detecting the presence of small amounts of warm dust around low-mass RGB (Origlia et al., 2010), whilst the use of only *Spitzer*-IRAC colours, for instance (3.6 - 8), is mostly sensitive to tracing larger amounts of cold dust around cooler and more luminous giants. With all that in mind, the use of the  $(K - 8)$  colour as the first method to select stars with a possible dust excess seems to be reasonable.

Firstly, a CMD  $(K - 8)$  vs.  $M_{bol}$  is constructed as shown in figure 5.2. The mean ridge

line was established and the standard deviation of the colour was calculated in different magnitude bins for the stars in the blue side of the line, because those stars are certain to have only photospheric emission. Stars in the red side of the line were then flagged as dusty when they presented a colour excess  $\geq +2.0\sigma$  from the mean ridge line.

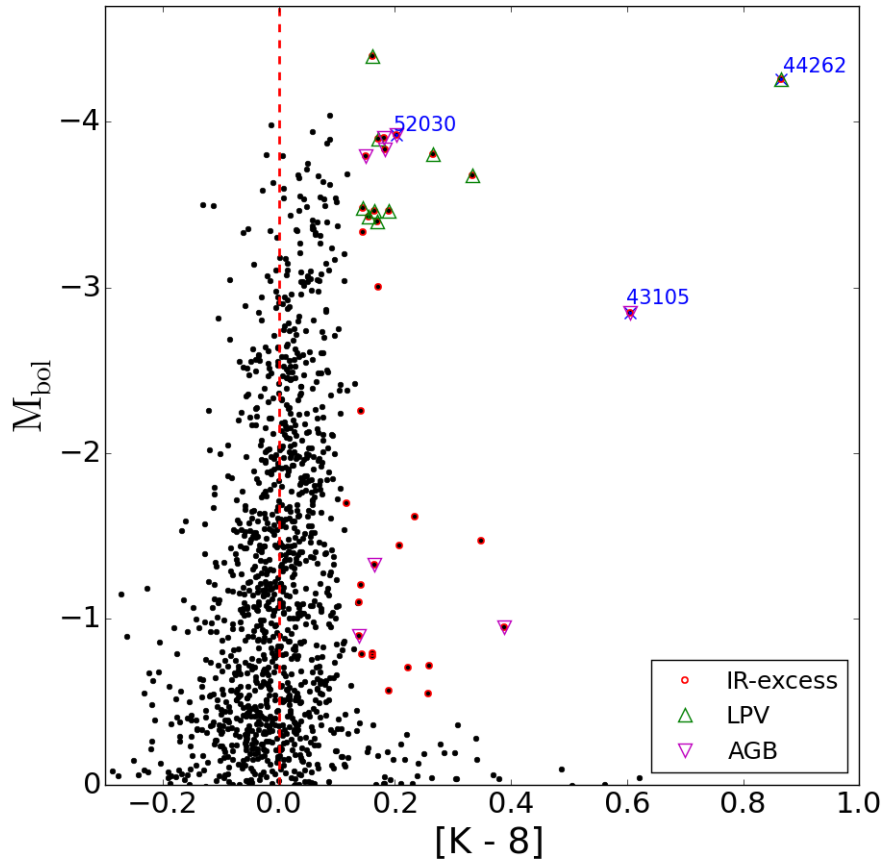


Figure 5.2:  $(K - 8)$  colour vs.  $M_{\text{bol}}$  CMD for  $\omega$  Cen. Stars with IR colour excess are marked with red circles, green squares are ML candidate stars from Boyer et al. (2008). 44262 (V42), 52030 and 43105 (V29) are stars identified also by Woolley (1966); Clement (1997); van Leeuwen et al. (2000); Kaluzny et al. (2004); McDonald et al. (2011).

The  $(K - 5.8)$  vs.  $(K - 8)$  colour-colour diagram is used to confirm the selection of the dust excess candidates, as those stars are expected to be redder in other IRAC bands. Figure 5.3 shows the colour-colour diagram for  $\omega$  Cen, note that the final 34 giants with dust excess are marked with red circles.

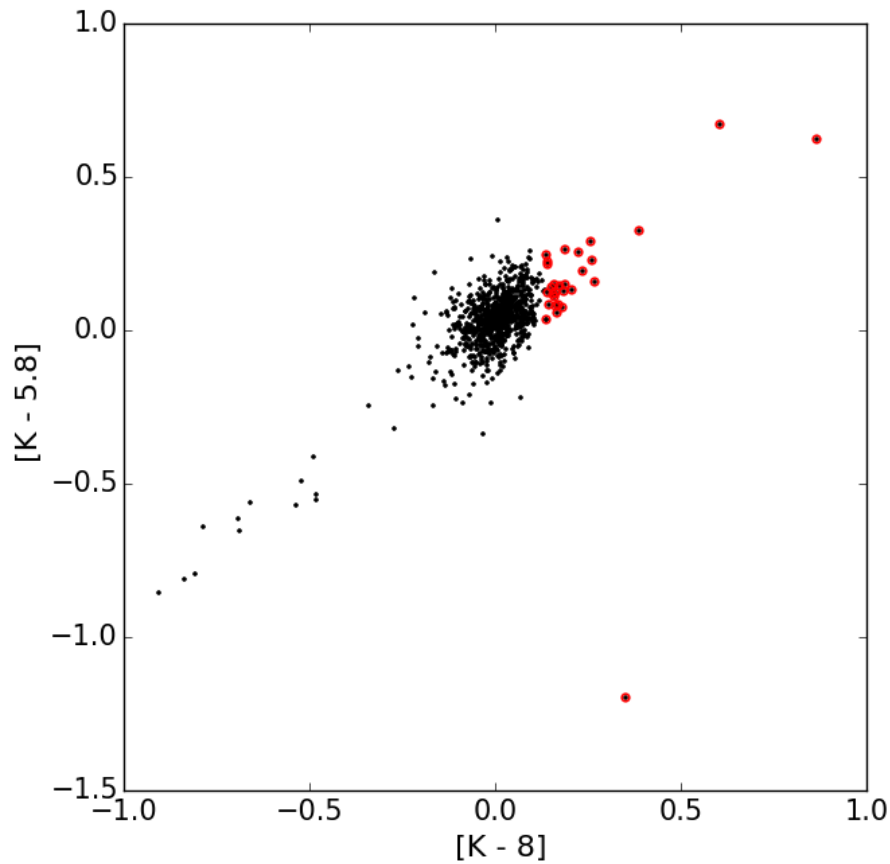


Figure 5.3:  $(K - 5.8)$  vs.  $(K - 8)$  colour-colour diagram for  $\omega$  Cen. Stars with IR colour excess are marked with red circles.

### 5.3 Dust excess sample

A visual inspection, examining the position of the stars, in optical ((B - I), B and (B - V), V) CMDs allowed us to classify RGB and AGB stars. AGB stars were considered to be those stars in a well-defined sequence falling close to a parallel track in the bluest part of the main body of the RGB. Stars brighter than the tip of RGB,  $M_K = -6.04 \pm 0.16$  (Bellazzini et al., 2004), were also considered to be AGB stars. LPV stars were classified from the van Leeuwen et al. (2000), Lebzelter & Wood (2016), and Mowlavi et al. (2018) catalogues. The total count of AGB stars in our sample is 191. Figure 5.4 shows in red our AGB selection and in blue the LPV present in our field of view.

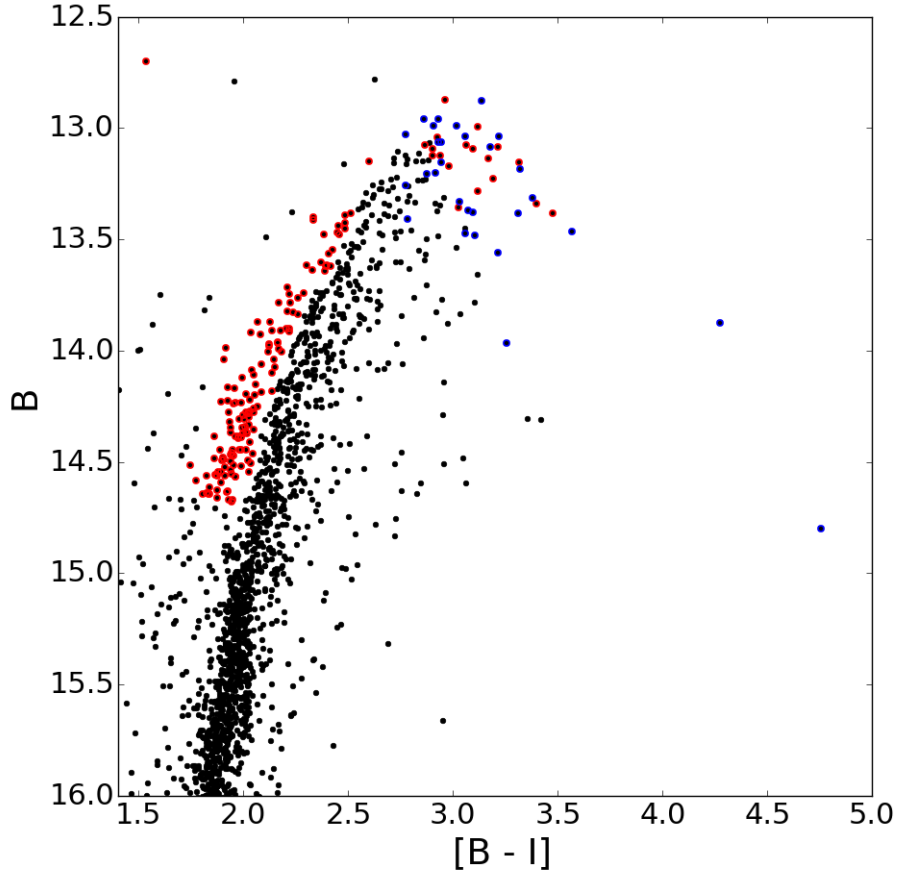


Figure 5.4: (B - I) colour vs. B for stars in  $\omega$  Cen. Optical CMD used to select AGB stars (red circles). Blue circles are LPV stars from van Leeuwen et al. (2000); Lebzelter & Wood (2016); Mowlavi et al. (2018).

To determine the metallicities of the mass-losing candidates, a collection of isochrones were taken into account. The isochrone interpolation involves to estimate the distance from the  $T_{\text{eff}}$  and luminosity of the star to each isochrone. The metallicity of the closest isochrone to the  $T_{\text{eff}}$  and luminosity of a given star is attributed as the metallicity of that particular star. PARSEC (Bressan et al., 2012) isochrones are used for the interpolation with the age of 10 Gyr. Figure 5.5 shows isochrones of metallicities  $[\text{Fe}/\text{H}] = -0.7, -1.0, -1.3, -1.6$  and  $-1.9$  plotted in the (V - K) colour vs. V CMD.

A total of 34 stars was identified with IR colour excess within  $2.0\sigma$ . 12 stars of those stars in our sample were also identified as mass-losing candidates by Boyer et al. (2008). The reddest star is LEID 44262 with  $[\text{Fe}/\text{H}] = -0.7$  (whilst optical spec-

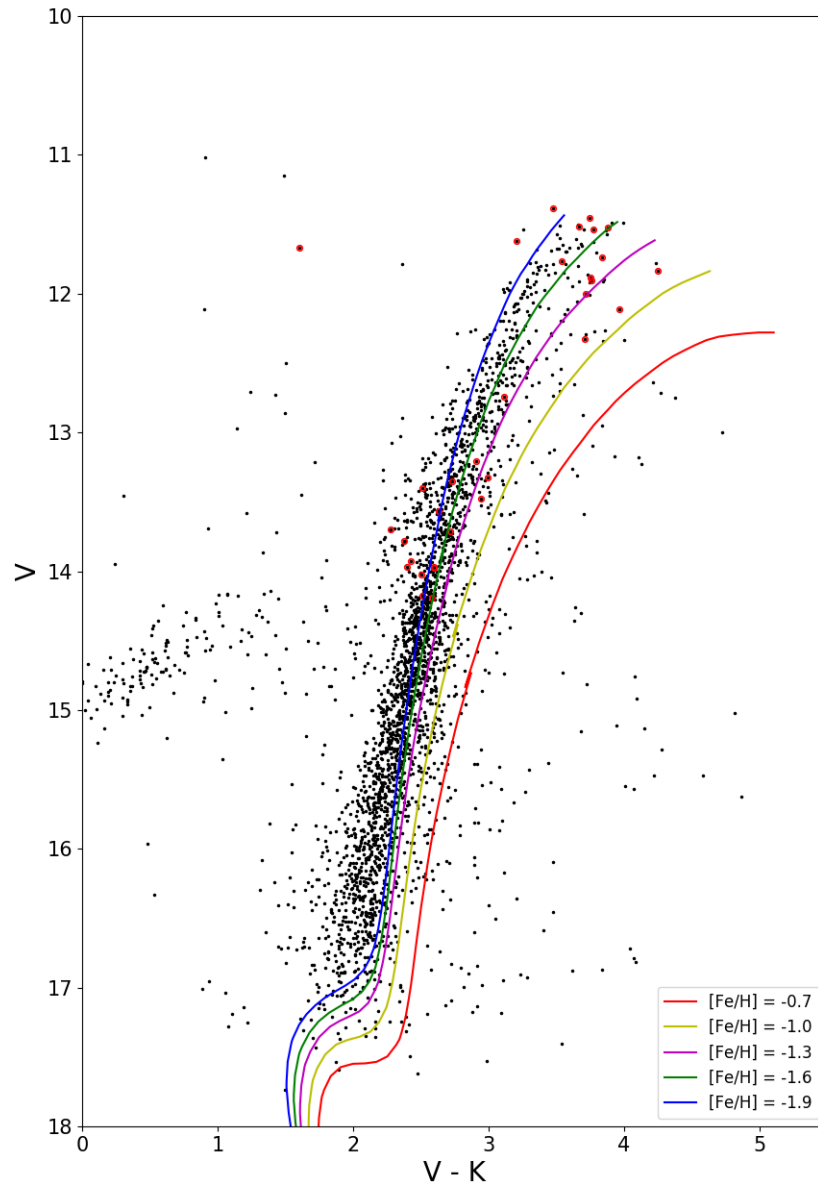


Figure 5.5: PARSEC (Bressan et al., 2012) theoretical isochrones, assuming  $[\text{Fe}/\text{H}] = -0.7, -1.0, -1.3, -1.6$  and  $-1.9$  and age 10 Gyr.

troscopy measurements is  $[\text{Fe}/\text{H}] = -1.25$  by van Loon et al. (2008)) and it is also the coolest (3452 K). Boyer et al. (2008) found  $[\text{Fe}/\text{H}] = -1.5$  for their reddest star. Stars with possible ML in our sample cover a range of 1.2 dex in metallicity, according to the metallicities interpolated from theoretical isochrones as shown in figure 5.5. The brightest stars (LEID 44420, 44262, 45232, 48060, 48150, 49123, 52030) show metallicity ranging from  $-1.9 < [\text{Fe}/\text{H}] < -0.7$ , while Boyer et al. (2008)'s sample ranges from  $-2.25 < [\text{Fe}/\text{H}] < -1.25$ . Table 5.2 presents the dusty stars and their IRAC fluxes, the derived  $T_{\text{eff}}$  and luminosity ( $\log(\frac{L}{L_{\odot}})$ ), the metallicity ( $[\text{Fe}/\text{H}]$ ) interpolated from theoretical isochrones and the evolutionary stage of the stars.

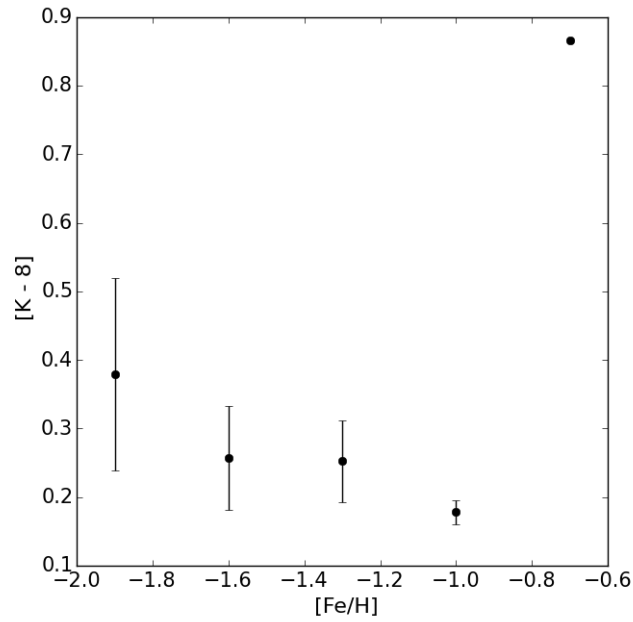


Figure 5.6:  $(K - 8)$  colour vs.  $[\text{Fe}/\text{H}]$  for the dusty stars in  $\omega$  Cen. The colour is an average of all stars with that particular metallicity. Metallicities were interpolated from theoretical isochrones. Stars with low metallicity does not seem to restrict dust production.

Table 5.2: Stars with IR-excess.

R.A.	DEC.	$3\mu\text{m}$	$4.5\mu\text{m}$	$5.8\mu\text{m}$	$8\mu\text{m}$	$T_{\text{eff}}(\text{K})$	$\log(\frac{L}{L_{\odot}})$	$[\text{Fe}/\text{H}]$	Type
<sup>1</sup> <b>201.69308</b>	<b>-47.49171</b>	<b>7.10</b>	<b>6.89</b>	<b>6.80</b>	<b>6.55</b>	<b>3452</b>	<b>3.59</b>	<b>-0.7</b>	<b>LPV<sup>2</sup></b>
<b>201.77199</b>	<b>-47.48466</b>	<b>6.65</b>	<b>6.84</b>	<b>6.75</b>	<b>6.67</b>	<b>3460</b>	<b>3.65</b>	<b>-1.0</b>	<b>LPV<sup>23</sup></b>

Continue on next page...

<sup>1</sup>**Notes:** Stars marked in bold are cluster members stars based on GAIA proper motions.

<sup>2</sup>Lebzelter & Wood (2016)

<sup>3</sup>Mowlavi et al. (2018)

Table 5.2 – Continued from previous page

R.A.	DEC.	$3\mu m$	$4.5\mu m$	$5.8\mu m$	$8\mu m$	$T_{\text{eff}}(\text{K})$	$\log(\frac{L}{L_{\odot}})$	$[Fe/H]$	Type
201.49471	-47.60263	–	8.07	–	7.97	3837	3.25	-1.0	LPV <sup>4</sup>
201.81588	-47.46506	–	7.77	–	7.57	3892	3.36	-1.3	LPV <sup>4</sup>
201.65332	-47.51379	7.99	8.04	7.99	7.95	3925	3.27	-1.3	LPV <sup>4</sup>
201.53178	-47.54827	–	8.00	–	7.98	3929	3.28	-1.3	LPV <sup>2</sup>
<b>201.72909</b>	<b>-47.47941</b>	<b>8.07</b>	<b>8.13</b>	<b>8.10</b>	<b>8.06</b>	<b>4033</b>	<b>3.27</b>	<b>-1.6</b>	<b>LPV<sup>2</sup></b>
201.68166	-47.49388	7.58	7.57	7.63	7.54	3932	3.45	-1.6	LPV <sup>2</sup>
201.64748	-47.53004	7.84	7.82	7.75	7.64	4068	3.41	-1.9	LPV <sup>2</sup>
201.65008	-47.44829	8.27	8.32	8.30	8.26	4229	3.26	-1.9	LPV <sup>2</sup>
201.66591	-47.51851	7.47	7.58	7.51	7.40	3735	3.45	-1.3	AGB
201.78760	-47.39388	7.73	7.77	7.70	7.69	3968	3.40	-1.6	AGB
201.56731	-47.51548	7.63	7.64	7.64	7.58	3920	3.42	-1.6	AGB
201.50664	-47.55156	–	7.51	–	7.44	3874	3.46	-1.6	AGB
<b>201.61340</b>	<b>-47.47976</b>	<b>9.52</b>	<b>9.49</b>	<b>9.39</b>	<b>9.46</b>	<b>6034</b>	<b>3.03</b>	<b>-1.9</b>	<b>post-AGB</b>
<b>201.63629</b>	<b>-47.51306</b>	<b>11.20</b>	<b>11.18</b>	<b>11.10</b>	<b>11.03</b>	<b>5079</b>	<b>2.27</b>	<b>-1.9</b>	<b>AGB</b>
<b>201.68593</b>	<b>-47.49855</b>	<b>10.80</b>	<b>10.73</b>	<b>10.83</b>	<b>10.72</b>	<b>4807</b>	<b>2.42</b>	<b>-1.9</b>	<b>AGB</b>
<b>201.72547</b>	<b>-47.48193</b>	<b>11.21</b>	<b>11.19</b>	<b>11.16</b>	<b>11.27</b>	<b>4955</b>	<b>2.25</b>	<b>-1.9</b>	<b>AGB</b>
201.71746	-47.43528	8.46	8.54	8.47	8.44	3948	3.09	-1.0	RGB
<b>201.66025</b>	<b>-47.48216</b>	<b>10.42</b>	<b>10.42</b>	<b>10.40</b>	<b>10.32</b>	<b>4415</b>	<b>2.47</b>	<b>-1.0</b>	<b>RGB</b>
<b>201.69620</b>	<b>-47.49370</b>	<b>10.14</b>	<b>10.23</b>	<b>10.14</b>	<b>10.10</b>	<b>4381</b>	<b>2.53</b>	<b>-1.3</b>	<b>RGB</b>
201.66857	-47.47679	8.18	8.20	8.20	8.14	3945	3.22	-1.3	RGB
201.60159	-47.48298	9.50	9.53	9.41	9.49	4293	2.79	-1.3	RGB
<b>201.45634</b>	<b>-47.63360</b>	–	<b>10.23</b>	–	<b>10.18</b>	<b>4442</b>	<b>2.57</b>	<b>-1.3</b>	<b>RGB</b>
<b>201.70383</b>	<b>-47.49686</b>	<b>10.88</b>	<b>10.85</b>	<b>10.96</b>	<b>10.86</b>	<b>4609</b>	<b>2.33</b>	<b>-1.3</b>	<b>RGB</b>
201.54340	-47.51959	11.18	11.31	11.23	11.22	4724	2.20	-1.3	RGB
<b>201.62858</b>	<b>-47.49146</b>	<b>11.19</b>	<b>11.38</b>	<b>11.17</b>	<b>11.24</b>	<b>4721</b>	<b>2.20</b>	<b>-1.3</b>	<b>RGB</b>
<b>201.70070</b>	<b>-47.48011</b>	<b>11.34</b>	<b>11.35</b>	<b>11.34</b>	<b>11.42</b>	<b>4733</b>	<b>2.11</b>	<b>-1.3</b>	<b>RGB</b>
201.66968	-47.54969	–	10.45	11.82	10.27	4595	2.48	-1.6	RGB
<b>201.69797</b>	<b>-47.48715</b>	<b>11.40</b>	<b>11.43</b>	<b>11.38</b>	<b>11.41</b>	<b>4807</b>	<b>2.11</b>	<b>-1.6</b>	<b>RGB</b>
<b>201.70175</b>	<b>-47.49631</b>	<b>10.78</b>	<b>10.72</b>	<b>10.82</b>	<b>10.80</b>	<b>4687</b>	<b>2.37</b>	<b>-1.6</b>	<b>RGB</b>
<b>201.74358</b>	<b>-47.47208</b>	<b>11.40</b>	<b>11.31</b>	<b>11.27</b>	<b>11.30</b>	<b>4806</b>	<b>2.17</b>	<b>-1.6</b>	<b>RGB</b>
<b>201.64288</b>	<b>-47.51644</b>	<b>11.45</b>	<b>11.46</b>	<b>11.35</b>	<b>11.32</b>	<b>4935</b>	<b>2.17</b>	<b>-1.9</b>	<b>RGB</b>
<b>201.69099</b>	<b>-47.51343</b>	<b>11.32</b>	<b>11.25</b>	<b>11.39</b>	<b>11.34</b>	<b>4902</b>	<b>2.20</b>	<b>-1.9</b>	<b>RGB</b>

<sup>4</sup>van Leeuwen et al. (2000)

The fractional number  $f_{num}$ , which is the number of candidate dusty stars divided by the total number of stars in the mid-IR sample, was accounted in two suitable [Fe/H] intervals,  $[Fe/H] < -1.3$  and  $[Fe/H] \geq -1.3$ . Photometric incompleteness was not considered for this analysis. The final observed numbers of dusty RGB and AGB stars for the GC  $\omega$  Cen are reported in table 5.3.

Table 5.3: Counts for red giant stars in  $\omega$  Cen.

Type	$n_{dusty}$	[Fe/H]	[Fe/H] $\geq -1.3$	[Fe/H] $< -1.3$
AGB	18	0.11	0.040	0.070
RGB	16	0.02	0.013	0.008

To refine our selection, the observed catalogue is cleaned from field stars based on proper motions dataset from the Gaia<sup>5</sup> Data Release 2 (Gaia Collaboration et al., 2016, 2018). Gaia DR2 has determined proper motion for over 1 billion stars in the Galaxy, with uncertainties ranging from 0.1 to 1 mas yr<sup>-1</sup>. Gaia DR2 positions were cross-correlated against  $\omega$  Cen catalogue and there exist 1684 stars with proper motion information available in the same field of view of our catalogue. Then, stars within an angular distance of 2.5 arcminutes around the cluster centre were selected as cluster members. With that, the number of dusty candidates were reduced to 18 stars. Table 5.2 shows those stars marked in bold.

## 5.4 Mass-loss rate derivation

### 5.4.1 DUSTY

The radiation emitted by a star surrounded by a spherical dust shell is absorbed and re-emitted in mid-IR wavelengths by circumstellar dust. The profile and features of that output spectrum can be identified by the radiative transfer code DUSTY (Ivezic et al., 1999; Elitzur & Ivezić, 2001). DUSTY solves the radiative transfer equation for

<sup>5</sup>This work has made use of data from the European Space Agency (ESA) mission *Gaia* (<https://www.cosmos.esa.int/gaia>), processed by the *Gaia* Data Processing and Analysis Consortium (DPAC, <https://www.cosmos.esa.int/web/gaia/dpac/consortium>). Funding for the DPAC has been provided by national institutions, in particular the institutions participating in the *Gaia* Multilateral Agreement.

an object in a dusty environment, computing an emerging spectrum, the dust emission and temperature distribution. A modified version (Origlia et al., 2007) of the radiative transfer code DUSTY was used to estimate the ML rate at the IRAC wavelengths. A Kurucz stellar atmosphere model was adopted to create the spectral energy distribution of the stars. The dust is assumed to be a mixture of warm silicates. Origlia et al. (2007, 2010) have tested slight differences in the dust properties with no significant impact in the IRAC colours and ML rates. Radiation pressure is neglected as it does not affect the stars. The following are the input parameters needed to be set before running DUSTY:

- optical depth of the circumstellar dust  $\tau = 10^{-5} - 10^{-1} \mu m$
- grain radius  $a = 0.1 \mu m$
- grain density  $\rho_g = 3 \text{ g cm}^{-3}$
- density profile  $\eta \propto r^{-2}$
- inner dust temperature  $T_{in} = 1000 \text{ K}$
- dust radius in the inner shell  $r_{in} = 10^{14} \text{ cm}$
- dust radius in the outer shell  $r_{out} = 1000 r_{in}$
- dust-to-gas ratio  $\delta_0 = 200$
- expansion velocity  $v_{exp}^0 = 10 \text{ km s}^{-1}$

A grid of DUSTY models with empirical stellar temperature (the temperature derived from the  $(V - K)$  colour, see 5.1) and  $(K\text{-IRAC})$  colours of each dust excess candidate star was created. DUSTY output is the predictions of the dust optical depth, the emerging flux and the envelope radius. To derive the ML rate, the following formula (Origlia et al., 2007) is considered:

$$dM/dt = 4\pi r_{out}^2 \times \rho_{dust} \times v_{exp} \times \delta \quad (5.8)$$

where  $\rho_{dust} \propto \rho_g \tau_8 F_8(obs)/F_8(mod) D^2/r_{out}^2$  is the dust density,  $F_8(obs)$  and  $F_8(mod)$  are the observed and model dust emission for  $8\mu m$  and  $D$  is the distance to the cluster.

The gas-to-dust ratio has a lower limit of  $1/Z$ , where  $Z$  is the metallicity. The general assumptions are that the  $v_{exp}$  of the envelope is constant, which means that  $v_{exp}$  depends only on  $\delta$  and not on the metallicity, and should scale like  $\delta^{-0.5}$ .

## 5.4.2 Results

Mass loss rates have been computed for the RGB stars with measured dust excess, using the radiative transfer code DUSTY (Ivezic et al., 1999; Elitzur & Ivezić, 2001) in its modified version by Origlia et al. (2007) to model the circumstellar dust emission and the emerging spectrum at the IRAC wavelengths. The total ML for the metal-poor and metal-rich RGB sub-populations at a given metallicity ( $i$ ) has been computed by using the equation:

$$\Delta M = \sum_i \left( \frac{dM}{dt_i} \times \Delta t_i^{ML} \right) \quad (5.9)$$

where  $\frac{dM}{dt_i}$  is the average ML rate and  $\Delta t^{ML} = \Delta t \times f_{num}$  is the ML timescale and  $f_{num}$  is the fractional number. The evolutionary time  $\Delta t$  for the RGB considered for the derivation of the ML timescale is  $14 \pm 1 Myr$ , according to the  $\Delta t$  adopted by Origlia et al. (2014). Average ML rates are computed by averaging the values obtained for the individual stars.

Top panel in figure 5.7 shows the inferred values for the metal-poor (green dots) and metal-rich (red dots) RGB stars. Bottom panel in figure 5.7 shows the average total ML of RGB as a function of metallicity. Solid line is the fitting relation  $ML^{RGB} = 0.08 \times [Fe/H] + 0.24 \pm 0.03$  (*rms*), in units of  $M_{\odot}$ , derived by Origlia et al. (2014).

ML rates in our sample are in the range of  $1.27 \times 10^{-8}$  to  $1.80 \times 10^{-7} M_{\odot} yr^{-1}$ , which is somewhat below the rates found by Boyer et al. (2008),  $2.9$  to  $4.2 \times 10^{-7} M_{\odot} yr^{-1}$ , and Origlia et al. (2002),  $10^{-7}$  to  $10^{-6} M_{\odot} yr^{-1}$ .  $M_{bol}$  varies from  $-1.4$  to  $-3.9$ , but most stars have  $M_{bol} < -3.0$ ; ML increases with brighter luminosities.

The fact that only a fraction of RGB stars are losing mass means that ML is episodic.

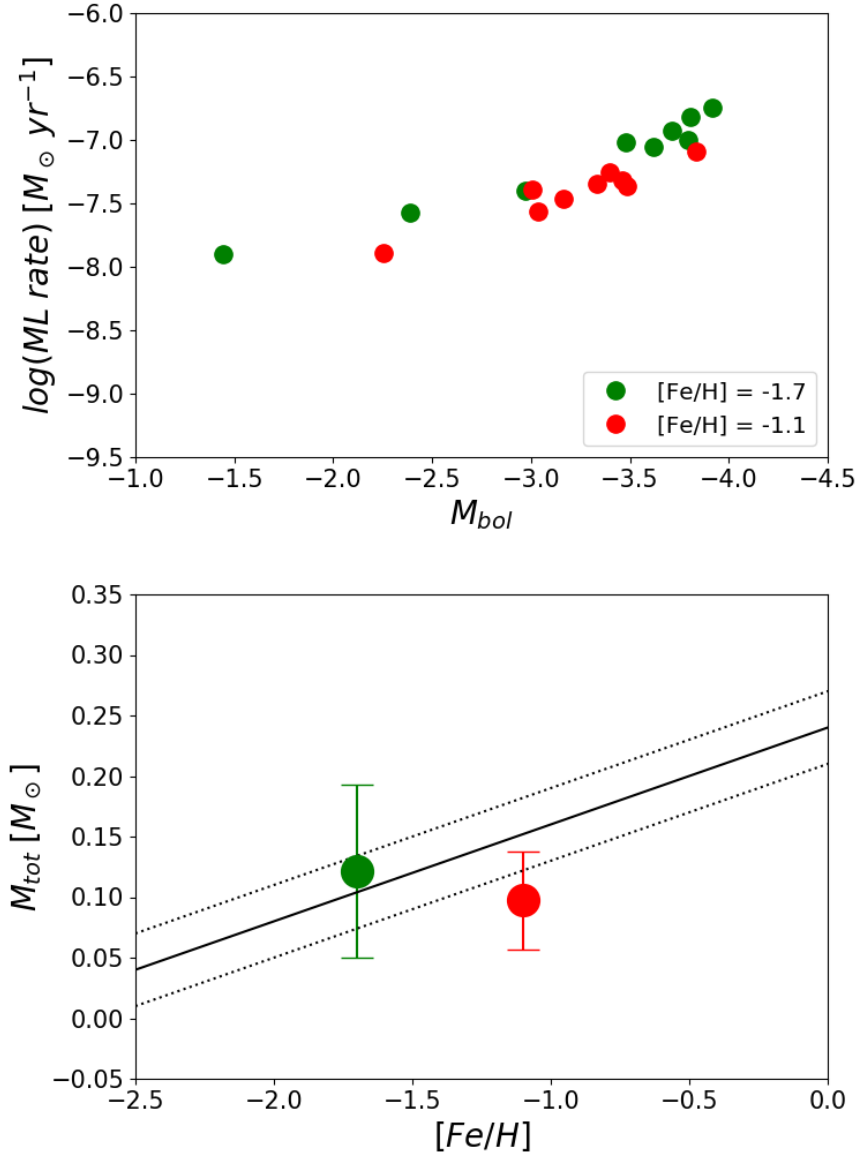


Figure 5.7: Top panel: ML rate as a function of the bolometric magnitude for the metal-poor (green) and metal-rich (red) RGB stars of  $\omega$  Cen with dust excess. Bottom panel: Average total mass lost by the metal-poor (green) and metal-rich (red) RGB sub-populations of  $\omega$  Cen. The error bars are the  $1\sigma$  uncertainty in the average total ML. The solid line is the fitting relation  $\pm 0.03$  rms (dotted lines) for the GGCs studied by Origlia et al. (2014), which is only shown for reference.

---

At a given luminosity, metal-poor stars have systematically slightly higher rates than metal-rich stars. Considering the  $1\sigma$  uncertainty of the average total ML, the results seem in agreement with the finding of Origlia et al. (2014) in their study of GGCs. ML depends minimally on metallicity, still it is possible to notice in the bottom panel of figure 5.7 that the steepness increases towards higher metallicities.

# Chapter 6

## Summary and Future work

### 6.1 Summary

The first chapter introduces the importance of closely scrutinising the SFH of low-mass spirals, taking advantage of the proximity of nearby systems to resolve its stellar population, as well as the importance of studying the process of ML of red giant stars in GC. The evolution with time of the SFR and the metallicity of a galaxy represents the SFH of that system, which is a necessary tool on the investigation of the formation and evolution of the Universe. M33 is one of the brightest spiral galaxies in the Local Group. Its vicinity allows us to observe and resolve its stellar populations. Past studies have suggested that M33 presents tidal interaction features, possibly from previous interactions with M31. Some studies have found age and metallicity gradient in the disc. Thereby, we provide the basis for pursuing the understanding of the SFH of star clusters in M33. Mass loss affects stellar evolution by altering evolutionary timescales, the chemical abundance in the stellar surface, and stellar luminosities.  $\omega$  Cen is a peculiar GC, exhibiting stellar populations with a vast range of ages and metallicities. Some studies have found ML occurring in stars near the TRGB. The objective of the study is to as accurately as possible determine the amount of mass that is lost by red giant stars and the ML dependence to the stellar metallicity for the GGC  $\omega$  Cen.

Chapter 2 briefly outlines the historical aspects that describes galaxy formation and evolution. By the hierarchical model point of view, the consecutive merger of small structures results in galaxies as we know them, implying that spiral galaxies are formed after only a few interactions. A general description of stellar evolution is given, including the transition from MS to giant branches, which is the starting point of one of the projects approached in this thesis. Stellar winds remove mass from stars at all evolutionary stages. The main mechanisms that drive the ML undergone on stars is also discussed. Chapter 2 closes with a succinct explanation of how the stellar radiation is captured by a telescope, the different photometric systems there exists to show the stellar flux in function of wavelength and how interstellar extinction affects the stellar brightness we see.

Chapter 3 gives some details of the photometry reductions and analyses carried out for the GGC  $\omega$  Cen and nearby galaxy M33. The former was observed with *Spitzer* telescope, in four different infrared channels, 3.6, 4.5, 5.8 and 8  $\mu m$ . The latter was observed in three optical filters,  $g'$ ,  $r'$  and  $i'$ , in the CFH telescope. Photometry was performed using DAOPHOT and IRAF softwares (Stetson, 1987) through the method of PFS-fitting.  $\omega$  Cen final catalogue sums about 4000 stars and the final catalogue for M33 adds up to a million stars.

Chapter 4 contains the characterization of the AST performed for M33 dataset. The purpose of the AST is to understand the impact of crowding on the stellar magnitudes and systematic effects in the photometry across the galaxy. In the one hand, crowding overestimates the real stellar brightness, leading to the wrong assumption of age, metallicity and mass of stars; on the other hand, the incompleteness interferes the stellar count, resulting in the wrong assumption of the IMF. The main concept of the method is to measure the input and output magnitude of fake stars added to the real image using the code ADDSTAR (Stetson, 1987), and asses the magnitude gradient and the number of stars lost during the photometric reductions.

In chapter 5 is presented the conversion of the magnitudes from the SDSS photometric system to the TCS system based on the colour relations of Carpenter (2001) and Alonso et al. (1998). The magnitude conversion is due to the colour-temperature equa-

tions used to calculate the  $T_{\text{eff}}$ , needed to generate the spectral energy distributions used in the radiative transfer code, being in different photometric filter systems. Following up, bolometric corrections and the effective temperature were derived according to Alonso et al. (1999). The selection of mass-losing stars candidate relies on (K - 8) colour excess method, 34 stars above  $\geq +2.0\sigma$  in colour on the red side of the CMD were flagged as dusty. A visual inspection of the CMD allowed us to segregate RGB from AGB, and a cross-correlation with a few LPV catalogues identified the LPV stars in the sample. PARSEC isochrones (Bressan et al., 2012) suitably interpolated were matched to individual stars to estimate their metallicity. Based on the proper motions from GAIA, field stars were discarded from the mass-losing candidate sample. To conclude, ML rates are derived for 18 RGB stars through the modelling of the circumstellar dust emission and the emerging spectrum at the IRAC wavelengths using the radiative transfer code DUSTY (Ivezic et al., 1999; Elitzur & Ivezić, 2001) in its modified version by Origlia et al. (2007).

## 6.2 Future work

### 6.2.1 M33

The adaptation of the code FIREs to use more than two photometric filters, as well as the SFH determination and tests with the results have been left for the future due to lack of time (i.e. the manipulation of large datasets are usually very time consuming, requiring even days to finish a single run). Future work concerns the use of the photometry and the AST previously obtained to determine the SFH.

The FIREs code has been developed to do this in a robust, objective, and autonomous way. The output of the code is the SFR and metallicity as function of age, which is all we need to describe the evolution of a galaxy baryonic component. To better understand how the galaxy formed and evolved, it will be interesting to first compare CMDs from small sub-regions located in different parts of the galaxy. This already contains information about qualitative differences in the underlying SFH of these dif-

ferent regions. This can be used as a guide for the quantitative exploration, across the whole system, of the SFH using the code FIREs. The only inputs of the code are the magnitudes and the isochrones already calculated. It uses a generic algorithm to find the SFH model with the maximum likelihood of representing the observed data. This is a computer-intensive process and the results will need to be analysed in detail for the whole galaxy and for each sub-region explored.

Another important test to perform is deeper analysis of the sensitivity of the method to the magnitude limit of the dataset. To accomplish this, synthetic CMDs need to be created based on a chosen SFH, and then the output SFH from the code can be compared with the chosen input. This can be repeated several times, each time considering a different magnitude limit of the synthetic data. In particular, it is also possible to explore the robustness of the method when the turn-off of the oldest population is not sampled. At this point, a SFH for many different regions of the galaxy will be available, and it will be possible to reconstruct its large scale evolution.

Regarding the AST, one could add fake stars near known Cepheid stars to understand how the magnitude of the Cepheids would be affected. Cepheids are important distance calibrators and an inaccurate measurement of their magnitudes would necessarily result in a systematic uncertainty in the distance estimate of other objects. Another possible investigation worth checking would be to include colour to the AST and analyse the impact of crowding on them. This is because other SFH methods (i.e. Harris & Zaritsky, 2001; Aparicio & Hidalgo, 2009; de Boer et al., 2012) are sensitive to colours.

### 6.2.2 $\omega$ Cen

Analysis of molecular lines and radial velocity of the mass-losing stars can help us to investigate deeply the mass motion from stellar winds and the origin of their emission. Emission detected in the wings of  $H\alpha$  lines in the spectra of GC red giants is an efficient way to probe the direct detection of mass outflow of those stars. One can make use of high resolution and high signal-to-noise spectroscopy to examine individual spectral

---

lines, such as  $H\alpha$  and CaII K lines, and their asymmetries that characterize gas motions in the stellar atmosphere, in the optical in order to measure the mass outflow velocities. Mg II lines are also worth checking as they form higher in the atmosphere, when compared to  $H\alpha$  and CaII K lines, suggesting that the stellar winds become more noticeable near the top of the chromosphere.

The same science could be reapplied for data with better spatial resolution. The James Webb Space Telescope facility will provide state-of-art spectrophotometric data that will enable the continuous investigation of the mass ejection of GC red giants. The NIR camera aboard of the James Webb Space Telescope has a field of view of  $2.2' \times 2.2'$  with an angular resolution of  $0.07''$  at  $2\mu$ .

# Appendix A

## Complementary tables

Table A.1 presents the aperture correction and error for each subimage in the three CFHT filters:

Table A.1: Aperture correction and error for the subimages of g', r' and i' filters.

<i>img</i>	ap corr	error	<i>img</i>	ap corr	error	<i>img</i>	ap corr	error
1g	-0.785	0.0376	1r	-0.738	0.0349	1i	-0.604	0.0286
2g	-0.768	0.0373	2r	-0.727	0.0344	2i	-0.584	0.0279
3g	-0.783	0.0374	3r	-0.723	0.0343	3i	-0.585	0.0277
4g	-0.758	0.0364	4r	-0.683	0.0322	4i	-0.546	0.0262
5g	-0.729	0.0358	5r	-0.660	0.0315	5i	-0.538	0.0258
6g	-0.743	0.0358	6r	-0.657	0.0315	6i	-0.540	0.0256
7g	-0.756	0.0362	7r	-0.682	0.0318	7i	-0.565	0.0261
8g	-0.745	0.0360	8r	-0.678	0.0316	8i	-0.539	0.0254
9g	-0.750	0.0364	9r	-0.691	0.0324	9i	-0.552	0.0258
10g	-0.738	0.0358	10r	-0.696	0.0326	10i	-0.547	0.0260
11g	-0.713	0.0352	11r	-0.719	0.0342	11i	-0.566	0.0269
13g	-0.788	0.0372	13r	-0.737	0.0342	13i	-0.585	0.0273
14g	-0.763	0.0367	14r	-0.691	0.0331	14i	-0.555	0.0266
15g	-0.749	0.0361	15r	-0.663	0.0316	15i	-0.564	0.0264
16g	-0.711	0.0349	16r	-0.640	0.0308	16i	-0.520	0.0249
17g	-0.700	0.0346	17r	-0.639	0.0304	17i	-0.517	0.0247
18g	-0.711	0.0348	18r	-0.647	0.0307	18i	-0.515	0.0245
19g	-0.726	0.0349	19r	-0.656	0.0305	19i	-0.519	0.0242

Continue on next page...

Table A.1 – Continued from previous page

<i>img</i>	ap corr	error	<i>img</i>	ap corr	error	<i>img</i>	ap corr	error
20g	-0.707	0.0344	20r	-0.647	0.0303	20i	-0.521	0.0244
21g	-0.721	0.0344	21r	-0.684	0.0310	21i	-0.542	0.0247
22g	-0.725	0.0353	22r	-0.663	0.0316	22i	-0.534	0.0254
23g	-0.708	0.0351	23r	-0.693	0.0330	23i	-0.546	0.0262
25g	-0.759	0.0357	25r	-0.691	0.0323	25i	-0.549	0.0256
26g	-0.715	0.0348	26r	-0.668	0.0313	26i	-0.536	0.0249
27g	-0.737	0.0352	27r	-0.660	0.0309	27i	-0.520	0.0245
28g	-0.708	0.0338	28r	-0.640	0.0297	28i	-0.513	0.0236
29g	-0.684	0.0330	29r	-0.814	0.0311	29i	-0.536	0.0236
30g	-0.716	0.0332	30r	-0.653	0.0292	30i	-0.547	0.0234
31g	-0.740	0.0335	31r	-0.699	0.0295	31i	-0.574	0.0235
32g	-0.727	0.0335	32r	-0.682	0.0297	32i	-0.558	0.0234
33g	-0.703	0.0335	33r	-0.683	0.0304	33i	-0.564	0.0242
34g	-0.726	0.0343	34r	-0.690	0.0311	34i	-0.558	0.0246
35g	-0.705	0.0346	35r	-0.669	0.0318	35i	-0.558	0.0255
37g	-0.716	0.0347	37r	-0.658	0.0314	37i	-0.519	0.0246
38g	-0.700	0.0341	38r	-0.636	0.0304	38i	-0.522	0.0241
39g	-0.705	0.0337	39r	-0.649	0.0301	39i	-0.537	0.0239
40g	-0.717	0.0324	40r	-0.671	0.0287	40i	-0.576	0.0231
41g	-0.735	0.0322	41r	-0.702	0.0288	41i	-0.592	0.0229
42g	-0.797	0.0326	42r	-0.750	0.0293	42i	-0.632	0.0233
43g	-0.840	0.0327	43r	-0.812	0.0300	43i	-0.719	0.0244
44g	-0.748	0.0319	44r	-0.958	0.0324	44i	-0.671	0.0239
45g	-0.768	0.0334	45r	-0.757	0.0304	45i	-0.655	0.0242
46g	-0.742	0.0340	46r	-0.700	0.0306	46i	-0.597	0.0244
47g	-0.748	0.0347	47r	-0.717	0.0318	47i	-0.597	0.0255
49g	-0.718	0.0343	49r	-0.686	0.0312	49i	-0.540	0.0245
50g	-0.699	0.0332	50r	-0.727	0.0304	50i	-0.544	0.0238
51g	-0.724	0.0331	51r	-0.790	0.0307	51i	-0.618	0.0241
52g	-0.771	0.0319	52r	-0.839	0.0301	52i	-0.658	0.0237
53g	-0.802	0.0313	53r	-0.820	0.0299	53i	-0.732	0.0246
54g	-0.821	0.0316	54r	-0.859	0.0306	54i	-0.770	0.0255
55g	-0.808	0.0315	55r	-0.866	0.0307	55i	-0.778	0.0256
56g	-0.820	0.0319	56r	-0.841	0.0305	56i	-0.740	0.0248

Continue on next page...

Table A.1 – Continued from previous page

<i>img</i>	ap corr	error	<i>img</i>	ap corr	error	<i>img</i>	ap corr	error
57g	-0.839	0.0339	57r	-0.803	0.0311	57i	-0.770	0.0261
58g	-0.775	0.0342	58r	-0.757	0.0312	58i	-0.638	0.0249
59g	-0.800	0.0356	59r	-0.751	0.0323	59i	-0.633	0.0258
61g	-0.700	0.0334	61r	-0.695	0.0309	61i	-0.565	0.0244
62g	-0.742	0.0330	62r	-0.704	0.0299	62i	-0.604	0.0241
63g	-0.827	0.0333	63r	-0.827	0.0303	63i	-0.694	0.0245
64g	-0.793	0.0316	64r	-0.874	0.0306	64i	-0.764	0.0251
65g	-0.807	0.0312	65r	-0.898	0.0310	65i	-0.799	0.0260
66g	-0.796	0.0310	66r	-0.903	0.0315	66i	-0.828	0.0277
67g	-0.803	0.0312	67r	-0.891	0.0315	67i	-0.803	0.0266
68g	-0.811	0.0314	68r	-0.866	0.0309	68i	-0.762	0.0254
69g	-0.807	0.0324	69r	-0.798	0.0307	69i	-0.724	0.0253
70g	-0.774	0.0332	70r	-0.742	0.0303	70i	-0.649	0.0244
71g	-0.732	0.0341	71r	-0.694	0.0313	71i	-0.585	0.0250
73g	-0.712	0.0331	73r	-0.681	0.0305	73i	-0.538	0.0239
74g	-0.747	0.0322	74r	-0.707	0.0295	74i	-0.567	0.0234
75g	-0.835	0.0329	75r	-0.782	0.0301	75i	-0.604	0.0235
76g	-0.797	0.0314	76r	-0.851	0.0305	76i	-0.804	0.0261
77g	-0.812	0.0309	77r	-0.878	0.0307	77i	-0.772	0.0252
78g	-0.781	0.0305	78r	-0.874	0.0311	78i	-0.766	0.0255
79g	-0.804	0.0306	79r	-0.857	0.0308	79i	-0.754	0.0252
80g	-0.742	0.0303	80r	-0.779	0.0301	80i	-0.709	0.0245
81g	-0.729	0.0312	81r	-0.719	0.0300	81i	-0.617	0.0238
82g	-0.704	0.0320	82r	-0.679	0.0300	82i	-0.564	0.0236
83g	-0.685	0.0332	83r	-0.652	0.0308	83i	-0.530	0.0246
85g	-0.722	0.0332	85r	-0.711	0.0309	85i	-0.565	0.0242
86g	-0.723	0.0323	86r	-0.704	0.0298	86i	-0.575	0.0236
87g	-0.770	0.0320	87r	-0.756	0.0297	87i	-0.578	0.0231
88g	-0.793	0.0317	88r	-0.769	0.0297	88i	-0.603	0.0232
89g	-0.785	0.0307	89r	-0.815	0.0298	89i	-0.564	0.0222
90g	-0.775	0.0305	90r	-0.778	0.0297	90i	-0.691	0.0238
91g	-0.716	0.0296	91r	-0.726	0.0291	91i	-0.643	0.0232
92g	-0.730	0.0304	92r	-0.718	0.0295	92i	-0.618	0.0231
93g	-0.696	0.0311	93r	-0.695	0.0298	93i	-0.570	0.0234

Continue on next page...

Table A.1 – Continued from previous page

<i>img</i>	ap corr	error	<i>img</i>	ap corr	error	<i>img</i>	ap corr	error
94 $g$	-0.675	0.0318	94 $r$	-0.659	0.0303	94 $i$	-0.523	0.0236
95 $g$	-0.680	0.0326	95 $r$	-0.649	0.0311	95 $i$	-0.516	0.0243
97 $g$	-0.675	0.0322	97 $r$	-0.686	0.0315	97 $i$	-0.535	0.0245
98 $g$	-0.709	0.0323	98 $r$	-0.675	0.0302	98 $i$	-0.538	0.0237
99 $g$	-0.745	0.0319	99 $r$	-0.716	0.0299	99 $i$	-0.567	0.0232
100 $g$	-0.739	0.0315	100 $r$	-0.707	0.0295	100 $i$	-0.550	0.0229
101 $g$	-0.733	0.0306	101 $r$	-0.720	0.0292	101 $i$	-0.620	0.0232
102 $g$	-0.739	0.0303	102 $r$	-0.737	0.0294	102 $i$	-0.622	0.0230
103 $g$	-0.665	0.0297	103 $r$	-0.639	0.0287	103 $i$	-0.566	0.0227
104 $g$	-0.673	0.0303	104 $r$	-0.657	0.0293	104 $i$	-0.528	0.0226
105 $g$	-0.655	0.0308	105 $r$	-0.657	0.0301	105 $i$	-0.520	0.0236
106 $g$	-0.676	0.0324	106 $r$	-0.664	0.0313	106 $i$	-0.529	0.0245
107 $g$	-0.689	0.0334	107 $r$	-0.663	0.0322	107 $i$	-0.524	0.0256
109 $g$	-0.702	0.0338	109 $r$	-0.711	0.0328	109 $i$	-0.542	0.0253
110 $g$	-0.685	0.0328	110 $r$	-0.662	0.0313	110 $i$	-0.530	0.0245
111 $g$	-0.694	0.0324	111 $r$	-0.668	0.0308	111 $i$	-0.523	0.0238
112 $g$	-0.653	0.0310	112 $r$	-0.635	0.0296	112 $i$	-0.505	0.0227
113 $g$	-0.683	0.0309	113 $r$	-0.639	0.0292	113 $i$	-0.524	0.0227
114 $g$	-0.657	0.0305	114 $r$	-0.664	0.0297	114 $i$	-0.516	0.0228
115 $g$	-0.644	0.0306	115 $r$	-0.650	0.0299	115 $i$	-0.511	0.0230
116 $g$	-0.646	0.0308	116 $r$	-0.643	0.0302	116 $i$	-0.503	0.0233
117 $g$	-0.683	0.0322	117 $r$	-0.668	0.0310	117 $i$	-0.517	0.0243
118 $g$	-0.681	0.0333	118 $r$	-0.666	0.0325	118 $i$	-0.529	0.0255
119 $g$	-0.705	0.0344	119 $r$	-0.709	0.0345	119 $i$	-0.564	0.0274
121 $g$	-0.710	0.0349	121 $r$	-0.715	0.0348	121 $i$	-0.576	0.0278
122 $g$	-0.710	0.0343	122 $r$	-0.720	0.0341	122 $i$	-0.554	0.0264
123 $g$	-0.723	0.0342	123 $r$	-0.698	0.0330	123 $i$	-0.531	0.0255
124 $g$	-0.693	0.0326	124 $r$	-0.672	0.0311	124 $i$	-0.515	0.0243
125 $g$	-0.652	0.0319	125 $r$	-0.656	0.0310	125 $i$	-0.512	0.0241
126 $g$	-0.668	0.0325	126 $r$	-0.651	0.0312	126 $i$	-0.515	0.0241
127 $g$	-0.662	0.0319	127 $r$	-0.647	0.0312	127 $i$	-0.495	0.0239
128 $g$	-0.670	0.0323	128 $r$	-0.658	0.0313	128 $i$	-0.534	0.0249
129 $g$	-0.676	0.0329	129 $r$	-0.690	0.0325	129 $i$	-0.552	0.0258
130 $g$	-0.691	0.0339	130 $r$	-0.696	0.0340	130 $i$	-0.554	0.0273

Continue on next page...

Table A.1 – Continued from previous page

<i>img</i>	ap corr	error	<i>img</i>	ap corr	error	<i>img</i>	ap corr	error
131 $g$	-0.727	0.0355	131 $r$	-0.734	0.0361	131 $i$	-0.588	0.0292

Table A.2 presents the offset correction and error between each subimage in the three CFHT filters:

Table A.2: Offset correction and error for the subimages of  $g'$ ,  $r'$  and  $i'$  filters.

img'1	img'2	offset	error	img'1	img'2	offset	error	img'1	img'2	offset	error
1	13 $g$	-0.03	0.0037	1	13 $r$	0.033	0.0030	1	13 $i$	0.045	0.0023
2	14 $g$	0.073	0.0023	2	14 $r$	0.108	0.0017	2	14 $i$	0.066	0.0014
3	15 $g$	0.082	0.0027	3	15 $r$	0.102	0.0023	3	15 $i$	0.084	0.0021
4	16 $g$	0.085	0.0014	4	16 $r$	0.091	0.0013	4	16 $i$	0.110	0.0015
5	17 $g$	0.051	0.0016	5	17 $r$	0.083	0.0012	5	17 $i$	0.063	0.0013
6	18 $g$	0.094	0.0023	6	18 $r$	0.047	0.0017	6	18 $i$	0.107	0.0019
7	19 $g$	0.162	0.0019	7	19 $r$	0.050	0.0013	7	19 $i$	0.137	0.0017
8	20 $g$	0.082	0.0024	8	20 $r$	0.096	0.0016	8	20 $i$	0.111	0.0012
9	21 $g$	0.037	0.0026	9	21 $r$	0.126	0.0026	9	21 $i$	0.146	0.0017
10	22 $g$	0.069	0.0016	10	22 $r$	0.048	0.0013	10	22 $i$	0.063	0.0013
11	23 $g$	0.100	0.0016	11	23 $r$	0.007	0.0011	11	23 $i$	0.020	0.0012
13	25 $g$	0.038	0.0102	13	25 $r$	0.055	0.0090	13	25 $i$	0.083	0.0048
14	26 $g$	0.069	0.0056	14	26 $r$	0.102	0.0040	14	26 $i$	0.074	0.0024
15	27 $g$	0.069	0.0015	15	27 $r$	0.099	0.0015	15	27 $i$	0.068	0.0020
16	28 $g$	0.084	0.0016	16	28 $r$	0.117	0.0015	16	28 $i$	0.086	0.0014
17	29 $g$	0.058	0.0012	17	29 $r$	0.074	0.0016	17	29 $i$	0.065	0.0012
18	30 $g$	0.082	0.0016	18	30 $r$	0.060	0.0011	18	30 $i$	0.096	0.0009
19	31 $g$	0.143	0.0017	19	31 $r$	0.022	0.0012	19	31 $i$	0.077	0.0009
20	32 $g$	0.057	0.0015	20	32 $r$	0.052	0.0012	20	32 $i$	0.112	0.0009
21	33 $g$	0.054	0.0012	21	33 $r$	0.107	0.0011	21	33 $i$	0.130	0.0009
22	34 $g$	0.064	0.0020	22	34 $r$	0.068	0.0013	22	34 $i$	0.048	0.0009
23	35 $g$	0.075	0.0013	23	35 $r$	0.024	0.0010	23	35 $i$	0.044	0.0009
25	37 $g$	0.041	0.0018	25	37 $r$	0.040	0.0015	25	37 $i$	0.069	0.0019
26	38 $g$	0.061	0.0014	26	38 $r$	0.080	0.0012	26	38 $i$	0.069	0.0012
27	39 $g$	0.061	0.0015	27	39 $r$	0.119	0.0017	27	39 $i$	0.077	0.0014
28	40 $g$	0.056	0.0016	28	40 $r$	0.083	0.0012	28	40 $i$	0.069	0.0009

Continue on next page...

Table A.2 – Continued from previous page

img'1	img'2	offset	error	img'1	img'2	offset	error	img'1	img'2	offset	error
29	41 $g$	0.057	0.0008	29	41 $r$	-0.02	0.0010	29	41 $i$	0.048	0.0007
30	42 $g$	0.071	0.0009	30	42 $r$	0.035	0.0008	30	42 $i$	0.082	0.0006
31	43 $g$	0.044	0.0007	31	43 $r$	-0.00	0.0007	31	43 $i$	0.044	0.0006
32	44 $g$	0.023	0.0011	32	44 $r$	0.022	0.0010	32	44 $i$	0.077	0.0006
33	45 $g$	0.055	0.0011	33	45 $r$	0.101	0.0010	33	45 $i$	0.122	0.0008
34	46 $g$	0.042	0.0013	34	46 $r$	0.039	0.0011	34	46 $i$	0.048	0.0008
35	47 $g$	0.067	0.0009	35	47 $r$	0.032	0.0008	35	47 $i$	0.034	0.0006
37	49 $g$	0.050	0.0017	37	49 $r$	0.046	0.0014	37	49 $i$	0.047	0.0017
38	50 $g$	0.079	0.0015	38	50 $r$	0.074	0.0013	38	50 $i$	0.076	0.0009
39	51 $g$	0.049	0.0011	39	51 $r$	0.082	0.0010	39	51 $i$	0.060	0.0008
40	52 $g$	0.035	0.0008	40	52 $r$	0.054	0.0008	40	52 $i$	0.031	0.0007
41	53 $g$	0.067	0.0008	41	53 $r$	0.018	0.0008	41	53 $i$	0.023	0.0006
42	54 $g$	0.025	0.0006	42	54 $r$	-0.01	0.0006	42	54 $i$	0.025	0.0005
43	55 $g$	-0.01	0.0005	43	55 $r$	-0.02	0.0005	43	55 $i$	0.001	0.0005
44	56 $g$	0.022	0.0006	44	56 $r$	-0.05	0.0007	44	56 $i$	0.043	0.0005
45	57 $g$	-0.00	0.0008	45	57 $r$	0.067	0.0008	45	57 $i$	0.080	0.0006
46	58 $g$	0.033	0.0007	46	58 $r$	0.024	0.0008	46	58 $i$	0.015	0.0006
47	59 $g$	0.037	0.0009	47	59 $r$	0.004	0.0008	47	59 $i$	0.024	0.0007
49	61 $g$	0.057	0.0021	49	61 $r$	0.047	0.0014	49	61 $i$	0.060	0.0013
50	62 $g$	0.060	0.0013	50	62 $r$	0.025	0.0011	50	62 $i$	0.055	0.0008
51	63 $g$	0.045	0.0009	51	63 $r$	0.025	0.0010	51	63 $i$	-0.00	0.0007
52	64 $g$	0.011	0.0007	52	64 $r$	-0.00	0.0007	52	64 $i$	0.004	0.0006
53	65 $g$	-0.00	0.0006	53	65 $r$	0.005	0.0007	53	65 $i$	-0.04	0.0005
54	66 $g$	-0.00	0.0005	54	66 $r$	-0.02	0.0005	54	66 $i$	-0.05	0.0005
55	67 $g$	-0.00	0.0005	55	67 $r$	-0.06	0.0006	55	67 $i$	-0.03	0.0004
56	68 $g$	0.012	0.0005	56	68 $r$	-0.01	0.0005	56	68 $i$	-0.01	0.0005
57	69 $g$	-0.01	0.0007	57	69 $r$	-0.00	0.0007	57	69 $i$	-0.02	0.0006
58	70 $g$	0.024	0.0008	58	70 $r$	-0.01	0.0008	58	70 $i$	-0.00	0.0006
59	71 $g$	0.027	0.0007	59	71 $r$	-0.01	0.0007	59	71 $i$	-0.01	0.0006
	62 $g$	0.055	0.0011		62 $r$	0.057	0.0010		62 $i$	0.052	0.0008
61	73 $g$	-0.06	0.0015	61	73 $r$	-0.04	0.0012	61	73 $i$	-0.06	0.0011
	63 $g$	0.033	0.0008		63 $r$	0.032	0.0008		63 $i$	0.017	0.0006
62	74 $g$	-0.00	0.0010	62	74 $r$	0.004	0.0008	62	74 $i$	-0.02	0.0007
	64 $g$	-0.00	0.0008		64 $r$	-0.03	0.0002		64 $i$	0.021	0.0007
63				63				63			

Continue on next page...

Table A.2 – Continued from previous page

img'1	img'2	offset	error	img'1	img'2	offset	error	img'1	img'2	offset	error
	75g	-0.00	0.0005		75r	-0.02	0.0006		75i	-0.03	0.0005
64	65g	-0.03	0.0006	64	65r	-0.01	0.0007	64	65i	0.016	0.0005
	76g	0.032	0.0007		76r	0.020	0.0007		76i	0.028	0.0005
65	66g	-0.03	0.0004	65	66r	-0.08	0.0005	65	66i	0.046	0.0004
	77g	-0.03	0.0004		77r	0.002	0.0005		77i	0.032	0.0004
66	67g	0.007	0.0005	66	67r	-0.02	0.0005	66	67i	0.032	0.0005
	78g	-0.01	0.0004		78r	0.068	0.0005		78i	0.021	0.0005
67	68g	-0.02	0.0005	67	68r	-0.09	0.0006	67	68i	0.033	0.0005
	79g	-0.02	0.0005		79r	-0.00	0.0005		79i	-0.02	0.0005
68	69g	-0.02	0.0005	68	69r	-0.01	0.0005	68	69i	0.026	0.0005
	80g	-0.02	0.0007		80r	0.001	0.0007		80i	0.026	0.0005
69	70g	-0.01	0.0008	69	70r	0.004	0.0008	69	70i	0.022	0.0006
	81g	-0.10	0.0008		81r	-0.01	0.0008		81i	-0.02	0.0006
70	71g	-0.05	0.0008	70	71r	-0.00	0.0008	70	71i	-0.01	0.0007
	82g	-0.05	0.0008		82r	-0.05	0.0008		82i	-0.04	0.0006
71	83g	-0.07	0.0008	71	83r	-0.02	0.0008	71	83i	-0.04	0.0007
73	85g	-0.04	0.0013	73	85r	-0.03	0.0011	73	85i	-0.04	0.0009
74	86g	-0.01	0.0008	74	86r	-0.00	0.0008	74	86i	-0.02	0.0006
75	87g	0.002	0.0009	75	87r	0.000	0.0009	75	87i	-0.02	0.0006
76	88g	0.005	0.0006	76	88r	0.061	0.0007	76	88i	-0.05	0.0005
77	89g	-0.01	0.0005	77	89r	0.010	0.0006	77	89i	-0.07	0.0004
78	90g	-0.03	0.0006	78	90r	-0.01	0.0006	78	90i	0.051	0.0005
79	91g	-0.04	0.0007	79	91r	-0.02	0.0007	79	91i	-0.03	0.0005
80	92g	-0.04	0.0007	80	92r	-0.01	0.0007	80	92i	-0.01	0.0006
81	93g	-0.05	0.0006	81	93r	-0.02	0.0007	81	93i	-0.05	0.0006
82	94g	-0.08	0.0012	82	94r	-0.07	0.0011	82	94i	-0.07	0.0008
83	95g	-0.05	0.0020	83	95r	-0.04	0.0017	83	95i	-0.04	0.0012
85	97g	-0.03	0.0014	85	97r	-0.01	0.0015	85	97i	-0.09	0.0010
86	98g	-0.02	0.0010	86	98r	-0.01	0.0009	86	98i	-0.02	0.0007
87	99g	0.012	0.0008	87	99r	-0.00	0.0008	87	99i	-0.02	0.0006
88	100g	0.012	0.0008	88	100r	0.015	0.0008	88	100i	-0.03	0.0006
89	101g	-0.04	0.0005	89	101r	-0.04	0.0006	89	101i	-0.05	0.0005
90	102g	-0.03	0.0005	90	102r	-0.02	0.0005	90	102i	0.013	0.0005
91	103g	-0.04	0.0008	91	103r	-0.07	0.0008	91	103i	-0.05	0.0006

Continue on next page...

Table A.2 – Continued from previous page

img'1	img'2	offset	error	img'1	img'2	offset	error	img'1	img'2	offset	error
92	104 $g$	-0.06	0.0008	92	104 $r$	-0.06	0.0009	92	104 $i$	-0.05	0.0007
93	105 $g$	-0.06	0.0014	93	105 $r$	-0.06	0.0012	93	105 $i$	-0.09	0.0010
94	106 $g$	-0.09	0.0013	94	106 $r$	-0.09	0.0013	94	106 $i$	-0.08	0.0009
95	107 $g$	-0.09	0.0015	95	107 $r$	-0.03	0.0012	95	107 $i$	-0.05	0.0010
97	109 $g$	-0.06	0.0019	97	109 $r$	-0.04	0.0016	97	109 $i$	-0.12	0.0016
98	110 $g$	-0.02	0.0016	98	110 $r$	-0.01	0.0013	98	110 $i$	-0.02	0.0010
99	111 $g$	-0.00	0.0012	99	111 $r$	-0.03	0.0011	99	111 $i$	-0.05	0.0008
100	112 $g$	-0.04	0.0009	100	112 $r$	-0.03	0.0009	100	112 $i$	-0.04	0.0007
101	113 $g$	-0.07	0.0007	101	113 $r$	-0.08	0.0007	101	113 $i$	-0.07	0.0006
102	114 $g$	-0.09	0.0011	102	114 $r$	-0.06	0.0010	102	114 $i$	-0.04	0.0008
103	115 $g$	-0.07	0.0015	103	115 $r$	-0.09	0.0011	103	115 $i$	-0.11	0.0008
104	116 $g$	-0.12	0.0021	104	116 $r$	-0.11	0.0015	104	116 $i$	-0.07	0.0013
105	117 $g$	-0.09	0.0020	105	117 $r$	-0.09	0.0014	105	117 $i$	-0.10	0.0014
106	118 $g$	-0.09	0.0021	106	118 $r$	-0.09	0.0016	106	118 $i$	-0.08	0.0012
107	119 $g$	-0.07	0.0022	107	119 $r$	-0.06	0.0016	107	119 $i$	-0.09	0.0016
109	121 $g$	-0.03	0.0019	109	121 $r$	-0.05	0.0021	109	121 $i$	-0.08	0.0020
110	122 $g$	-0.04	0.0020	110	122 $r$	-0.01	0.0030	110	122 $i$	-0.03	0.0018
111	123 $g$	0.017	0.0025	111	123 $r$	0.004	0.0019	111	123 $i$	-0.07	0.0018
112	124 $g$	-0.06	0.0024	112	124 $r$	-0.06	0.0015	112	124 $i$	-0.05	0.0020
113	125 $g$	-0.08	0.0021	113	125 $r$	-0.11	0.0016	113	125 $i$	-0.08	0.0017
114	126 $g$	-0.07	0.0027	114	126 $r$	-0.07	0.0020	114	126 $i$	-0.03	0.0016
115	127 $g$	-0.05	0.0015	115	127 $r$	-0.07	0.0024	115	127 $i$	-0.12	0.0020
116	128 $g$	-0.11	0.0019	116	128 $r$	-0.10	0.0013	116	128 $i$	-0.07	0.0020
117	129 $g$	-0.09	0.0035	117	129 $r$	-0.06	0.0024	117	129 $i$	-0.09	0.0019
118	130 $g$	-0.07	0.0024	118	130 $r$	-0.08	0.0024	118	130 $i$	-0.07	0.0022
119	131 $g$	-0.05	0.0021	119	131 $r$	-0.03	0.0017	119	131 $i$	-0.08	0.0018

Table A.3 presents the coefficients zero point, colour term and  $A_*$  for the transformation equation of each chip reached by KT:

Table A.3: Photometric solutions for the coefficients zero point, colour term and  $A_*$  by KT.

chip	$Z$	$C$	$A_1$	$A_2$
------	-----	-----	-------	-------

Continue on next page...

Table A.3 – Continued from previous page

chip	$Z$	$C$	$A_1$	$A_2$
$g'$				
0	-30.193	-0.173	$4.372e-5$	$1.175e-5$
1	-30.092	-0.167	$-1.962e-5$	$1.723e-5$
2	-29.674	-0.175	$4.834e-5$	$-2.755e-5$
3	-27.965	-0.137	$-9.068e-5$	$-7.569e-5$
4	-30.120	-0.159	$1.250e-5$	$2.047e-6$
5	-29.605	-0.128	$-2.718e-5$	$-1.617e-6$
6	-30.576	-0.216	$2.818e-5$	$1.564e-5$
7	-23.855	-0.135	$-2.560e-4$	$-1.205e-4$
8 <sup>1</sup>	–	–	–	–
9	-29.564	-0.214	$-2.395e-5$	$-7.504e-6$
10	-29.426	-0.154	$-1.462e-4$	$1.244e-5$
11	-29.869	-0.173	$-2.172e-5$	$4.956e-6$
12	-29.990	-0.167	$1.940e-5$	$-1.081e-5$
13	-29.791	-0.182	$-9.038e-6$	$-4.858e-6$
14	-29.378	-0.154	$-9.098e-6$	$-3.260e-5$
15	-30.567	-0.155	$3.859e-5$	$3.482e-6$
16	-30.733	-0.179	$2.684e-5$	$2.698e-5$
17	-30.506	-0.182	$-3.314e-7$	$4.883e-5$
18	-29.570	-0.211	$-1.305e-5$	$-2.268e-5$
19	-29.488	-0.204	$-6.806e-5$	$-1.434e-5$
20	-29.689	-0.288	$-2.387e-5$	$1.165e-5$
21	-29.263	-0.158	$-8.098e-6$	$-7.215e-5$
22	-29.669	-0.197	$-1.115e-5$	$-2.272e-5$
23	-30.040	-0.159	$1.486e-6$	$4.744e-6$
24	-30.573	-0.171	$5.133e-5$	$-1.601e-5$
25	-30.572	-0.149	$3.879e-5$	$1.209e-5$
26	-29.181	-0.175	$-2.174e-5$	$-4.541e-5$
27	-29.796	-0.216	$-6.946e-6$	$2.493e-5$
28	-29.655	-0.196	$-5.228e-5$	$3.225e-6$
29	-30.046	-0.220	$4.277e-5$	$-1.148e-6$
30	-29.615	-0.183	$-2.807e-5$	$-1.016e-5$

Continue on next page...

<sup>1</sup>There is no solution for CFHT chip 8 as there are too few stars in that region in the INT data for calibration.

Table A.3 – Continued from previous page

chip	$Z$	$C$	$A_1$	$A_2$
31	-29.744	-0.158	$-2.127e-5$	$1.256e-5$
32	-29.740	-0.169	$-1.648e-5$	$1.665e-5$
33	-30.059	-0.166	$5.924e-6$	$1.755e-5$
34	-29.127	-0.161	$-5.716e-5$	$3.171e-5$
35	-30.238	-0.171	$1.222e-5$	$1.700e-5$
<hr/>				
r'				
0	-29.897	-0.008	$-3.660e-5$	$4.104e-6$
1	-30.111	-0.013	$-1.244e-5$	$1.432e-5$
2	-30.456	-0.015	$9.308e-6$	$2.904e-5$
3	-28.482	-0.005	$-2.734e-4$	$3.355e-5$
4	-29.669	-0.023	$-1.442e-5$	$-5.461e-6$
5	-29.989	-0.017	$-1.627e-5$	$1.427e-5$
6	-31.137	-0.026	$3.150e-5$	$4.310e-5$
7	-27.159	0.029	$-2.069e-4$	$2.545e-5$
8 <sup>2</sup>	–	–	–	–
9	-29.805	-0.007	$-1.766e-5$	$-6.846e-6$
10	-29.441	-0.027	$-4.051e-5$	$-2.658e-5$
11	-29.945	-0.033	$1.242e-5$	$-1.612e-6$
12	-29.877	-0.058	$2.378e-6$	$-3.882e-6$
13	-29.654	-0.021	$-2.726e-5$	$3.489e-6$
14	-29.219	-0.029	$-2.810e-5$	$-2.193e-5$
15	-30.010	-0.014	$1.363e-5$	$-8.222e-6$
16	-30.362	$-1.256e-4$	$1.716e-5$	$1.179e-5$
17	-29.877	-0.019	$-1.048e-5$	$1.166e-5$
18	-29.794	-0.007	$-4.478e-5$	$-8.475e-6$
19	-30.040	-0.011	$-2.292e-6$	$1.028e-5$
20	-29.950	-0.020	$4.017e-7$	$2.051e-6$
21	-30.610	0.003	$7.964e-5$	$4.416e-6$
22	-29.923	-0.041	$-1.747e-5$	$2.805e-5$
23	-29.902	-0.034	$-1.699e-5$	$2.607e-5$
24	-30.146	-0.022	$1.785e-5$	$-4.174e-6$
25	-29.080	-0.011	$-5.020e-5$	$3.698e-6$

Continue on next page...

<sup>2</sup>There is no solution for CFHT chip 8 as there are too few stars in that region in the INT data for calibration.

Table A.3 – Continued from previous page

chip	$Z$	$C$	$A_1$	$A_2$
26	-29.125	-0.083	$-2.082e-5$	$-4.771e-5$
27	-29.630	-0.009	$-6.141e-5$	$1.540e-5$
28	-29.488	-0.019	$-7.698e-5$	$-4.148e-5$
29	-29.878	-0.039	$2.227e-5$	$-4.705e-5$
30	-29.969	-0.024	$1.251e-5$	$-1.239e-5$
31	-29.472	-0.014	$-4.359e-5$	$1.617e-5$
32	-29.836	-0.028	$-9.852e-6$	$4.171e-5$
33	-29.913	-0.017	$-2.361e-6$	$3.894e-5$
34	-29.328	0.005	$-3.788e-5$	$1.705e-5$
35	-29.582	-0.028	$3.337e-6$	$-1.427e-5$
<hr/>				
i'				
<hr/>				
0	-30.098	-0.061	$2.726e-6$	$5.277e-6$
1	-30.583	-0.062	$-1.831e-5$	$3.818e-5$
2	-30.717	-0.080	$-8.250e-6$	$4.375e-5$
3	-30.791	-0.092	$1.953e-5$	$3.836e-5$
4	-30.106	-0.070	$-1.758e-6$	$7.302e-6$
5	-30.119	-0.074	$-1.170e-5$	$1.397e-5$
6	-31.328	-0.097	$4.463e-5$	$4.102e-5$
7	-35.213	-0.034	$2.333e-4$	$8.771e-5$
8 <sup>3</sup>	–	–	–	–
9	-30.046	-0.028	$-5.094e-5$	$4.181e-5$
10	-29.658	-0.071	$-4.371e-5$	$-1.473e-5$
11	-29.852	-0.077	$-7.672e-6$	$-7.916e-6$
12	-30.246	-0.081	$2.195e-5$	$2.769e-6$
13	-29.945	-0.072	$-1.696e-5$	$1.213e-5$
14	-29.123	-0.088	$-3.450e-5$	$-2.829e-5$
15	-30.060	-0.067	$1.905e-5$	$-1.644e-5$
16	-30.019	-0.048	$-7.689e-6$	$9.734e-6$
17	-30.526	-0.085	$1.704e-5$	$1.756e-5$
18	-29.611	-0.028	$-8.737e-5$	$9.748e-7$
19	-29.163	-0.045	$-1.437e-4$	$-3.034e-5$
20	-29.660	-0.080	$-3.970e-5$	$-1.475e-5$

Continue on next page...

<sup>3</sup>There is no solution for CFHT chip 8 as there are too few stars in that region in the INT data for calibration.

Table A.3 – Continued from previous page

chip	$Z$	$C$	$A_1$	$A_2$
21	-30.214	-0.073	$7.239e - 5$	$-4.086e - 5$
22	-29.731	-0.100	$-2.794e - 5$	$5.699e - 6$
23	-29.933	-0.086	$-1.057e - 5$	$7.276e - 6$
24	-29.922	-0.066	$-1.148e - 6$	$-1.231e - 5$
25	-30.015	-0.072	$2.093e - 5$	$-3.398e - 5$
26	-33.833	-0.108	$2.313e - 4$	$-3.864e - 5$
27	-29.684	-0.020	$-7.320e - 5$	$-2.785e - 6$
28	-29.704	-0.060	$-7.255e - 5$	$5.786e - 6$
29	-30.145	-0.107	$4.388e - 5$	$-1.360e - 5$
30	-29.997	-0.085	$1.016e - 5$	$-1.890e - 5$
31	-29.750	-0.073	$-2.474e - 5$	$1.253e - 5$
32	-29.830	-0.062	$-1.755e - 5$	$1.564e - 5$
33	-30.174	-0.067	$1.008e - 5$	$1.996e - 5$
34	-29.281	-0.045	$-1.858e - 5$	$-1.032e - 4$
35	-29.065	-0.069	$-3.254e - 5$	$2.084e - 5$

Table A.4 shows the results of the density, completeness and completeness errors, fitting functions and its parameters. The exponential function is:  $f(x) = ae^{(x/b)} + c$ , when presents the lowest  $\chi^2$  sets the number 2 as best fit, and the polynomial function is:  $ax^4 + bx^3 + cx^2 + dx + e$ , when presents the lowest  $\chi^2$  sets the number 4 as best fit.

Table A.4: AST results for  $g$ ,  $r$  and  $i$  filters. The best is 2 when the goodness of fit was from the exponential function,  $f(x) = ae^{(x/b)} + c$ , or 4 from the polynomial function,  $ax^4 + bx^3 + cx^2 + dx + e$ .

img	density	mag <sub>50</sub>	emag(-)	emag(+)	best fit	func <sub>50</sub>	exponential function					polynomial function				
							$a_{efac}$	$b_{efac}$	$c_{efac}$	$a_{pfac}$	$b_{pfac}$	$c_{pfac}$	$d_{pfac}$	$e_{pfac}$		
1g	0.0028	18.4	0.1	0.39	2	0.013	4.68	0.312	-0.0026	0.00039	-0.023	-0.002	-4.903	17.643		
2g	0.0033	18.5	0.11	0.38	4	0.017	7.127	0.293	-0.0024	4.8009	-0.002	-0.002	-0.372	1.1136		
3g	0.0033	18.5	0.07	0.42	2	0.013	4.288	0.188	-0.0019	0.00024	-0.013	-0.001	-2.653	9.1158		
4g	0.0023	18.4	0.08	0.08	2	0.007	4.72	0.281	-0.0019	0.00024	-0.014	-0.001	-2.737	9.4056		
5g	0.0026	18.5	0.37	0.12	2	0.013	2.294	0.298	-0.0025	0.00019	-0.011	-0.002	-2.222	7.7093		
6g	0.0034	18.6	0.36	0.14	4	0.021	9.711	0.377	-0.0036	2.40628	-0.0	-0.003	-0.03	-0.163		
7g	0.0047	18.8	0.41	0.08	2	0.037	3.0	0.246	-0.0032	6.60949	-0.003	-0.003	-0.568	1.7921		
8g	0.0043	18.5	0.1	0.39	2	0.023	2.985	0.474	-0.0035	0.00018	-0.01	-0.003	-1.961	6.6647		
9g	0.0036	18.4	0.05	0.44	2	0.009	2.642	0.299	-0.0027	0.00014	-0.008	-0.002	-1.607	5.5673		
10g	0.0045	18.5	0.08	0.41	2	0.013	6.799	0.304	-0.0025	0.00017	-0.009	-0.002	-1.815	6.1788		
11g	0.0036	18.6	0.1	0.39	2	0.014	3.222	0.29	-0.0028	0.00027	-0.015	-0.002	-3.046	10.553		
12g	0.0036	18.5	0.05	0.44	2	0.02	2.905	0.323	-0.0013	0.00046	-0.027	-0.001	-6.016	21.96		
13g	0.003	18.2	0.16	0.16	2	0.003	2.534	0.218	0.00023	0.00039	-0.024	0.0002	-5.475	20.468		
14g	0.004	18.3	0.13	0.13	2	0.004	2.471	0.218	8.01068	0.00026	-0.015	8.0106	-3.063	10.63		
15g	0.0045	18.2	0.17	0.17	2	0.001	3.41	0.177	0.00011	0.00013	-0.007	0.0001	-1.549	5.4397		
16g	0.0075	18.5	0.13	0.13	2	0.009	5.222	0.199	0.0006	0.00016	-0.009	0.0006	-1.91	6.6199		
17g	0.0111	18.3	0.14	0.14	2	0.005	1.236	0.236	0.00054	0.0002	-0.011	0.0005	-2.351	8.2402		

Continue on next page...

Table A.4 – Continued from previous page

img	density	mag <sub>50</sub>	emag(–)	emag(+)	best fit	func <sub>50</sub>	exponential function					polynomial function				
							a <sub>efac</sub>	b <sub>efac</sub>	c <sub>efac</sub>	a <sub>pfac</sub>	b <sub>pfac</sub>	c <sub>pfac</sub>	d <sub>pfac</sub>	e <sub>pfac</sub>		
18g	0.0184	18.5	0.34	0.15	2	0.018	1.327	0.332	0.00106	0.00043	-0.024	0.0010	-4.904	16.979		
19g	0.0166	18.7	0.37	0.12	2	0.026	1.821	0.207	0.00132	0.00025	-0.014	0.0013	-2.948	10.27		
20g	0.0134	18.5	0.07	0.42	2	0.011	5.248	0.273	-1.6654	0.00039	-0.023	-1.665	-4.672	16.387		
21g	0.0143	18.7	0.38	0.11	2	0.029	3.565	0.193	0.00108	0.00018	-0.01	0.0010	-2.062	7.135		
22g	0.0092	18.5	0.09	0.4	2	0.012	8.641	0.257	1.57937	0.00033	-0.019	1.5793	-3.873	13.508		
23g	0.0034	18.5	0.1	0.39	2	0.024	8.318	0.328	-0.001	0.00055	-0.032	-0.001	-6.911	24.75		
24g	0.0066	18.7	0.36	0.13	2	0.024	2.378	0.325	0.00062	0.00015	-0.008	0.0006	-1.781	6.2974		
25g	0.0097	18.9	0.0	0.0	2	0.075	1.669	0.297	0.00042	0.00039	-0.022	0.0004	-4.55	15.878		
26g	0.0195	18.6	0.36	0.13	2	0.02	4.442	0.292	0.00114	0.00041	-0.024	0.0011	-4.913	17.301		
27g	0.0435	18.6	0.35	0.14	2	0.023	2.346	0.309	0.00064	0.00079	-0.046	0.0006	-9.668	34.309		
28g	0.0714	18.5	0.36	0.13	2	0.019	6.132	0.248	0.00264	0.00057	-0.032	0.0026	-6.545	22.716		
29g	0.1007	18.3	0.05	0.44	2	0.015	1.108	0.241	0.00647	0.00095	-0.055	0.0064	-11.43	40.347		
30g	0.0828	18.6	0.39	0.1	2	0.026	5.626	0.233	0.00496	0.0011	-0.064	0.0049	-13.44	47.79		
31g	0.049	18.6	0.37	0.12	2	0.018	9.914	0.229	0.00308	0.00108	-0.062	0.0030	-12.8	44.88		
32g	0.0369	18.5	0.36	0.14	2	0.009	1.236	0.183	0.0022	0.0009	-0.052	0.0022	-10.95	38.841		
33g	0.0317	18.8	0.43	0.06	2	0.058	2.534	0.298	0.00125	0.00054	-0.031	0.0012	-6.393	22.396		
34g	0.0054	18.6	0.01	0.48	2	0.014	2.293	0.279	-0.0001	0.00044	-0.026	-0.000	-5.578	20.069		
35g	0.0136	18.7	0.06	0.06	2	0.019	2.907	0.247	7.46989	0.00033	-0.019	7.4698	-4.107	14.676		
36g	0.0362	18.7	0.38	0.11	2	0.026	4.988	0.215	0.00213	0.00175	-0.106	0.0021	-23.93	88.896		

Continue on next page...

Table A.4 – Continued from previous page

img	density	mag <sub>50</sub>	emag(–)	emag(+)	best fit	func <sub>50</sub>	exponential function					polynomial function				
							a <sub>efac</sub>	b <sub>efac</sub>	c <sub>efac</sub>	a <sub>pfac</sub>	b <sub>pfac</sub>	c <sub>pfac</sub>	d <sub>pfac</sub>	e <sub>pfac</sub>		
37g	0.091	18.6	0.39	0.1	2	0.034	1.997	0.297	0.00718	0.00146	-0.088	0.0071	-19.94	73.882		
38g	0.1527	18.4	0.04	0.45	2	0.019	9.624	0.217	0.01381	0.01054	-0.694	0.0138	-186.6	761.98		
39g	0.2242	18.3	0.03	0.46	2	0.036	3.058	0.286	0.01877	0.00971	-0.633	0.0187	-167.4	677.19		
40g	0.3312	18.3	0.0	0.49	4	0.076	9.725	1.009	0.0122	0.00147	-0.093	0.0122	-23.18	90.86		
41g	0.2593	18.2	0.04	0.45	2	0.035	4.741	0.335	0.01833	0.00445	-0.28	0.0183	-68.5	265.87		
42g	0.1912	18.4	0.02	0.47	2	0.046	5.648	0.402	0.011	0.0097	-0.639	0.011	-172.1	704.04		
43g	0.0867	18.4	0.06	0.43	2	0.016	1.321	0.236	0.006	0.00336	-0.209	0.006	-49.76	190.05		
44g	0.0635	18.7	0.41	0.08	2	0.038	4.497	0.232	0.00313	0.0006	-0.035	0.0031	-7.386	26.312		
45g	0.0147	18.8	0.41	0.08	2	0.04	1.164	0.266	-0.0002	0.00064	-0.037	-0.000	-7.575	26.623		
46g	0.0555	18.5	0.07	0.42	2	0.014	5.057	0.204	0.0038	0.00066	-0.039	0.0038	-8.414	30.391		
47g	0.1114	18.5	0.03	0.46	2	0.022	4.89	0.262	0.00627	0.00327	-0.207	0.0062	-51.24	200.19		
48g	0.2177	18.4	0.04	0.45	2	0.032	8.472	0.255	0.01694	0.00817	-0.532	0.0169	-139.5	562.69		
49g	0.4294	18.2	0.37	0.12	4	0.097	5.082	1.268	0.0109	0.00137	-0.086	0.0109	-21.49	84.197		
50g	0.6818	17.7	0.31	0.18	2	0.132	1.818	0.716	0.0344	0.00696	-0.437	0.0344	-107.3	418.74		
51g	0.7115	17.8	0.01	0.48	2	0.15	2.886	0.727	0.03094	0.00749	-0.472	0.0309	-116.5	456.08		
52g	0.522	18.1	0.4	0.09	4	0.122	3.384	1.203	0.0134	0.00138	-0.085	0.0134	-20.03	76.483		
53g	0.3717	17.9	0.32	0.17	4	0.07	2.318	1.211	0.01458	0.00158	-0.1	0.0145	-24.95	98.083		
54g	0.1321	18.3	0.05	0.44	2	0.03	3.358	0.346	0.00374	0.0027	-0.161	0.0037	-34.93	126.97		
55g	0.0868	18.5	0.0	0.49	2	0.049	8.65	0.301	0.00433	0.00174	-0.103	0.0043	-22.56	82.173		

Continue on next page...

Table A.4 – Continued from previous page

img	density	mag <sub>50</sub>	emag(-)	emag(+)	best fit	func <sub>50</sub>	exponential function					polynomial function				
							a <sub>efac</sub>	b <sub>efac</sub>	c <sub>efac</sub>	a <sub>pfac</sub>	b <sub>pfac</sub>	c <sub>pfac</sub>	d <sub>pfac</sub>	e <sub>pfac</sub>		
56g	0.0429	18.6	0.05	0.44	2	0.023	2.61	0.261	0.00067	0.00142	-0.086	0.0006	-19.35	71.728		
57g	0.1369	18.4	0.03	0.46	2	0.02	8.24	0.24	0.00732	0.00196	-0.12	0.0073	-27.82	104.69		
58g	0.2762	18.2	0.05	0.45	2	0.043	9.638	0.369	0.01867	0.0043	-0.269	0.0186	-64.94	250.18		
59g	0.45	18.1	0.05	0.44	4	0.09	1.471	0.898	0.01732	0.00382	-0.247	0.0173	-64.92	262.0		
60g	0.7858	17.8	0.39	0.1	4	0.166	1.284	1.276	0.01853	0.00152	-0.091	0.0185	-20.52	76.574		
61g	1.0244	17.3	0.07	0.42	4	0.185	2.657	0.968	0.03114	0.00383	-0.232	0.0311	-53.47	202.12		
62g	0.8794	17.4	0.3	0.19	4	0.147	1.62	1.1	0.02981	0.00109	-0.063	0.0298	-13.44	48.729		
63g	0.6613	17.8	0.06	0.43	4	0.119	5.667	0.753	0.02945	0.0051	-0.319	0.0294	-77.48	300.5		
64g	0.3732	18.2	0.37	0.12	2	0.066	2.466	0.457	0.02558	0.00438	-0.28	0.0255	-71.56	284.34		
65g	0.1767	18.4	0.37	0.12	2	0.03	1.543	0.284	0.0119	0.00911	-0.592	0.0119	-155.0	624.31		
66g	0.0656	18.7	0.41	0.08	2	0.055	8.5	0.256	0.00407	0.00103	-0.06	0.0040	-12.84	46.019		
67g	0.0626	18.7	0.04	0.45	2	0.034	6.453	0.256	0.00083	0.00418	-0.268	0.0008	-68.13	269.94		
68g	0.1944	18.4	0.35	0.14	2	0.025	5.452	0.254	0.01167	0.00258	-0.162	0.0116	-39.36	152.23		
69g	0.309	18.3	0.37	0.12	2	0.049	9.101	0.428	0.0194	0.00346	-0.215	0.0194	-51.35	196.79		
70g	0.4991	18.0	0.02	0.47	2	0.085	1.24	0.47	0.03063	0.01067	-0.695	0.0306	-183.4	742.92		
71g	0.7607	17.8	0.06	0.43	4	0.153	2.566	1.628	0.00906	0.00071	-0.042	0.0090	-9.491	35.274		
72g	0.7922	17.9	0.38	0.11	4	0.184	1.523	1.286	0.01351	0.00195	-0.119	0.0135	-27.56	104.58		
73g	0.5997	18.2	0.39	0.1	4	0.13	6.321	1.262	0.01856	-0.0001	0.0122	0.0185	4.6727	-21.38		
74g	0.3612	18.4	0.39	0.1	2	0.075	5.599	0.421	0.02504	0.00829	-0.541	0.0250	-142.6	577.08		

Continue on next page...

Table A.4 – Continued from previous page

img	density	mag <sub>50</sub>	emag(–)	emag(+)	best fit	func <sub>50</sub>	exponential function					polynomial function				
							a <sub>efac</sub>	b <sub>efac</sub>	c <sub>efac</sub>	a <sub>pfac</sub>	b <sub>pfac</sub>	c <sub>pfac</sub>	d <sub>pfac</sub>	e <sub>pfac</sub>		
75g	0.2185	18.6	0.4	0.09	2	0.062	4.047	0.35	0.01115	0.00109	-0.065	0.0111	-14.26	52.057		
76g	0.1034	18.5	0.06	0.43	2	0.027	6.313	0.291	0.00376	0.00133	-0.077	0.0037	-15.72	55.026		
77g	0.0246	18.8	0.38	0.11	2	0.037	3.956	0.227	0.0013	0.00073	-0.042	0.0013	-8.804	31.093		
78g	0.0702	18.7	0.39	0.1	2	0.024	1.371	0.237	0.00419	0.0037	-0.231	0.0041	-55.61	213.66		
79g	0.1501	18.4	0.05	0.44	2	0.023	7.794	0.264	0.01009	0.00872	-0.575	0.0100	-155.1	634.39		
80g	0.2556	18.4	0.37	0.12	2	0.049	9.265	0.34	0.01808	0.00848	-0.552	0.0180	-144.8	583.6		
81g	0.3685	18.4	0.4	0.09	4	0.09	2.669	1.229	0.00982	0.00104	-0.065	0.0098	-16.01	62.29		
82g	0.4888	18.1	0.02	0.47	4	0.098	1.407	1.35	0.00745	0.00105	-0.065	0.0074	-15.79	61.135		
83g	0.4185	18.2	0.07	0.42	2	0.068	3.773	0.523	0.02032	0.00618	-0.39	0.0203	-96.63	377.52		
84g	0.2752	18.7	0.41	0.08	2	0.071	7.95	0.328	0.01876	0.01168	-0.769	0.0187	-206.9	844.81		
85g	0.197	18.7	0.0	0.49	2	0.047	1.984	0.269	0.01438	0.0113	-0.747	0.0143	-202.6	830.55		
86g	0.103	18.7	0.06	0.43	2	0.039	1.483	0.297	0.00587	0.00102	-0.061	0.0058	-13.68	50.414		
87g	0.0364	18.8	0.03	0.03	2	0.026	2.073	0.27	0.00052	0.00068	-0.04	0.0005	-8.606	30.939		
88g	0.0114	18.8	0.01	0.48	2	0.027	1.465	0.269	0.00107	0.00038	-0.022	0.0010	-4.473	15.598		
89g	0.0309	18.8	0.01	0.48	2	0.045	2.557	0.3	0.00033	0.00079	-0.047	0.0003	-10.21	37.074		
90g	0.083	18.9	0.45	0.04	2	0.055	5.015	0.227	0.00552	0.0018	-0.109	0.0055	-24.67	91.687		
91g	0.1763	18.6	0.39	0.1	2	0.034	1.373	0.266	0.01069	0.00615	-0.391	0.0106	-97.94	384.75		
92g	0.2018	18.5	0.01	0.48	2	0.046	1.825	0.376	0.00933	0.00299	-0.184	0.0093	-43.0	162.52		
93g	0.216	18.5	0.05	0.44	2	0.045	1.281	0.329	0.01267	0.00762	-0.492	0.0126	-127.1	508.15		

Continue on next page...

Table A.4 – Continued from previous page

img	density	mag <sub>50</sub>	emag(-)	emag(+)	best fit	func <sub>50</sub>	exponential function				polynomial function			
							a <sub>efac</sub>	b <sub>efac</sub>	c <sub>efac</sub>	a <sub>pfac</sub>	b <sub>pfac</sub>	c <sub>pfac</sub>	d <sub>pfac</sub>	e <sub>pfac</sub>
94g	0.2212	18.5	0.06	0.43	2	0.038	7.113	0.34	0.01251	0.00544	-0.348	0.0125	-87.9	347.02
95g	0.1326	18.9	0.41	0.08	2	0.058	7.024	0.304	0.0069	0.00861	-0.567	0.0069	-152.8	624.4
96g	0.0736	18.7	0.06	0.43	2	0.024	5.932	0.283	0.00396	0.00452	-0.288	0.0039	-72.19	283.22
97g	0.0293	18.6	0.07	0.07	2	0.015	1.159	0.287	0.0017	0.00065	-0.038	0.0017	-8.165	29.29
98g	0.0125	18.7	0.09	0.09	2	0.017	1.311	0.219	0.00048	0.00044	-0.026	0.0004	-5.423	19.281
99g	0.0066	18.6	0.33	0.16	2	0.018	1.462	0.349	-5.7172	0.00026	-0.015	-5.717	-3.003	10.457
100g	0.01	18.7	0.35	0.14	2	0.019	1.22	0.278	0.00046	0.00022	-0.012	0.0004	-2.59	9.0882
101g	0.0193	18.5	0.13	0.13	2	0.012	7.506	0.235	0.00113	0.00027	-0.015	0.0011	-3.304	11.744
102g	0.0362	18.7	0.36	0.13	2	0.022	1.124	0.333	0.00116	0.00032	-0.018	0.0011	-3.828	13.42
103g	0.046	18.7	0.04	0.04	2	0.023	8.081	0.286	0.00138	0.0009	-0.054	0.0013	-12.1	44.597
104g	0.0475	18.9	0.02	0.47	2	0.042	1.63	0.232	0.00287	0.00107	-0.064	0.0028	-14.2	52.049
105g	0.0325	18.7	0.35	0.14	2	0.012	3.316	0.234	0.00127	0.00034	-0.02	0.0012	-4.075	14.265
106g	0.0222	18.9	0.01	0.01	2	0.034	6.112	0.23	0.00094	0.00045	-0.026	0.0009	-5.87	21.412
107g	0.0136	18.9	0.02	0.02	2	0.034	1.839	0.226	0.00054	0.00039	-0.023	0.0005	-4.899	17.62
108g	0.0095	18.8	0.02	0.47	2	0.03	3.805	0.342	0.00033	0.0004	-0.023	0.0003	-4.828	16.963
109g	0.0047	18.5	0.16	0.16	2	0.008	1.989	0.232	3.89708	0.00017	-0.01	3.8970	-2.069	7.3556
110g	0.0036	18.7	0.07	0.42	2	0.021	1.764	0.279	0.00028	0.00035	-0.02	0.0002	-4.27	15.106
111g	0.0054	18.8	0.4	0.09	2	0.047	1.42	0.276	-0.0007	0.00011	-0.005	-0.000	-0.902	2.6618
112g	0.006	18.6	0.34	0.15	2	0.011	6.405	0.191	0.0007	0.00017	-0.009	0.0007	-1.928	6.6359

Continue on next page...

Table A.4 – Continued from previous page

img	density	mag <sub>50</sub>	emag(–)	emag(+)	best fit	func <sub>50</sub>	exponential function					polynomial function				
							a <sub>efac</sub>	b <sub>efac</sub>	c <sub>efac</sub>	a <sub>pfac</sub>	b <sub>pfac</sub>	c <sub>pfac</sub>	d <sub>pfac</sub>	e <sub>pfac</sub>		
113g	0.0084	18.8	0.36	0.13	2	0.039	2.639	0.279	-0.0011	0.0001	-0.005	-0.001	-0.72	1.8654		
114g	0.0093	18.7	0.33	0.16	2	0.017	6.375	0.25	-0.0002	0.0003	-0.017	-0.000	-3.563	12.499		
115g	0.0104	18.7	0.32	0.17	2	0.017	2.866	0.24	-0.0005	8.55729	-0.004	-0.000	-0.65	1.8324		
116g	0.0081	18.8	0.04	0.45	2	0.023	1.673	0.246	0.00086	0.00038	-0.022	0.0008	-4.513	15.782		
117g	0.0055	18.9	0.35	0.14	2	0.029	2.678	0.371	-0.0004	0.00017	-0.009	-0.000	-1.829	6.1632		
118g	0.0038	18.9	0.34	0.15	2	0.03	3.463	0.264	2.85373	0.00027	-0.015	2.8537	-3.294	11.655		
119g	0.0035	18.8	0.08	0.41	2	0.018	7.18	0.237	0.00028	0.0002	-0.011	0.0002	-2.481	8.8123		
120g	0.0034	18.7	0.06	0.43	2	0.021	1.729	0.213	0.00037	0.00037	-0.021	0.0003	-4.513	16.028		
121g	0.0026	18.6	0.05	0.44	2	0.014	2.55	0.169	0.00047	0.00036	-0.021	0.0004	-4.35	15.31		
1r	0.0024	17.7	0.13	0.36	4	0.008	2.082	0.41	-0.0029	-3.4124	0.0022	-0.002	0.5524	-2.07		
2r	0.0036	17.9	0.03	0.46	2	0.009	3.734	0.17	-0.0025	0.00011	-0.006	-0.002	-1.099	3.6351		
3r	0.003	17.9	0.03	0.46	2	0.012	2.151	0.258	-0.0072	6.46772	-0.002	-0.007	-0.33	0.7971		
4r	0.0024	18.1	0.37	0.12	2	0.031	1.16	0.275	-0.0063	0.0001	-0.005	-0.006	-1.002	3.3611		
5r	0.0035	18.0	0.34	0.16	2	0.018	4.193	0.281	-0.0045	0.00033	-0.019	-0.004	-3.809	13.392		
6r	0.0046	17.9	0.13	0.36	2	0.003	1.088	0.169	-0.003	0.00023	-0.012	-0.003	-2.362	7.9159		
7r	0.0055	17.9	0.11	0.38	2	0.01	4.155	0.239	-0.003	0.00023	-0.012	-0.003	-2.33	7.7919		
8r	0.0063	17.5	0.21	0.21	4	0.005	3.407	0.469	-0.0032	-3.5236	0.0022	-0.003	0.5428	-2.009		
9r	0.0049	17.9	0.33	0.16	2	0.012	3.21	0.29	-0.0059	0.00027	-0.015	-0.005	-3.062	10.65		
10r	0.005	17.9	0.12	0.37	2	0.014	1.565	0.216	-0.0021	0.00022	-0.012	-0.002	-2.282	7.6484		

Continue on next page...

Table A.4 – Continued from previous page

img	density	mag <sub>50</sub>	emag(-)	emag(+)	best fit	func <sub>50</sub>	exponential function					polynomial function				
							a <sub>efac</sub>	b <sub>efac</sub>	c <sub>efac</sub>	a <sub>pfac</sub>	b <sub>pfac</sub>	c <sub>pfac</sub>	d <sub>pfac</sub>	e <sub>pfac</sub>		
11r	0.0031	17.8	0.29	0.2	2	0.006	9.484	0.198	-0.0011	0.00016	-0.008	-0.001	-1.627	5.4604		
12r	0.0032	17.9	0.1	0.39	2	0.012	1.459	0.2	0.00026	0.0002	-0.011	0.0002	-2.188	7.4654		
13r	0.004	17.9	0.09	0.4	2	0.015	4.305	0.293	0.00011	0.00025	-0.014	0.0001	-2.784	9.5371		
14r	0.0043	18.0	0.08	0.41	2	0.017	1.211	0.267	-0.0038	0.00028	-0.016	-0.003	-3.258	11.445		
15r	0.0067	17.9	0.3	0.19	2	0.005	1.204	0.205	-0.0034	0.00063	-0.036	-0.003	-7.618	27.144		
16r	0.0125	18.1	0.33	0.16	2	0.026	1.362	0.195	0.00053	0.00064	-0.037	0.0005	-7.734	27.527		
17r	0.0191	18.1	0.08	0.41	2	0.029	4.565	0.219	0.00084	0.00119	-0.07	0.0008	-15.09	54.654		
18r	0.0278	18.1	0.01	0.48	2	0.016	2.997	0.148	0.00237	0.00183	-0.107	0.0023	-22.25	79.328		
19r	0.0283	18.0	0.08	0.41	2	0.013	3.281	0.154	0.0026	0.00067	-0.039	0.0026	-7.956	28.049		
20r	0.0217	17.9	0.31	0.18	2	0.009	5.585	0.226	-0.0008	0.00056	-0.032	-0.000	-6.583	23.149		
21r	0.0217	17.9	0.3	0.19	2	0.008	8.56	0.172	0.00141	0.00073	-0.041	0.0014	-8.164	28.233		
22r	0.0119	17.8	0.31	0.18	2	0.005	1.594	0.122	0.00105	0.00043	-0.024	0.0010	-4.79	16.543		
23r	0.0033	18.0	0.15	0.34	2	0.017	1.691	0.186	-0.0001	0.00051	-0.028	-0.000	-5.574	19.118		
24r	0.0099	18.0	0.15	0.34	2	0.015	3.148	0.202	0.00139	0.00036	-0.02	0.0013	-4.036	13.86		
25r	0.0119	18.0	0.16	0.33	2	0.003	2.782	0.188	-0.0042	0.00021	-0.011	-0.004	-2.245	7.7117		
26r	0.0263	18.1	0.01	0.48	2	0.015	4.781	0.176	-0.0015	0.00082	-0.048	-0.001	-10.34	37.562		
27r	0.0623	18.1	0.01	0.48	2	0.029	1.314	0.21	0.00302	0.00091	-0.053	0.0030	-11.17	40.028		
28r	0.0952	18.1	0.37	0.12	2	0.031	4.343	0.197	0.00737	0.00645	-0.398	0.0073	-93.78	357.45		
29r	0.1208	18.0	0.05	0.44	2	0.04	1.983	0.229	0.00834	0.00325	-0.195	0.0083	-43.22	159.43		

Continue on next page...

Table A.4 – Continued from previous page

img	density	mag <sub>50</sub>	emag(−)	emag(+)	best fit	func <sub>50</sub>	exponential function					polynomial function				
							a <sub>efac</sub>	b <sub>efac</sub>	c <sub>efac</sub>	a <sub>pfac</sub>	b <sub>pfac</sub>	c <sub>pfac</sub>	d <sub>pfac</sub>	e <sub>pfac</sub>		
30r	0.1018	18.1	0.36	0.14	2	0.033	1.247	0.199	0.00685	0.00275	−0.166	0.0068	−37.05	137.26		
31r	0.0627	18.1	0.36	0.13	2	0.021	2.016	0.174	0.00046	0.0025	−0.15	0.0004	−33.32	123.1		
32r	0.0584	18.1	0.04	0.45	2	0.014	3.82	0.1	0.00762	0.0033	−0.2	0.0076	−45.41	169.59		
33r	0.04	17.9	0.11	0.11	2	0.015	5.692	0.175	0.00443	0.00125	−0.071	0.0044	−14.25	49.604		
34r	0.0068	17.8	0.28	0.21	2	0.006	1.742	0.244	0.00029	0.00062	−0.036	0.0002	−7.547	26.847		
35r	0.0225	18.0	0.09	0.4	2	0.015	1.147	0.181	0.00144	0.00044	−0.025	0.0014	−4.985	17.31		
36r	0.0454	18.1	0.05	0.44	2	0.03	9.588	0.204	−0.002	0.002	−0.118	−0.002	−25.37	92.04		
37r	0.1067	18.2	0.37	0.12	2	0.052	2.586	0.252	0.00613	0.00713	−0.444	0.0061	−106.7	411.34		
38r	0.1762	18.1	0.37	0.12	2	0.057	1.048	0.227	0.01203	0.00883	−0.559	0.0120	−139.0	545.68		
39r	0.2538	18.0	0.04	0.45	2	0.055	4.392	0.279	0.01639	0.01362	−0.862	0.0163	−214.2	840.55		
40r	0.3514	17.9	0.02	0.47	2	0.067	6.897	0.312	0.02498	0.00781	−0.489	0.0249	−118.9	461.4		
41r	0.2936	17.8	0.05	0.44	2	0.041	2.848	0.276	0.0198	0.00453	−0.281	0.0198	−66.71	255.75		
42r	0.1819	17.9	0.07	0.42	2	0.044	2.266	0.319	0.00296	0.02459	−1.594	0.0029	−416.5	1677.9		
43r	0.1142	18.1	0.37	0.12	2	0.031	3.594	0.164	0.00861	0.00819	−0.52	0.0086	−130.4	514.43		
44r	0.0675	17.9	0.1	0.39	2	0.022	5.591	0.179	0.00569	0.00702	−0.441	0.0056	−107.9	420.52		
45r	0.0222	18.1	0.03	0.46	2	0.027	1.109	0.209	8.62741	0.00107	−0.061	8.6274	−12.24	42.626		
46r	0.0783	18.1	0.03	0.46	2	0.022	3.586	0.171	0.00453	0.00273	−0.164	0.0045	−36.87	136.92		
47r	0.1156	18.1	0.34	0.15	2	0.046	4.07	0.218	0.00413	0.02425	−1.571	0.0041	−409.6	1648.3		
48r	0.2288	18.1	0.02	0.47	2	0.065	1.28	0.249	0.01472	0.01649	−1.05	0.0147	−264.2	1043.4		

Continue on next page...

Table A.4 – Continued from previous page

img	density	mag <sub>50</sub>	emag(−)	emag(+)	best fit	func <sub>50</sub>	exponential function					polynomial function				
							a <sub>efac</sub>	b <sub>efac</sub>	c <sub>efac</sub>	a <sub>pfac</sub>	b <sub>pfac</sub>	c <sub>pfac</sub>	d <sub>pfac</sub>	e <sub>pfac</sub>		
49r	0.5228	17.7	0.36	0.13	2	0.079	1.727	0.376	0.03441	0.01183	-0.748	0.0344	-185.4	727.16		
50r	0.8264	17.4	0.35	0.14	4	0.137	1.774	1.108	0.02563	0.00205	-0.123	0.0256	-28.01	105.12		
51r	0.8657	17.2	0.28	0.21	4	0.133	2.703	1.328	0.01998	0.00162	-0.099	0.0199	-23.44	90.076		
52r	0.6322	17.7	0.41	0.08	2	0.117	1.429	0.409	0.03535	0.01139	-0.702	0.0353	-165.8	633.65		
53r	0.3585	17.9	0.42	0.07	2	0.096	3.302	0.38	0.01416	0.01701	-1.077	0.0141	-268.0	1053.0		
54r	0.1634	18.1	0.39	0.1	2	0.055	4.883	0.187	0.01183	0.0041	-0.249	0.0118	-56.64	211.93		
55r	0.0818	18.0	0.37	0.12	2	0.05	2.34	0.216	0.00941	0.00772	-0.488	0.0094	-120.8	473.54		
56r	0.0506	18.0	0.31	0.18	2	0.015	1.46	0.181	0.00306	0.00157	-0.094	0.0030	-20.8	76.645		
57r	0.153	18.0	0.05	0.44	2	0.038	2.045	0.25	0.00805	0.00718	-0.438	0.0080	-100.7	379.2		
58r	0.3164	18.1	0.4	0.1	2	0.064	2.458	0.186	0.01511	0.01556	-1.001	0.0151	-257.5	1029.1		
59r	0.4201	18.0	0.01	0.48	2	0.058	2.858	0.242	0.01685	0.01487	-0.96	0.0168	-248.7	998.08		
60r	0.9967	17.3	0.37	0.12	2	0.156	6.244	0.614	0.04875	0.012	-0.741	0.0487	-175.8	674.44		
61r	1.266	16.9	0.0	0.49	4	0.195	8.011	0.882	0.0374	0.00579	-0.343	0.0374	-74.81	275.31		
62r	1.0993	17.1	0.04	0.45	4	0.175	1.128	1.206	0.0254	0.00724	-0.444	0.0254	-104.4	399.33		
63r	0.7606	17.4	0.33	0.16	4	0.134	2.66	1.141	0.02059	0.00115	-0.067	0.0205	-14.0	50.138		
64r	0.3555	17.8	0.38	0.11	4	0.074	3.28	0.746	0.00857	0.00502	-0.318	0.0085	-79.06	310.42		
65r	0.183	18.0	0.03	0.46	2	0.053	8.098	0.246	0.01364	0.02578	-1.67	0.0136	-435.9	1755.5		
66r	0.0607	17.9	0.14	0.35	2	0.02	1.822	0.21	0.00498	0.00559	-0.337	0.0049	-75.25	278.95		
67r	0.0687	17.9	0.12	0.37	2	0.015	1.728	0.186	0.00348	0.00108	-0.063	0.0034	-13.39	48.107		

Continue on next page...

Table A.4 – Continued from previous page

img	density	mag <sub>50</sub>	emag(-)	emag(+)	best fit	func <sub>50</sub>	exponential function					polynomial function				
							a <sub>efac</sub>	b <sub>efac</sub>	c <sub>efac</sub>	a <sub>pfac</sub>	b <sub>pfac</sub>	c <sub>pfac</sub>	d <sub>pfac</sub>	e <sub>pfac</sub>		
68r	0.2027	17.9	0.05	0.44	2	0.034	8.561	0.232	0.01045	0.00346	-0.203	0.0104	-42.86	153.96		
69r	0.2687	18.1	0.0	0.49	2	0.077	1.205	0.264	0.01398	0.00379	-0.235	0.0139	-56.37	216.85		
70r	0.5214	17.7	0.36	0.13	4	0.099	2.299	0.897	0.01839	0.00351	-0.221	0.0183	-54.93	215.81		
71r	0.8846	17.4	0.0	0.49	2	0.149	3.281	0.654	0.04131	0.00778	-0.477	0.0413	-111.3	423.5		
72r	0.9546	17.4	0.36	0.13	4	0.176	3.978	1.349	0.01475	0.00252	-0.153	0.0147	-35.14	132.89		
73r	0.7219	17.3	0.05	0.45	4	0.098	3.099	0.609	0.03718	0.01053	-0.658	0.0371	-159.7	619.87		
74r	0.416	18.0	0.42	0.07	2	0.113	2.735	0.257	0.03363	0.01241	-0.791	0.0336	-199.5	790.11		
75r	0.1887	18.0	0.37	0.12	2	0.06	8.996	0.292	0.00426	0.01165	-0.735	0.0042	-181.6	710.21		
76r	0.1	18.1	0.35	0.15	2	0.056	8.403	0.255	0.00446	0.00337	-0.204	0.0044	-46.25	172.7		
77r	0.0245	18.1	0.05	0.44	2	0.022	6.736	0.165	0.00226	0.00095	-0.056	0.0022	-12.17	44.374		
78r	0.0723	17.9	0.08	0.41	2	0.021	2.992	0.229	0.00175	0.00201	-0.114	0.0017	-22.26	76.55		
79r	0.1605	18.0	0.03	0.46	2	0.036	3.096	0.23	0.01039	0.02972	-1.927	0.0103	-503.7	2029.7		
80r	0.218	18.1	0.4	0.1	2	0.048	1.029	0.209	0.00935	0.01274	-0.815	0.0093	-207.1	822.02		
81r	0.3594	17.8	0.03	0.46	2	0.04	1.362	0.226	0.02535	0.00672	-0.421	0.0253	-102.6	398.44		
82r	0.5036	17.6	0.34	0.15	2	0.071	4.646	0.424	0.02714	0.01091	-0.676	0.0271	-160.5	615.34		
83r	0.4282	18.0	0.42	0.07	2	0.103	8.017	0.339	0.02472	0.00937	-0.579	0.0247	-136.5	521.19		
84r	0.2925	17.9	0.05	0.44	2	0.049	4.16	0.289	0.01967	0.00709	-0.436	0.0196	-102.0	387.57		
85r	0.1887	18.1	0.02	0.47	2	0.066	1.573	0.249	0.01112	0.00792	-0.498	0.0111	-122.1	475.73		
86r	0.0808	18.2	0.37	0.12	2	0.068	4.932	0.231	-0.0016	0.00233	-0.138	-0.001	-30.19	110.44		

Continue on next page...

Table A.4 – Continued from previous page

img	density	mag <sub>50</sub>	emag(–)	emag(+)	best fit	func <sub>50</sub>	exponential function					polynomial function				
							a <sub>efac</sub>	b <sub>efac</sub>	c <sub>efac</sub>	a <sub>pfac</sub>	b <sub>pfac</sub>	c <sub>pfac</sub>	d <sub>pfac</sub>	e <sub>pfac</sub>		
87r	0.0389	18.0	0.14	0.35	2	0.017	2.725	0.201	0.00318	0.00194	-0.115	0.0031	-24.99	91.063		
88r	0.0108	18.0	0.12	0.37	2	0.02	6.617	0.208	0.00099	0.00105	-0.061	0.0009	-12.66	45.103		
89r	0.0297	18.0	0.36	0.13	2	0.03	1.863	0.159	0.003	0.00303	-0.186	0.003	-43.41	164.62		
90r	0.0843	18.1	0.34	0.15	2	0.029	1.172	0.173	0.00662	0.00622	-0.394	0.0066	-98.28	386.34		
91r	0.137	18.0	0.34	0.15	2	0.032	4.269	0.212	0.00486	0.01494	-0.947	0.0048	-235.6	924.76		
92r	0.1712	18.2	0.39	0.1	2	0.081	7.393	0.246	0.00985	0.00591	-0.362	0.0098	-83.69	315.74		
93r	0.2083	18.2	0.4	0.09	2	0.102	1.535	0.295	0.01065	0.00784	-0.484	0.0106	-114.1	435.18		
94r	0.1927	18.0	0.36	0.13	2	0.035	1.317	0.189	0.01226	0.00471	-0.292	0.0122	-69.59	266.96		
95r	0.1145	18.1	0.02	0.47	2	0.039	2.965	0.237	0.0062	0.00519	-0.319	0.0062	-74.92	284.8		
96r	0.0659	18.0	0.12	0.37	2	0.016	2.921	0.168	0.00417	0.00227	-0.133	0.0041	-28.45	102.66		
97r	0.0261	18.1	0.33	0.16	2	0.014	3.008	0.149	-0.003	0.0011	-0.064	-0.003	-13.56	48.7		
98r	0.0145	17.9	0.15	0.15	2	0.008	4.567	0.22	0.00093	0.00049	-0.028	0.0009	-5.793	20.355		
99r	0.0048	17.9	0.15	0.15	2	0.011	3.607	0.207	0.00044	0.00041	-0.023	0.0004	-4.468	15.263		
100r	0.0097	17.9	0.31	0.19	2	0.006	4.062	0.109	0.00068	0.00096	-0.055	0.0006	-11.39	40.241		
101r	0.0226	18.1	0.35	0.14	2	0.027	2.456	0.206	0.00115	0.00049	-0.028	0.0011	-5.687	19.922		
102r	0.0305	18.0	0.09	0.4	2	0.021	1.369	0.204	-0.0024	0.00052	-0.03	-0.002	-5.942	20.657		
103r	0.0402	18.2	0.06	0.43	2	0.019	1.44	0.143	0.00342	0.00279	-0.166	0.0034	-36.13	132.06		
104r	0.046	18.2	0.03	0.46	2	0.031	4.886	0.248	0.00334	0.00067	-0.04	0.0033	-8.606	31.3		
105r	0.0349	18.0	0.3	0.19	2	0.01	2.049	0.175	0.00227	0.0004	-0.023	0.0022	-4.984	17.854		

Continue on next page...

Table A.4 – Continued from previous page

img	density	mag <sub>50</sub>	emag(–)	emag(+)	best fit	func <sub>50</sub>	exponential function					polynomial function				
							a <sub>efac</sub>	b <sub>efac</sub>	c <sub>efac</sub>	a <sub>pfac</sub>	b <sub>pfac</sub>	c <sub>pfac</sub>	d <sub>pfac</sub>	e <sub>pfac</sub>		
106r	0.0239	18.2	0.05	0.05	2	0.032	5.766	0.189	0.00158	0.00086	-0.051	0.0015	-11.01	39.987		
107r	0.015	18.1	0.05	0.05	2	0.016	6.63	0.189	0.00062	0.00039	-0.022	0.0006	-4.715	16.743		
108r	0.0075	18.0	0.11	0.38	2	0.011	2.809	0.175	-0.0033	0.00018	-0.01	-0.003	-1.906	6.494		
109r	0.0055	17.9	0.1	0.39	2	0.008	4.719	0.183	0.00049	0.00024	-0.013	0.0004	-2.673	9.12		
110r	0.0029	17.9	0.16	0.33	2	0.014	1.007	0.154	0.00015	0.00034	-0.019	0.0001	-3.594	12.163		
111r	0.004	17.8	0.1	0.39	2	0.014	5.404	0.245	-0.0001	0.00035	-0.019	-0.000	-3.526	11.727		
112r	0.0061	17.9	0.08	0.41	2	0.01	2.96	0.178	0.00092	0.00055	-0.031	0.0009	-6.098	20.948		
113r	0.0072	17.8	0.3	0.19	2	0.012	2.083	0.309	-0.0053	0.00014	-0.007	-0.005	-1.207	3.7913		
114r	0.0075	18.1	0.32	0.17	2	0.027	1.146	0.251	0.0011	0.00031	-0.017	0.0011	-3.388	11.622		
115r	0.0077	18.0	0.29	0.2	2	0.012	4.312	0.203	0.00106	0.00053	-0.03	0.0010	-6.092	21.294		
116r	0.0074	18.0	0.3	0.19	2	0.014	1.141	0.194	0.00145	0.00048	-0.027	0.0014	-5.217	17.789		
117r	0.0058	18.1	0.02	0.47	2	0.019	1.705	0.11	0.00132	8.74864	-0.004	0.0013	-0.881	2.941		
118r	0.0041	17.9	0.28	0.21	2	0.005	2.158	0.178	0.00022	0.00016	-0.009	0.0002	-1.721	5.8468		
119r	0.0031	18.0	0.31	0.18	2	0.02	4.514	0.246	-0.0047	0.00033	-0.018	-0.004	-3.631	12.483		
120r	0.0034	17.8	0.07	0.42	2	0.007	2.761	0.182	0.00097	0.00033	-0.018	0.0009	-3.568	12.171		
121r	0.0022	17.8	0.3	0.19	2	0.005	7.145	0.13	0.00043	0.00022	-0.012	0.0004	-2.408	8.2773		
1i	0.0052	17.6	0.34	0.15	2	0.011	6.202	0.199	-0.0023	0.00022	-0.012	-0.002	-2.194	7.2351		
2i	0.0049	17.7	0.04	0.45	2	0.002	2.653	0.143	-0.0036	0.00017	-0.009	-0.003	-1.661	5.512		
3i	0.0057	17.6	0.27	0.22	2	0.002	1.599	0.168	-0.0035	0.00085	-0.048	-0.003	-9.801	34.407		

Continue on next page...

Table A.4 – Continued from previous page

img	density	mag <sub>50</sub>	emag(-)	emag(+)	best fit	func <sub>50</sub>	exponential function					polynomial function				
							a <sub>efac</sub>	b <sub>efac</sub>	c <sub>efac</sub>	a <sub>pfac</sub>	b <sub>pfac</sub>	c <sub>pfac</sub>	d <sub>pfac</sub>	e <sub>pfac</sub>		
4i	0.0051	17.8	0.0	0.49	2	0.015	1.658	0.285	-0.0045	0.00024	-0.013	-0.004	-2.771	9.7032		
5i	0.0061	17.7	0.17	0.32	2	0.006	3.301	0.222	-0.0039	0.00054	-0.03	-0.003	-5.988	20.693		
6i	0.0082	17.7	0.18	0.31	2	0.002	7.697	0.154	-0.0028	0.00104	-0.059	-0.002	-12.09	42.564		
7i	0.0097	17.9	0.3	0.19	2	0.01	2.748	0.15	-0.0001	0.00089	-0.05	-0.000	-9.803	33.639		
8i	0.0106	17.7	0.27	0.22	2	0.005	1.666	0.152	-0.0003	0.00096	-0.056	-0.000	-11.77	42.156		
9i	0.0104	17.6	0.27	0.22	2	0.002	3.168	0.173	-0.0019	0.00053	-0.03	-0.001	-5.952	20.631		
10i	0.0089	17.8	0.09	0.4	2	0.007	1.034	0.141	-0.0008	0.00075	-0.042	-0.000	-8.105	27.632		
11i	0.0074	17.7	0.05	0.44	2	0.003	3.803	0.114	0.0003	0.00074	-0.041	0.0003	-8.053	27.645		
12i	0.0059	17.9	0.02	0.47	2	0.005	2.595	0.074	3.63193	0.00078	-0.044	3.6319	-8.527	29.202		
13i	0.0065	17.7	0.27	0.22	2	0.005	1.011	0.143	0.00082	0.00045	-0.025	0.0008	-4.705	15.805		
14i	0.0086	17.8	0.18	0.31	2	0.014	6.701	0.225	0.00033	0.00055	-0.031	0.0003	-6.159	21.33		
15i	0.0132	17.8	0.15	0.34	2	0.01	3.905	0.191	-0.0004	0.00168	-0.099	-0.000	-21.28	77.241		
16i	0.021	17.7	0.27	0.22	2	0.008	1.11	0.197	0.00098	0.00137	-0.079	0.0009	-16.25	57.565		
17i	0.0321	17.8	0.28	0.21	2	0.016	2.232	0.169	0.0012	0.00212	-0.125	0.0012	-26.82	97.24		
18i	0.0452	17.9	0.33	0.16	2	0.02	1.874	0.152	0.00266	0.00152	-0.088	0.0026	-18.51	66.208		
19i	0.0482	17.9	0.3	0.19	2	0.04	1.507	0.208	0.00159	0.00284	-0.167	0.0015	-35.28	127.04		
20i	0.0456	17.8	0.12	0.37	2	0.01	4.846	0.16	0.00198	0.00221	-0.129	0.0019	-27.24	97.845		
21i	0.0373	17.8	0.06	0.43	2	0.013	2.462	0.139	0.00306	0.00279	-0.165	0.0030	-35.36	128.31		
22i	0.0247	17.7	0.04	0.45	2	0.009	1.958	0.149	0.00156	0.00187	-0.107	0.0015	-21.62	75.803		

Continue on next page...

Table A.4 – Continued from previous page

img	density	mag <sub>50</sub>	emag(-)	emag(+)	best fit	func <sub>50</sub>	exponential function					polynomial function				
							a <sub>efac</sub>	b <sub>efac</sub>	c <sub>efac</sub>	a <sub>pfac</sub>	b <sub>pfac</sub>	c <sub>pfac</sub>	d <sub>pfac</sub>	e <sub>pfac</sub>		
23i	0.0079	17.9	0.14	0.35	2	0.016	9.22	0.203	-0.0001	0.00045	-0.025	-0.000	-5.062	17.528		
24i	0.0146	17.9	0.3	0.19	2	0.015	7.758	0.158	0.00108	0.0004	-0.022	0.0010	-4.031	13.328		
25i	0.0243	17.9	0.15	0.34	2	0.023	4.182	0.206	-0.0005	0.00151	-0.088	-0.000	-18.37	65.633		
26i	0.0493	17.9	0.02	0.48	2	0.025	6.957	0.187	0.00079	0.00367	-0.216	0.0007	-46.2	167.08		
27i	0.0979	18.0	0.0	0.49	2	0.061	8.72	0.238	0.00212	0.00601	-0.36	0.0021	-79.74	294.13		
28i	0.1533	17.8	0.28	0.21	2	0.02	2.171	0.18	0.00699	0.00804	-0.491	0.0069	-113.1	426.28		
29i	0.1899	17.8	0.31	0.18	2	0.058	2.814	0.331	0.00269	0.00802	-0.482	0.0026	-107.1	395.89		
30i	0.1656	17.9	0.08	0.41	2	0.04	5.321	0.223	0.00889	0.00552	-0.329	0.0088	-72.04	264.2		
31i	0.137	17.9	0.3	0.19	2	0.032	3.873	0.199	0.00436	0.0039	-0.231	0.0043	-50.1	182.55		
32i	0.1033	17.8	0.3	0.19	2	0.038	1.159	0.237	0.00302	0.00962	-0.581	0.0030	-130.5	485.56		
33i	0.0771	17.8	0.11	0.38	2	0.04	3.524	0.209	0.00296	0.00468	-0.276	0.0029	-59.63	216.98		
34i	0.0138	17.9	0.29	0.2	2	0.013	6.656	0.197	-0.0014	0.0009	-0.052	-0.001	-10.7	37.884		
35i	0.0381	17.9	0.07	0.42	2	0.013	3.055	0.137	0.00207	0.00243	-0.142	0.0020	-30.09	108.26		
36i	0.099	17.9	0.11	0.38	2	0.043	6.41	0.26	0.00116	0.00627	-0.379	0.0011	-85.7	319.7		
37i	0.1914	18.0	0.34	0.15	2	0.084	3.824	0.334	0.00306	0.02083	-1.327	0.0030	-334.5	1322.7		
38i	0.2832	17.9	0.12	0.37	2	0.073	3.315	0.307	0.00893	0.01711	-1.079	0.0089	-266.0	1039.8		
39i	0.4019	17.9	0.35	0.15	4	0.088	9.474	0.454	0.00694	0.01842	-1.167	0.0069	-291.3	1145.8		
40i	0.5327	18.0	0.39	0.1	2	0.125	5.035	0.276	0.02508	0.00959	-0.595	0.0250	-141.7	544.34		
41i	0.4738	17.8	0.09	0.4	2	0.058	5.941	0.299	0.02257	0.00543	-0.341	0.0225	-84.19	329.32		

Continue on next page...

Table A.4 – Continued from previous page

img	density	mag <sub>50</sub>	emag(-)	emag(+)	best fit	func <sub>50</sub>	exponential function					polynomial function				
							a <sub>efac</sub>	b <sub>efac</sub>	c <sub>efac</sub>	a <sub>pfac</sub>	b <sub>pfac</sub>	c <sub>pfac</sub>	d <sub>pfac</sub>	e <sub>pfac</sub>		
42i	0.3812	17.8	0.31	0.18	2	0.045	1.35	0.207	0.02035	0.03174	-2.065	0.0203	-544.7	2206.4		
43i	0.1947	17.8	0.3	0.19	2	0.062	4.498	0.365	0.00423	0.02001	-1.27	0.0042	-317.8	1252.2		
44i	0.126	17.8	0.3	0.19	2	0.032	7.47	0.205	0.00491	0.03052	-1.946	0.0049	-491.5	1946.1		
45i	0.042	18.0	0.32	0.17	2	0.016	2.186	0.174	0.00064	0.00133	-0.077	0.0006	-16.29	58.349		
46i	0.1324	17.9	0.08	0.41	2	0.058	1.792	0.304	-6.5792	0.00692	-0.415	-6.579	-92.51	342.24		
47i	0.2448	17.9	0.02	0.47	2	0.049	1.619	0.226	0.01029	0.0171	-1.086	0.0102	-272.0	1072.4		
48i	0.3989	17.8	0.31	0.18	2	0.043	3.92	0.228	0.01672	0.01112	-0.695	0.0167	-168.5	653.1		
49i	0.781	17.8	0.01	0.48	2	0.129	2.465	0.439	0.0352	0.00962	-0.611	0.0352	-153.5	606.85		
50i	1.1783	17.6	0.4	0.09	4	0.189	2.092	1.544	0.00808	0.0003	-0.016	0.0080	-2.712	8.6081		
51i	1.2675	17.4	0.37	0.12	4	0.189	1.252	1.231	0.02364	0.00088	-0.049	0.0236	-9.691	33.6		
52i	0.9855	17.6	0.38	0.12	4	0.145	3.805	1.164	0.01657	0.00534	-0.336	0.0165	-83.33	326.99		
53i	0.7177	17.7	0.01	0.48	2	0.123	1.837	0.459	0.02778	0.00883	-0.555	0.0277	-136.5	533.69		
54i	0.284	17.8	0.06	0.43	2	0.076	3.471	0.346	0.00953	0.0191	-1.204	0.0095	-297.2	1162.6		
55i	0.1437	17.8	0.01	0.48	2	0.065	4.383	0.296	0.00363	0.02651	-1.687	0.0036	-424.4	1677.2		
56i	0.0957	17.9	0.0	0.49	2	0.036	1.464	0.232	0.00279	0.00589	-0.354	0.0027	-78.52	290.04		
57i	0.2502	17.9	0.05	0.44	2	0.085	3.961	0.32	0.00663	0.01448	-0.898	0.0066	-213.4	817.59		
58i	0.4652	17.8	0.04	0.45	2	0.07	1.318	0.28	0.02108	0.00802	-0.492	0.0210	-114.5	434.22		
59i	0.8493	17.7	0.34	0.15	4	0.121	7.023	0.543	0.0314	0.0134	-0.861	0.0314	-221.4	885.91		
60i	1.4246	17.2	0.35	0.14	4	0.197	4.322	1.332	0.01862	0.00171	-0.102	0.0186	-23.45	88.702		

Continue on next page...

Table A.4 – Continued from previous page

img	density	mag <sub>50</sub>	emag(–)	emag(+)	best fit	func <sub>50</sub>	exponential function					polynomial function				
							a <sub>efac</sub>	b <sub>efac</sub>	c <sub>efac</sub>	a <sub>pfac</sub>	b <sub>pfac</sub>	c <sub>pfac</sub>	d <sub>pfac</sub>	e <sub>pfac</sub>		
61i	1.7095	16.6	0.33	0.16	4	0.233	4.074	0.935	0.0387	0.00693	-0.408	0.0387	-88.73	326.69		
62i	1.5808	17.1	0.39	0.1	4	0.252	6.169	1.334	0.01706	0.0015	-0.086	0.0170	-18.15	65.74		
63i	1.1755	17.4	0.01	0.48	4	0.18	6.53	0.727	0.03292	0.00928	-0.571	0.0329	-134.2	512.83		
64i	0.6992	17.6	0.34	0.15	2	0.091	5.064	0.4	0.02981	0.01597	-1.007	0.0298	-249.0	975.2		
65i	0.3106	17.8	0.32	0.17	2	0.059	1.362	0.245	0.01284	0.01339	-0.841	0.0128	-205.5	800.22		
66i	0.1032	17.8	0.3	0.19	2	0.043	3.477	0.241	0.00341	0.00472	-0.279	0.0034	-59.69	216.36		
67i	0.1274	17.9	0.12	0.37	2	0.017	1.852	0.155	0.00497	0.00286	-0.171	0.0049	-37.99	140.39		
68i	0.3149	17.8	0.1	0.39	2	0.061	2.614	0.294	0.0114	0.01001	-0.614	0.0114	-143.1	542.76		
69i	0.5515	17.8	0.01	0.48	2	0.109	9.11	0.407	0.01948	0.01572	-0.986	0.0194	-240.4	934.6		
70i	0.922	17.6	0.03	0.46	4	0.123	2.814	1.148	0.01001	0.00677	-0.431	0.0100	-108.6	430.24		
71i	1.2877	17.3	0.05	0.44	4	0.176	8.659	1.422	0.01169	0.00012	-0.005	0.0116	-0.983	3.534		
72i	1.4062	17.0	0.31	0.18	4	0.176	6.375	1.367	0.01844	0.00249	-0.148	0.0184	-32.95	122.51		
73i	1.1366	17.7	0.42	0.07	4	0.187	1.918	1.539	0.00474	0.00206	-0.13	0.0047	-32.54	128.75		
74i	0.7078	17.7	0.03	0.46	2	0.098	1.734	0.392	0.03139	0.02641	-1.692	0.0313	-431.4	1717.1		
75i	0.3962	17.7	0.28	0.21	2	0.055	1.26	0.27	0.01836	0.02313	-1.477	0.0183	-373.9	1482.6		
76i	0.1718	17.9	0.09	0.4	2	0.046	1.538	0.219	0.00532	0.00612	-0.37	0.0053	-83.4	310.71		
77i	0.0459	17.7	0.28	0.21	2	0.006	7.242	0.135	0.00271	0.00093	-0.054	0.0027	-11.43	41.009		
78i	0.1293	17.8	0.03	0.46	2	0.041	1.202	0.28	0.00246	0.00682	-0.411	0.0024	-92.3	343.0		
79i	0.2641	17.7	0.28	0.21	2	0.034	1.206	0.262	0.01303	0.02588	-1.663	0.0130	-426.7	1704.2		

Continue on next page...

Table A.4 – Continued from previous page

img	density	mag <sub>50</sub>	emag(−)	emag(+)	best fit	func <sub>50</sub>	exponential function					polynomial function				
							a <sub>efac</sub>	b <sub>efac</sub>	c <sub>efac</sub>	a <sub>pfac</sub>	b <sub>pfac</sub>	c <sub>pfac</sub>	d <sub>pfac</sub>	e <sub>pfac</sub>		
80i	0.4499	17.8	0.04	0.45	2	0.058	1.744	0.263	0.02072	0.02938	-1.889	0.0207	-485.5	1940.0		
81i	0.6538	17.7	0.08	0.41	4	0.08	2.927	0.467	0.02415	0.02537	-1.643	0.0241	-428.9	1728.3		
82i	0.7753	17.7	0.34	0.15	2	0.116	3.977	0.501	0.02645	0.00779	-0.476	0.0264	-110.2	416.58		
83i	0.6905	17.8	0.0	0.49	2	0.097	4.152	0.332	0.02922	0.00852	-0.532	0.0292	-129.0	500.33		
84i	0.4891	18.0	0.36	0.13	4	0.136	3.925	0.472	0.01344	0.01899	-1.215	0.0134	-309.6	1231.3		
85i	0.3051	18.0	0.33	0.16	2	0.075	1.02	0.225	0.0142	0.00614	-0.372	0.0142	-84.35	314.93		
86i	0.1598	18.0	0.34	0.15	2	0.087	2.253	0.294	0.00247	0.01313	-0.815	0.0024	-194.4	746.67		
87i	0.0694	18.0	0.32	0.17	2	0.033	5.768	0.167	0.00333	0.00435	-0.259	0.0033	-56.78	208.21		
88i	0.0231	17.8	0.15	0.34	2	0.008	2.782	0.153	0.00192	0.00105	-0.059	0.0019	-11.62	39.956		
89i	0.0576	17.9	0.01	0.48	2	0.019	5.93	0.171	0.00305	0.00652	-0.406	0.0030	-97.44	375.43		
90i	0.1382	17.9	0.31	0.18	2	0.063	4.108	0.285	0.00251	0.02173	-1.368	0.0025	-336.5	1313.6		
91i	0.2685	18.0	0.36	0.14	2	0.085	1.278	0.207	0.01276	0.01477	-0.934	0.0127	-232.1	911.44		
92i	0.3218	18.0	0.36	0.13	2	0.083	5.432	0.268	0.01404	0.01022	-0.631	0.0140	-149.0	569.1		
93i	0.3328	17.9	0.34	0.15	2	0.099	1.922	0.394	0.00742	0.01078	-0.661	0.0074	-153.9	582.97		
94i	0.2993	17.9	0.11	0.38	2	0.041	7.618	0.201	0.01363	0.01021	-0.638	0.0136	-154.2	596.64		
95i	0.1843	18.0	0.0	0.0	2	0.05	1.188	0.246	0.0053	0.01947	-1.235	0.0053	-308.4	1213.4		
96i	0.107	18.0	0.06	0.43	2	0.066	1.298	0.272	0.00104	0.00905	-0.552	0.0010	-126.8	477.31		
97i	0.0549	17.7	0.27	0.22	2	0.012	4.551	0.223	0.00193	0.00442	-0.263	0.0019	-57.16	208.91		
98i	0.0261	17.9	0.3	0.19	2	0.021	1.648	0.172	0.0011	0.00236	-0.138	0.0011	-29.44	106.2		

Continue on next page...

Table A.4 – Continued from previous page

img	density	mag <sub>50</sub>	emag(-)	emag(+)	best fit	func <sub>50</sub>	exponential function				polynomial function			
							a <sub>efac</sub>	b <sub>efac</sub>	c <sub>efac</sub>	a <sub>pfac</sub>	b <sub>pfac</sub>	c <sub>pfac</sub>	d <sub>pfac</sub>	e <sub>pfac</sub>
99i	0.0095	17.8	0.14	0.35	2	0.012	9.078	0.148	0.00085	0.00051	-0.028	0.0008	-5.391	18.239
100i	0.0212	17.9	0.3	0.19	2	0.009	7.001	0.18	0.00102	0.00132	-0.077	0.0010	-16.34	58.649
101i	0.0372	17.7	0.28	0.21	2	0.008	3.579	0.162	0.00156	0.00229	-0.132	0.0015	-26.67	93.697
102i	0.062	17.8	0.13	0.36	2	0.017	6.636	0.201	0.0016	0.00335	-0.197	0.0016	-42.4	153.82
103i	0.0749	18.0	0.04	0.45	2	0.036	3.506	0.216	0.00054	0.00455	-0.272	0.0005	-60.31	222.5
104i	0.0726	17.9	0.28	0.21	2	0.025	2.264	0.185	0.00293	0.00355	-0.21	0.0029	-45.4	165.13
105i	0.0581	17.8	0.27	0.22	2	0.008	3.317	0.182	0.00181	0.00371	-0.22	0.0018	-47.96	175.24
106i	0.0425	18.0	0.03	0.46	2	0.03	1.835	0.159	0.00257	0.00206	-0.121	0.0025	-25.83	93.267
107i	0.0271	17.9	0.17	0.32	2	0.009	6.571	0.141	0.00168	0.00148	-0.086	0.0016	-18.04	64.474
108i	0.0161	17.8	0.27	0.22	2	0.014	8.219	0.202	0.00028	0.00113	-0.064	0.0002	-12.93	45.1
109i	0.0095	17.8	0.29	0.2	2	0.012	1.422	0.176	0.00053	0.00088	-0.05	0.0005	-9.913	34.423
110i	0.0069	17.7	0.09	0.4	2	0.007	3.805	0.147	0.00066	0.00035	-0.019	0.0006	-3.639	12.284
111i	0.0078	17.7	0.28	0.21	2	0.005	3.789	0.147	0.0006	0.00039	-0.022	0.0006	-4.136	13.955
112i	0.0106	17.7	0.16	0.33	2	0.007	1.79	0.149	0.00076	0.0011	-0.061	0.0007	-11.49	38.794
113i	0.0142	17.8	0.13	0.36	2	0.011	6.508	0.187	0.00091	0.00047	-0.026	0.0009	-4.987	16.912
114i	0.0145	17.9	0.04	0.45	2	0.02	3.588	0.206	0.00093	0.00055	-0.031	0.0009	-6.169	21.358
115i	0.0126	17.9	0.13	0.36	2	0.009	2.198	0.115	0.00152	0.00075	-0.042	0.0015	-8.172	28.028
116i	0.0122	17.9	0.08	0.41	2	0.011	4.847	0.145	0.00116	0.00042	-0.023	0.0011	-4.327	14.474
117i	0.01	17.9	0.04	0.45	2	0.018	1.713	0.152	0.00184	0.00055	-0.03	0.0018	-5.618	18.804

Continue on next page...

Table A.4 – Continued from previous page

img	density	mag <sub>50</sub>	emag(-)	emag(+)	best fit	func <sub>50</sub>	exponential function				polynomial function			
							a <sub>efac</sub>	b <sub>efac</sub>	c <sub>efac</sub>	a <sub>pfac</sub>	b <sub>pfac</sub>	c <sub>pfac</sub>	d <sub>pfac</sub>	e <sub>pfac</sub>
118i	0.0073	17.7	0.26	0.23	2	0.004	3.403	0.163	0.00053	0.0004	-0.022	0.0005	-4.08	13.648
119i	0.0079	17.9	0.01	0.49	2	0.015	1.852	0.172	0.00016	0.00057	-0.032	0.0001	-6.221	21.326
120i	0.0064	17.7	0.16	0.33	2	0.016	3.26	0.243	0.00097	0.00027	-0.015	0.0009	-2.856	9.5769
121i	0.0048	17.4	0.27	0.22	2	0.003	3.317	0.18	0.00065	0.00044	-0.024	0.0006	-4.564	15.4

# Appendix B

## List of Abbreviations

- AGB** Asymptotic Giant Branch  
**AST** Artificial Stars Test  
**CCD** Charge Coupled Device  
**CFHT** Canada France Hawaii Telescope  
**CIT** Caltech System  
**CMD** Colour Magnitude Diagram  
**FWHM** Full Width at Half Maximum  
**GC** Globular Cluster  
**GGC** Galactic Globular Cluster  
**HB** Horizontal Branch  
**HRD** Hertzsprung- Russel Diagram  
**IMF** Initial Mass Function  
**IRAC** Infra red Array Camera  
 $M_{bol}$  bolometric Magnitude  
**ML** Mass Loss  
**MS** Main Sequence  
**LPV** Long Period Variable  
**PSF** Point Spread Function  
**RGB** Red Giant Branch

**RGB-a** anomalous **R**ed **G**iant **B**ranch

**SDSS** Sloan **D**igital **S**ky **S**urvey

**SGB** Sub **G**iant **B**ranch

**SFH** Star **F**ormation **H**istory

**SFR** Star **F**ormation **R**ate

**SSP** Simple **S**tellar **P**opulation

$T_{eff}$  effective **T**emperature

**TPAGB** Thermal **P**ulsing **A**symptotic **G**iant **B**ranch

**TCS** Telescopio **C**arlos **S**anches

**TO** Turn **O**ff

**TRGB** Tip of **R**ed **G**iant **B**ranch

**2MASS** Two **M**icron **A**ll **S**ky **S**urvey

# Bibliography

- Abbott, D. C. 1982, in IAU Symposium, Vol. 99, Wolf-Rayet Stars: Observations, Physics, Evolution, ed. C. W. H. De Loore & A. J. Willis, 185–193
- Allain, S. 1998, *A&A*, 333, 629
- Alonso, A., Arribas, S., & Martínez-Roger, C. 1998, *A&AS*, 131, 209
- Alonso, A., Arribas, S., & Martínez-Roger, C. 1999, *A&AS*, 140, 261
- Alonso, A., Arribas, S., & Martínez-Roger, C. 2001, *A&A*, 376, 1039
- Anderson, J. 2002, in Astronomical Society of the Pacific Conference Series, Vol. 265, Omega Centauri, A Unique Window into Astrophysics, ed. F. van Leeuwen, J. D. Hughes, & G. Piotto, 87
- Aparicio, A. & Gallart, C. 1995, *AJ*, 110, 2105
- Aparicio, A. & Gallart, C. 2004, *AJ*, 128, 1465
- Aparicio, A. & Hidalgo, S. L. 2009, *AJ*, 138, 558
- Audoze, J. & Mathieu, N. 1986, *Science*, 233, 1210
- Baade, W. 1944, *ApJ*, 100, 137
- Baldry, I. K., Driver, S. P., Loveday, J., et al. 2012, *MNRAS*, 421, 621
- Barker, M. K., Ferguson, A. M. N., Cole, A. A., et al. 2011, *MNRAS*, 410, 504
- Barker, M. K., Sarajedini, A., Geisler, D., Harding, P., & Schommer, R. 2007, *AJ*, 133, 1125

- Barnes, J. E. & Hernquist, L. 1992, *ARA&A*, 30, 705
- Bastian, N. & Lardo, C. 2018, *ARA&A*, 56, 83
- Bauer, A. E., Hopkins, A. M., Gunawardhana, M., et al. 2013, *MNRAS*, 434, 209
- Baugh, C. M. 2006, *Reports on Progress in Physics*, 69, 3101
- Beasley, M. A., San Roman, I., Gallart, C., Sarajedini, A., & Aparicio, A. 2015, *MNRAS*, 451, 3400
- Bedin, L. R., Piotto, G., Anderson, J., et al. 2004, *Memorie della Societa Astronomica Italiana Supplementi*, 5, 105
- Bekki, K. 2008, *MNRAS*, 390, L24
- Bekki, K. & Freeman, K. C. 2003, *MNRAS*, 346, L11
- Bellazzini, M., Ferraro, F. R., Sollima, A., Pancino, E., & Origlia, L. 2004, *A&A*, 424, 199
- Bellini, A., Libralato, M., Bedin, L. R., et al. 2018, *ApJ*, 853, 86
- Benacquista, M. J. 2002, *Living Reviews in Relativity*, 5, 2
- Bernard, E. J., Ferguson, A. M. N., Barker, M. K., et al. 2012, *MNRAS*, 420, 2625
- Bernard, E. J., Ferguson, A. M. N., Richardson, J. C., et al. 2015, *MNRAS*, 446, 2789
- Bessell, M. S. 2005, *ARA&A*, 43, 293
- Bothun, G. D. 1992, *AJ*, 103, 104
- Boyer, M. L., McDonald, I., van Loon, J. T., et al. 2008, *AJ*, 135, 1395
- Boyer, M. L., van Loon, J. T., McDonald, I., et al. 2010, *The Astrophysical Journal*, 711, L99
- Boyer, M. L., Woodward, C. E., van Loon, J. T., et al. 2006, *AJ*, 132, 1415
- Bressan, A., Marigo, P., Girardi, L., et al. 2012, *MNRAS*, 427, 127

- Brinchmann, J., Charlot, S., White, S. D. M., et al. 2004, *MNRAS*, 351, 1151
- Brown, T. M. 2009, *Astronomical Society of the Pacific Conference Series*, Vol. 419, The Star Formation Histories of the M31 and M33 Spheroids, ed. S. Jogee, I. Marinova, L. Hao, & G. A. Blanc, 110
- Brown, T. M., Smith, E., Ferguson, H. C., et al. 2006, *ApJ*, 652, 323
- Carpenter, J. M. 2001, *AJ*, 121, 2851
- Catelan, M. 1993, *A&AS*, 98, 547
- Catelan, M. 2000, in *Liege International Astrophysical Colloquia*, Vol. 35, *Liege International Astrophysical Colloquia*, ed. A. Noels, P. Magain, D. Caro, E. Jehin, G. Parmentier, & A. A. Thoul, 485
- Catelan, M., Ferraro, F. R., & Rood, R. T. 2001, *ApJ*, 560, 970
- Chiosi, C. & Maeder, A. 1986, *ARA&A*, 24, 329
- Christy, R. F. 1966, *ApJ*, 144, 108
- Clement, C. 1997, *VizieR Online Data Catalog*, 5097
- Cole, A. A., Skillman, E. D., Tolstoy, E., et al. 2007, *ApJl*, 659, L17
- Corbelli, E. 2003, *MNRAS*, 342, 199
- Dado, S. & Dar, A. 2014, *ApJ*, 785, 70
- Dalessandro, E., Salaris, M., Ferraro, F. R., Mucciarelli, A., & Cassisi, S. 2013, *MNRAS*, 430, 459
- Davidge, T. J. & Puzia, T. H. 2011, *ApJ*, 738, 144
- D’Cruz, N. L., Dorman, B., Rood, R. T., & O’Connell, R. W. 1996, *ApJ*, 466, 359
- de Boer, T. J. L., Tolstoy, E., Hill, V., et al. 2012, *A&A*, 539, A103
- Deutsch, A. J. 1956, *ApJ*, 123, 210

- di Criscienzo, M., Ventura, P., D'Antona, F., Milone, A., & Piotto, G. 2010, *MNRAS*, 408, 999
- Dobbs, C. L. 2011, in *EAS Publications Series*, Vol. 52, *EAS Publications Series*, ed. M. Röllig, R. Simon, V. Ossenkopf, & J. Stutzki, 87–93
- Dobbs, C. L., Pettitt, A. R., Corbelli, E., & Pringle, J. E. 2018, *MNRAS*, 478, 3793
- Dolphin, A. E. 2002, *MNRAS*, 332, 91
- Dolphin, A. E. & Hunter, D. A. 1998, *AJ*, 116, 1275
- D'Souza, R. & Rix, H.-W. 2013, *Monthly Notices of the Royal Astronomical Society*, 429, 1887–1901
- Eggen, O. J., Lynden-Bell, D., & Sandage, A. R. 1962, *ApJ*, 136, 748
- Elitzur, M., Goldreich, P., & Scoville, N. 1976, *ApJ*, 205, 384
- Elitzur, M. & Ivezić, Ž. 2001, *MNRAS*, 327, 403
- Faber, S. M. & Gallagher, J. S. 1979, *ARA&A*, 17, 135
- Falceta-Gonçalves, D. & Jatenco-Pereira, V. 2002, *ApJ*, 576, 976
- Fazio, G. G., Hora, J. L., Allen, L. E., et al. 2004, *ApJS*, 154, 10
- Ferraro, F. R., Paltrinieri, B., Fusi Pecci, F., Rood, R. T., & Dorman, B. 1998, *ApJ*, 500, 311
- Fitzpatrick, E. L. 1999, *PASP*, 111, 63
- Freedman, W. L., Wilson, C. D., & Madore, B. F. 1991, *ApJ*, 372, 455
- Frogel, J. A. & Elias, J. H. 1988, *ApJ*, 324, 823
- Fusi Pecci, F. & Bellazzini, M. 1997, in *The Third Conference on Faint Blue Stars*, ed. A. G. D. Philip, J. Liebert, R. Saffer, & D. S. Hayes, 255
- Gaia Collaboration, Brown, A. G. A., Vallenari, A., et al. 2018, *A&A*, 616, A1

- Gaia Collaboration, Prusti, T., de Bruijne, J. H. J., et al. 2016, *A&A*, 595, A1
- Gallart, C., Aparicio, A., & Vilchez, J. M. 1996, *AJ*, 112, 1928
- Gallart, C., Zoccali, M., & Aparicio, A. 2005, *ARA&A*, 43, 387
- Giersz, M. & Heggie, D. C. 2003, *MNRAS*, 339, 486
- Goldberg, L. 1979, *QJRAS*, 20, 361
- Graham, A. W. 2001, *AJ*, 121, 820
- Greggio, L. 2005, *A&A*, 441, 1055
- Greiner, J., Michałowski, M. J., Klose, S., et al. 2016, *A&A*, 593, A17
- Harris, J. & Zaritsky, D. 2001, *ApJS*, 136, 25
- Harris, J. & Zaritsky, D. 2004, *AJ*, 127, 1531
- Harris, W. E. 1996, *AJ*, 112, 1487
- Hartman, J. D., Bersier, D., Stanek, K. Z., et al. 2006, *MNRAS*, 371, 1405
- Hernandez, X., Gilmore, G., & Valls-Gabaud, D. 2000, *MNRAS*, 317, 831
- Herschel, W. 1789, *Philosophical Transactions of the Royal Society of London Series I*, 79, 212
- Höfner, S. & Olofsson, H. 2018, *A&A Rev.*, 26, 1
- Hubble, E. P. 1926, *ApJ*, 64, 321
- Iben, Icko, J. & Rood, R. T. 1970, in *BAAS*, Vol. 2, 201
- Ivezic, Z., Nenkova, M., & Elitzur, M. 1999, *DUSTY: Radiation transport in a dusty environment*, Astrophysics Source Code Library
- Jimenez, R. & MacDonald, J. 1996, *MNRAS*, 283, 721
- Johnson, C. I. & Pilachowski, C. A. 2010, *ApJ*, 722, 1373

- Johnson, J. L., Greif, T. H., & Bromm, V. 2008a, *MNRAS*, 388, 26
- Johnson, J. L., Greif, T. H., & Bromm, V. 2008b, in *IAU Symposium*, Vol. 250, *Massive Stars as Cosmic Engines*, ed. F. Bresolin, P. A. Crowther, & J. Puls, 471–482
- Kaluzny, J., Olech, A., Thompson, I. B., et al. 2004, *A&A*, 424, 1101
- Kennicutt, Robert C., J. 1998, *ApJ*, 498, 541
- Kennicutt, R. C. & Evans, N. J. 2012, *ARA&A*, 50, 531
- Kent, S. M. 1986, *AJ*, 91, 1301
- Kirby, E. N., Boylan-Kolchin, M., Cohen, J. G., et al. 2013, *ApJ*, 770, 16
- Kitzbichler, M. G. & White, S. D. M. 2006, *MNRAS*, 366, 858
- Lamers, H. J. G. L. M. & Cassinelli, J. P. 1999, *Introduction to Stellar Winds*, 452
- Lamers, H. J. G. L. M. & Leitherer, C. 1993, *ApJ*, 412, 771
- Lebzelter, T. & Wood, P. R. 2016, *A&A*, 585, A111
- Lim, J. & White, S. M. 1996, *ApJl*, 462, L91
- Lucy, L. B. & Solomon, P. M. 1970, *ApJ*, 159, 879
- Marino, A. F., Milone, A. P., Piotto, G., et al. 2011, *ApJ*, 731, 64
- Marinoni, C., Monaco, P., Giuricin, G., & Costantini, B. 1999, *ApJ*, 521, 50
- Martín-Manjón, M. L., Mollá, M., Díaz, A. I., & Terlevich, R. 2011, *Monthly Notices of the Royal Astronomical Society*, 420, 1294–1308
- McConnachie, A. W., Ferguson, A. M. N., Irwin, M. J., et al. 2010, *ApJ*, 723, 1038
- McDonald, I., van Loon, J. T., Sloan, G. C., et al. 2011, *MNRAS*, 417, 20
- McDonald, I. & Zijlstra, A. A. 2015, *MNRAS*, 448, 502
- McMonigal, B., Lewis, G. F., Brewer, B. J., et al. 2016, *MNRAS*, 461, 4374

- Meylan, G. 1987, *A&A*, 184, 144
- Milone, A. P., Marino, A. F., Bedin, L. R., et al. 2017, *MNRAS*, 469, 800
- Mowlavi, N., Lecoœur-Taïbi, I., Lebzelter, T., et al. 2018, ArXiv e-prints [[arXiv]1805.02035]
- Nataf, D. M. 2016, , 33, e023
- Norris, J. E. & Da Costa, G. S. 1995, *ApJ*, 447, 680
- Noyola, E., Gebhardt, K., & Bergmann, M. 2006, in *Astronomical Society of the Pacific Conference Series*, Vol. 352, *New Horizons in Astronomy: Frank N. Bash Symposium*, ed. S. J. Kannappan, S. Redfield, J. E. Kessler-Silacci, M. Landriau, & N. Drory, 269
- Noyola, E., Gebhardt, K., & Bergmann, M. 2008, in *IAU Symposium*, Vol. 246, *Dynamical Evolution of Dense Stellar Systems*, ed. E. Vesperini, M. Giersz, & A. Sills, 341–345
- Oey, M. S. & Massey, P. 1995, *ApJ*, 452, 210
- Olofsson, H., González Delgado, D., Kerschbaum, F., & Schöier, F. L. 2002, *A&A*, 391, 1053
- Olsen, K. A. G., Hodge, P. W., Mateo, M., et al. 1998, *MNRAS*, 300, 665
- Origlia, L., Ferraro, F. R., Bellazzini, M., & Pancino, E. 2003, *ApJ*, 591, 916
- Origlia, L., Ferraro, F. R., Fabbri, S., et al. 2014, *A&A*, 564, A136
- Origlia, L., Ferraro, F. R., Fusi Pecci, F., & Rood, R. T. 2002, *ApJ*, 571, 458
- Origlia, L., Ferraro, F. R., & Pecci, F. F. 1996, *MNRAS*, 280, 572
- Origlia, L., Rood, R. T., Fabbri, S., et al. 2007, *ApJ*, 667, L85
- Origlia, L., Rood, R. T., Fabbri, S., et al. 2010, *ApJ*, 718, 522

- Pancino, E., Ferraro, F. R., Bellazzini, M., Piotto, G., & Zoccali, M. 2000, *ApJ*, 534, L83
- Pancino, E., Pasquini, L., Hill, V., Ferraro, F. R., & Bellazzini, M. 2002, *ApJ*, 568, L101
- Pauldrach, A. W. A., Feldmeier, A., Puls, J., & Kudritzki, R. P. 1993, *Space Sci. Rev.*, 66, 105
- Peebles, P. J. E. 1982, in *Astrophysical Cosmology Proceedings*, ed. H. A. Brueck, G. V. Coyne, & M. S. Longair, 165–183
- Percival, S. M. & Salaris, M. 2011, *MNRAS*, 412, 2445
- Petrovic, J., Langer, N., Yoon, S. C., & Heger, A. 2005, *A&A*, 435, 247
- Pietrinferni, A., Cassisi, S., Salaris, M., & Castelli, F. 2004, *ApJ*, 612, 168
- Reach, W. T., Megeath, S. T., Cohen, M., et al. 2005, *PASP*, 117, 978
- Regan, M. W. & Vogel, S. N. 1994, *ApJ*, 434, 536
- Robin, A. C., Marshall, D. J., Schultheis, M., & Reyl , C. 2012, *A&A*, 538, A106
- Rood, R. T. 1973, *ApJ*, 184, 815
- Rowe, J. F., Richer, H. B., Brewer, J. P., & Crabtree, D. R. 2005, *AJ*, 129, 729
- Salaris, M., Cassisi, S., & Pietrinferni, A. 2016, *A&A*, 590, A64
- Salaris, M., Serenelli, A., Weiss, A., & Miller Bertolami, M. 2009, *ApJ*, 692, 1013
- Savaglio, S. 2015, *Journal of High Energy Astrophysics*, 7, 95
- Savino, A., de Boer, T. J. L., Salaris, M., & Tolstoy, E. 2018, *MNRAS*, 480, 1587
- Schatzman, E. L., Praderie, F., & King, A. R. 1993, *The Stars*, 402
- Schmidt, M. 1959, *ApJ*, 129, 243
- Schwarzschild, M. & H rm, R. 1965, *ApJ*, 142, 855

- Searle, L. & Zinn, R. 1978, *ApJ*, 225, 357
- Seigar, M. S. & James, P. A. 2002, *MNRAS*, 337, 1113
- Shapley, H. 1918, *ApJ*, 48
- Small, E. E., Bersier, D., & Salaris, M. 2013, *MNRAS*, 428, 763
- Sollima, A., Ferraro, F. R., Origlia, L., Pancino, E., & Bellazzini, M. 2004, *VizieR Online Data Catalog*, 342
- Stephens, A. W., Frogel, J. A., Freedman, W., et al. 2001, *AJ*, 121, 2584
- Stetson, P. B. 1987, *PASP*, 99, 191
- Stetson, P. B. 1990, *PASP*, 102, 932
- Stetson, P. B. & Harris, W. E. 1988, *AJ*, 96, 909
- Tan, W.-W., Cao, X.-F., & Yu, Y.-W. 2015, , 38, 11
- Tenorio-Tagle, G., Franco, J., Bodenheimer, P., & Rozyczka, M. 1987, *A&A*, 179, 219
- Tolstoy, E., Hill, V., & Tosi, M. 2009, *ARA&A*, 47, 371
- Tolstoy, E. & Saha, A. 1996, *ApJ*, 462, 672
- van Leeuwen, F., Le Poole, R. S., Reijns, R. A., Freeman, K. C., & de Zeeuw, P. T. 2000, *A&A*, 360, 472
- van Loon, J. T., Boyer, M. L., & McDonald, I. 2008, *ApJl*, 680, L49
- VandenBerg, D. A., Brogaard, K., Leaman, R., & Casagrande, L. 2013, *ApJ*, 775, 134
- Vergely, J.-L., Köppen, J., Egret, D., & Bienaymé, O. 2002, *A&A*, 390, 917
- Villanova, S., Piotto, G., King, I. R., et al. 2007, *ApJ*, 663, 296
- Wang, F. Y. & Dai, Z. G. 2014, *ApJS*, 213, 15
- Wei, J.-J. & Wu, X.-F. 2017, *International Journal of Modern Physics D*, 26, 1730002

- 
- Weigert, A. 1965, *Mitteilungen der Astronomischen Gesellschaft Hamburg*, 19, 61
- Weisz, D. R., Dolphin, A. E., Skillman, E. D., et al. 2014, *ApJ*, 789, 147
- White, S. D. M. & Rees, M. J. 1978, *MNRAS*, 183, 341
- Whitney, J. H., Rood, R. T., O'Connell, R. W., et al. 1998, *ApJ*, 495, 284
- Williams, B. F., Dalcanton, J. J., Dolphin, A. E., Holtzman, J., & Sarajedini, A. 2009, *ApJ*, 695, L15
- Willson, L. A., Bowen, G. H., & Struck-Marcell, C. 1987, *Comments on Astrophysics*, 12, 17
- Wolfe, S. A., Pisano, D. J., Lockman, F. J., McGaugh, S. S., & Shaya, E. J. 2013, *Nature*, 497, 224
- Woolley, R. V. D. R. 1966, *Royal Observatory Annals*, 2
- Wosley, S. E. & Heger, A. 2006, *ApJ*, 637, 914